Harnessing locality for scalable strongly correlated electron simulations

Thesis by
Linqing Peng

In Partial Fulfillment of the Requirements for the
Degree of
Doctor of Philosophy

CALIFORNIA INSTITUTE OF TECHNOLOGY
Pasadena, California

2025
Defended April 28, 2025

To my beloved parents and grandparents

ACKNOWLEDGEMENTS

I owe the greatest debt of gratitude to my advisor, Prof. Garnet Chan, without whom this work would not have been possible. His long-term vision and dedication to pushing the boundaries of science, his unwavering commitment to rigor and quality, and his knowledge and deep insight into tackling difficult problems have been guiding lights throughout my Ph.D. I have benefited immensely from his mentorship in creative and critical thinking. His scientific taste and clarity of thought continue to inspire me to develop useful methods. The Ph.D. journey is not easy. I feel truly fortunate to have an advisor who exemplifies all these qualities and is always ready to support.

I would also like to thank my thesis committee—Prof. Austin Minnich, Prof. Ryan Hadt, and Prof. Scott Cushing—as well as Prof. Tom Miller who served on my candidacy committee, for their time and valuable discussions and suggestions on my research and proposals.

I have been fortunate to collaborate with and be mentored by brilliant scientists: Prof. Tianyu Zhu, Dr. Zhihao Cui, Dr. Xing Zhang, Dr. Huanchen Zhai, Dr. Chenghan Li, Dr. Runze Chi, Prof. Hai-Ping Cheng, Dr. Shuanglong Liu, Dr. Xiao Chen, Prof. Stephen Hill, Prof. Mike Shatruk, Dr. Robert Stewart, and Dr. Miguel Gakiya-Teruya. I am grateful for your time and generosity in sharing your knowledge.

To my Chan group family, thank you for creating such a kind, supportive, and intellectually stimulating environment. Besides my collaborators above, many thanks go to the Chan group alums I had the good fortune to overlap with: Dr. Ruojing Peng, Prof. Chong Sun, Dr. Matthew Coley-O'Rourke, Dr. Yang Gao, Dr. Phillip Helms, Prof. Henrik Larsson, Dr. Zuxin Jin, Dr. Reza Haghshenas, Dr. Kasra Hijazi, Prof. Seunghoon Lee, Prof. Wenyuan Liu, Dr. Johannes Tölle, Dr. Ke Liao, Dr. Or Sharir, and Dr. Min Liu, and to current members of the group, Dr. Johnnie Gray, Junjie Yang, Rui Li, Prof. Tomislav Begušić, Dr. Verena Neufeld, Dr. Petra Shin, Shunyue Yuan, Dr. Eirik Kjønstad, Yuhang Ai, Dr. Adil Gangat, Jielun Chen, Shuoxue Li, Gunhee Park, Sijing Du. The small talks in the office—though often brief—have been unexpectedly inspiring and always encouraging.

I also appreciate being part of the Center for Molecular Magnetic Quantum Materials (M2QM). Besides my collaborators, I thank Prof. Samuel Trickey, Prof. Chunjing Jia, Prof. Xiaoxiao Zhang, Prof. Xiaoguang Zhang, Prof. Mark Pederson, Prof. Richard Hennig, and many other members of the center for insightful discussions and suggestions. The interactions make me feel the importance of my work and help me grow scientifically and professionally.

I am grateful to the Chemical Physics Seminar (CPS) series which provides valuable opportunities for students and postdocs to nominate and invite Professors of our interest. I am especially thankful to Elisha Okawa, our CPS coordinator, for ensuring that every speaker's visit and seminar ran smoothly. I will miss my time working with her as the CPS student co-chair.

I would also like to thank the Caltech Institute fellowship, the Caltech C fellowship, the Molecular Sciences Software Institute (MolSSI) fellowship, and the M2QM, an Energy Frontier Research Center funded by the Department of Energy, for funding my PhD work, and National Energy Research Scientific Computing Center (NERSC) for providing computational resources.

Standing at the end of my PhD journey, I remain deeply grateful to those who empowered me to start this path at Caltech: my chemistry advisor, Prof. Elaine Marzluff, and my physics advisor, Prof. Charles Cunningham at Grinnell College, and my research mentors, Dr. Jonathan Poplawsky and Prof. Andrew Mobley.

Last but by no means least, I thank my parents for their unconditional love and support, which gave me the energy and freedom to pursue my intellectual interests. I am deeply grateful to my friends, Dr. Doris Mai, Dr. Jiajun Du, Miranda Kong, Evelyn Li, Vignesh Bhethanabotla, Dr. Roman Korol, Dr. Greg Jones, Dr. Tianhan Liu, Dr. Douglas Ober, Yue Xu, Dr. Sherry Cheng, Dr. Hung Tien Vuong, Dr. Zhuoran Qiao, Lulu, Dr. Matthew Zimmer, Dr. Jorge Rosa, Prof. Joohmin Lee, Dr. Zhuyun Zhuang, Jingya Huang, Siqi Wu, Heyun Li, Dr. Xiaotian Bi, Dr. Zongyuan Wang, Dr. Shumao Zhang, Dr. Hanwei Liu. Special thanks go to my partner, Dr. Xuecheng Tao, for fun scientific arguments and unwavering emotional support, and to our cat Clair, for the fluffy companionship.

ABSTRACT

Materials-specific predictions of large, realistic molecules and materials with strong electron correlations have been a long-standing challenge in quantum chemistry. This dissertation addresses this challenge by leveraging three forms of physical and mathematical locality—in space, energy, and rank—to develop scalable, efficient, and accurate electronic structure methods.

In Chapter 2, we use quantum embedding theory that exploits the spatial locality of electron correlations and reduces the computational cost of accurate correlated electronic structure methods, enabling accurate ab initio simulation of complicated correlated materials. In this work, we study Kondo physics, a prototypical many-body quantum phenomenon, with a full-cell extension of dynamical mean-field theory (DMFT). Our *ab initio* simulation of the Kondo correlations systematically converges towards the exact zero-temperature limit, yielding material-specific Kondo temperatures that reproduce the subtle exponential trends observed experimentally and offer new insight into the underlying physics.

Chapter 3 explores the locality in energy in lanthanide single-ion magnets. Their multi-reference ground and excited states are generally challenging to compute, but fortunately, the states that govern the spin dynamics are local in the energy spectrum. We develop a theoretical protocol to compute their spin Hamiltonian by sampling only relevant states in this reduced Hilbert space, and particularly, the single-reference states accessible by the efficient density functional theory. This method surpasses the prohibitive cost of calculating multi-reference eigenstates, and with its mean-field scaling, enables studying realistic magnets of unprecedentedly large size at an accuracy comparable to the previous state-of-the-art method.

Chapter 4 focuses on the locality in the rank structure of reduced density matrices (RDMs). The 1- and 2-RDMs are the crucial ingredients in estimating energies and observables in many classical and quantum simulation methods. Their intrinsic low-rank structure makes them compressible and can be exploited to significantly reduce the measurement cost. We analyze both noiseless and noisy measurement scenarios, including shot-noise-limited quantum algorithms, and show that in the context of Gaussian (shot) noise, a low-rank approximate reconstruction of RDMs effectively removes the high-rank noises and reduces the measurement cost by orders of magnitude, therefore enabling larger-scale simulations.

PUBLISHED CONTENT AND CONTRIBUTIONS

1. **Peng, L**, Liu, S., Zhang, X., Chen, X., Li, C., Cheng, H.-P. & Chan, G. K.-L. Accurate crystal field Hamiltonians of single-ion magnets at mean-field cost. *arXiv preprint arXiv:2505.16905.* doi:`10.48550/arXiv.2505.16905` (2025).
   Peng, L. contributed to the design of the study, to method and code developments, to numerical calculations, and to the writing of the manuscript.

2. Zhu†, T., **Peng†, L**, Zhai, H., Cui, Z.-H. & Chan, G. K.-L. Towards an exact electronic quantum many-body treatment of Kondo correlation in magnetic impurities. *arXiv preprint arXiv:2405.18709.* doi:`10.48550/arXiv.2405.18709` (2024).
   Peng, L. contributed to the design of the study, to method and code development, to numerical calculations, and to the writing of the manuscript.

3. **Peng, L**, Zhang, X. & Chan, G. K.-L. Fermionic reduced density low-rank matrix completion, noise filtering, and measurement reduction in quantum simulations. *Journal of Chemical Theory and Computation* **19,** 9151–9160. doi:`10.1021/acs.jctc.3c00851` (2023).
   Peng, L. contributed to the design of the study and to writing of the manuscript, developed the code, and performed the calculations.

4. Zhai, H., Larsson, H. R., Lee, S., Cui, Z.-H., Zhu, T., Sun, C., **Peng, L.**, Peng, R., Liao, K., Tölle, J., *et al.* Block2: A comprehensive open source framework to develop and apply state-of-the-art DMRG algorithms in electronic structure and beyond. *The Journal of Chemical Physics* **159,** 234801. doi:`10.1063/5.0180424` (2023).
   Peng, L. supported the software development and contributed to the method validation and the manuscript editing.

† These authors contributed equally to this work.

TABLE OF CONTENTS

LIST OF ILLUSTRATIONS

LIST OF TABLES

Chapter 1

INTRODUCTION

In 1929, P.A.M. Dirac remarked, "The underlying physical laws necessary for the mathematical theory of a large part of physics and the whole of chemistry are thus completely known, and the difficulty is only that the exact application of these laws leads to equations much too complicated to be soluble." [1] Since then, various approximations have been developed to solve the electronic Schrödinger equation: the Hartree-Fock theory [2] that yields the best single Slater determinant to approximate the electronic wavefunction; the density functional theory [3–5] that has been the routine workhorse to study chemical catalysis [6], energy materials [7], biological problems [8]; and the configurational interaction [9] and coupled cluster [10] expansions that provide a systematically improvable path towards exact solutions beyond the mean-field.

However, much challenge was sealed in this statement about the "only" difficulty. Nearly 100 years later, many realistic, strongly correlated materials remain too complicated to simulate. This class spans a wide range of systems, including transition metal oxides that exhibit high-temperature superconductivity [11] and Fe–S clusters of nitrogenase [12]. A common theme includes heavy elements with partially occupied d- or f-shells, such as transition metals and lanthanides. Because of this, their electronic eigenstates are usually of multi-reference characters, meaning that their eigenstate wavefunctions cannot be well described by a single dominant Slater determinant and its high-energy excitations and instead have small overlap with many near-degenerate Slater determinants. Advanced methods such as Complete Active Space Self-Consistent Field (CASSCF) method [13], complete active space perturbation theory (CASPT2) [14, 15], n-electron valence state perturbation theory (NEVPT2) [16, 17] and density matrix renormalization group (DMRG) [18–20] have been developed to predict their properties with high accuracy. However, they alone can be prohibitively expensive to study many realistic systems of experimental interest.

Developing methods to study these challenging systems, especially the realistic systems of large size and complicated structures, requires more refined approximations. A key to unlock efficiency from complexity is to tailor the approximation to the intrinsic locality in a physical problem, meaning some electrons or electronic states are "nearer," by some measure of distance, than others and thus interact more strongly. Given the spatial locality of electron correlations, as electronic interactions decay with distance, the distant parts of a system can be more heavily approximated with little loss of accuracy. Locality can lie in the energy spectrum, where only a narrow energy band of low-energy states dominates the physics and thus reduces the size of the Hilbert space for computation. Locality also manifests in the low-rank structure of the electron density matrices, allowing us to compress the information of the electronic wavefunction in a low-dimensional core. Taking advantage of these forms of locality inherent to the chemical systems can provide a unique opportunity to focus the limited computational resources on the most important part of the problem, overcome the "curse of dimensionality," and make it possible to simulate large, strongly correlated systems with accuracy and reduced computational cost.

In this dissertation, we will illustrate how we can take advantage of these three different types of locality concretely to develop methods that expand the boundary/complexity of systems one can compute. In the following, we will demonstrate how the *spatial locality* of the electron correlations allows the development and application of a quantum embedding theory to the Kondo physics, a many-body electronic problem in its full ab initio features, without the need to downfold into a simplified low-energy model. Secondly, we will discuss how the *locality in the energy spectrum* reduces the size of the Hilbert space of lanthanide single molecular magnets and thus allows accurate and efficient computation of excited states of molecular magnets unprecedentedly large. Thirdly, electronic density matrices usually have low rank; we take advantage of this *locality in rank* to reduce their degrees of freedom and thus their measurement cost.

The remaining dissertation is organized as follows. In Chapter 2, we extend the dynamical mean-field theory, a quantum embedding theory, to study the Kondo physics and systematically converge towards an exact zero-temperature electronic treatment of the Kondo correlations. We start by introducing the Kondo problem, a prototypical many-body electronic phenomenon where the strong electron correlations make simulations challenging, and then describe the numerical strategy to simulate it *ab initio* and converge towards the exact solution. We show that this approach provides chemical-specific predictions of the Kondo temperatures with quantitative agreement with experimental measurements and further shed light on their physical origin.

In Chapter 3, we develop a theoretical protocol to predict low-energy excitations in correlated lanthanide single-ion magnets with high accuracy comparable to CASPT2/NEVPT2 but with only the low scaling of HF and DFT. In these systems, the low-energy physics is dominated by excited states within a narrow spin-orbit manifold split by the weak crystal field interaction. We utilize the constrained DFT method to sample Slater determinants only within this local energy space, and then take advantage of the symmetry structure of this local space to predict the multi-reference eigenstates from the efficiently sampled non-eigenstates. Benchmarks on five experimental systems confirm the high accuracy of the method and the efficiency in studying unprecedentedly large, realistic lanthanide molecular magnets.

In Chapter 4, we take advantage of the low-rank structure of electronic reduced density matrices to reduce the measurement cost. Many classical and quantum simulation protocols require measurements of the reduced density matrices to calculate energies and properties. We study both situations where measurements of reduced density matrices are noiseless or noisy, and in the context of Gaussian noise, e.g., shot noise in quantum simulations, our method brings 1–3 orders of magnitude reduction in measurement cost.

References

1. Dirac, P. A. M. Quantum mechanics of many-electron systems. *Proceedings of the Royal Society of London. Series A, Containing Papers of a Mathematical and Physical Character* **123,** 714–733. doi:`10.1098/rspa.1929.0094` (1929).
2. Slater, J. C. A simplification of the Hartree-Fock method. *Physical Review* **81,** 385. doi:`10.1103/PhysRev.81.385` (1951).
3. Kohn, W. & Sham, L. J. Self-consistent equations including exchange and correlation effects. *Physical Review* **140,** A1133. doi:`10.1103/PhysRev.140.A1133` (1965).
4. Kohn, W. Nobel Lecture: Electronic structure of matter—wave functions and density functionals. *Reviews of Modern Physics* **71,** 1253. doi:`10.1103/RevModPhys.71.1253` (1999).
5. Parr, R. G. & Yang, W. *Density-Functional Theory of Atoms and Molecules* (Oxford University Press, New York, 1989).
6. Nørskov, J. K., Abild-Pedersen, F., Studt, F. & Bligaard, T. Density functional theory in surface chemistry and catalysis. *Proceedings of the National Academy of Sciences* **108,** 937–943. doi:`10.1073/pnas.1006652108` (2011).

7. Jain, A., Shin, Y. & Persson, K. A. Computational predictions of energy materials using density functional theory. *Nature Reviews Materials* **1,** 1–13. doi:`10.1038/natrevmats.2015.4` (2016).

8. Siegbahn, P. E. & Borowski, T. Modeling enzymatic reactions involving transition metals. *Accounts of Chemical Research* **39,** 729–738. doi:`10.1021/ar050123u` (2006).

9. Sherrill, C. D. & Schaefer III, H. F. in *Advances in Quantum Chemistry* 143–269 (Elsevier, 1999). doi:`10.1016/S0065-3276(08)60532-8`.

10. Shavitt, I. & Bartlett, R. J. *Many-body methods in chemistry and physics: MBPT and coupled-cluster theory* (Cambridge University Press, 2009).

11. Dagotto, E. Complexity in strongly correlated electronic systems. *Science* **309,** 257–262. doi:`10.1126/science.1107559` (2005).

12. Beinert, H., Holm, R. H. & Munck, E. Iron-sulfur clusters: Nature's modular, multipurpose structures. *Science* **277,** 653–659. doi:`10.1126/science.277.5326.653` (1997).

13. Roos, B. O., Taylor, P. R. & Sigbahn, P. E. A complete active space SCF method (CASSCF) using a density matrix formulated super-CI approach. *Chemical Physics* **48,** 157–173. doi:`10.1016/0301-0104(80)80045-0` (1980).

14. Andersson, K., Malmqvist, P.-Å., Roos, B. O., Sadlej, A. J. & Wolinski, K. Second-order perturbation theory with a CASSCF reference function. *Journal of Physical Chemistry* **94,** 5483–5488. doi:`10.1021/j100377a012` (1990).

15. Andersson, K., Malmqvist, P.-Å. & Roos, B. O. Second-order perturbation theory with a complete active space self-consistent field reference function. *The Journal of Chemical Physics* **96,** 1218–1226. doi:`10.1063/1.462209` (1992).

16. Angeli, C., Cimiraglia, R., Evangelisti, S., Leininger, T. & Malrieu, J.-P. Introduction of n-electron valence states for multireference perturbation theory. *The Journal of Chemical Physics* **114,** 10252–10264. doi:`10.1063/1.1361246` (2001).

17. Angeli, C., Cimiraglia, R. & Malrieu, J.-P. N-electron valence state perturbation theory: a fast implementation of the strongly contracted variant. *Chemical Physics Letters* **350,** 297–305. doi:`10.1016/S0009-2614(01)01303-3` (2001).

18. White, S. R. Density matrix formulation for quantum renormalization groups. *Physical Review Letters* **69,** 2863. doi:`10.1103/PhysRevLett.69.2863` (1992).

19. White, S. R. Density-matrix algorithms for quantum renormalization groups. *Physical Review B* **48,** 10345. doi:`10.1103/PhysRevB.48.10345` (1993).

20. Verstraete, F., Nishino, T., Schollwöck, U., Bañuls, M. C., Chan, G. K. & Stoudenmire, M. E. Density matrix renormalization group, 30 years on. *Nature Reviews Physics* **5,** 273–276. doi:`10.1038/s42254-023-00572-5` (2023).

Chapter 2

TOWARDS AN EXACT ELECTRONIC QUANTUM MANY-BODY TREATMENT OF KONDO CORRELATION IN MAGNETIC IMPURITIES

This chapter is based on the following publication:

1. Zhu†, T., **Peng†, L**, Zhai, H., Cui, Z.-H. & Chan, G. K.-L. Towards an exact electronic quantum many-body treatment of Kondo correlation in magnetic impurities. *arXiv preprint arXiv:2405.18709.* doi:`10.48550/arXiv.2405.18709` (2024).

† These authors contributed equally to this work.

2.1 Abstract

The Kondo effect is a prototypical quantum phenomenon arising from the interaction between localized electrons in a magnetic impurity and itinerant electrons in a metallic host. Although it has served as the testing ground for quantum many-body methods for decades, the precise description of Kondo physics with material specificity remains challenging. Here, we present a systematic *ab initio* approach to converge towards an exact zero-temperature electronic treatment of Kondo correlations. Across a series of $3d$ transition metals, we extract Kondo temperatures matching the subtle experimental trends, with an accuracy exceeding that of standard models. We further obtain microscopic insight into the origin of these trends. More broadly, we demonstrate the possibility to start from fully *ab initio* many-body simulations and push towards the realm of converged predictions.

2.2 Introduction

The Kondo system of a magnetic impurity embedded in a non-magnetic metallic host is a foundational quantum many-body materials problem [1–7]. As the temperature is decreased below a characteristic Kondo temperature T_{K}, the impurity moment is screened by the conduction electrons, forming a many-electron singlet state that manifests as a sharp resonance in the local density of states. Although the physics involves many-electron correlations in a bulk material, a qualitative understanding was achieved decades ago through the Anderson impurity model (AIM) [8] and via Wilson's numerical renormalization group (NRG) solution of the Kondo spin problem [9]. However, while deeply insightful, these model frameworks are limited in their quantitative precision due to the uncertainties in the specific model parameters and the neglect of higher-energy electronic degrees of freedom. In this work, we show that one can now describe Kondo physics without ever simplifying to such models, starting only with the *ab initio* many-electron Hamiltonian of the full material. In so doing, we present a precise material-specific treatment of the phenomenon, which can in principle be converged towards a numerically exact solution.

The challenge of the Kondo problem stems from the simultaneous presence of strong electron correlation leading to local singlet formation, and impurity-metal hybridization, which requires considering the thermodynamic limit. In addition, the Kondo energy scale is very small (typically 1 to 500 K). In low-energy models, one chooses a (small) set of impurity correlated orbitals (e.g., a few d or f orbitals), whose interactions are formally described by a downfolded effective Hamiltonian. Uncertainties, which are large on the Kondo scale, then arise from the choice and construction of these orbitals [10], the derivation of the effective interactions (and approximations to treat their complicated frequency dependence [11]), and the use of double-counting corrections to remove density functional theory (DFT) contributions [12, 13], in lieu of a fully many-body treatment of the local interactions. As a result, although much qualitative progress has been made in describing Kondo physics in different realistic settings [14–18], the accurate simulation of Kondo trends across different magnetic impurities, geometries, or even different calculations, without reference to experimental data, is challenging [15–17].

We will instead attempt to solve the *ab initio* many-electron Schrödinger equation for the Kondo problem without first deriving a low-energy model. This offers the advantage that it is often easier to quantify (and thus converge) errors in the approximate solution of a problem, than the error associated with deriving a model. We build on our work on full cell embedding in the context of dynamical mean-field theories [19–23] to construct a systematically improvable representation of the impurity in its metallic host. Solving the many-body problem in this representation, as we increase the number of orbitals in the parent basis, we eventually obtain the exact non-relativistic description of the pure electronic problem. In small molecules [24], as well as in simple materials (such as organic crystals [25]), it has been established that for the quantities of interest, related strategies can reach an accuracy rivalling, or even exceeding, that of experimental measurements. We thus ask, how far can we go with a similar philosophy for a realistic correlated quantum materials problem?

A major technical challenge is to solve for the impurity properties given the large number of electronic orbitals. We achieve this by implementing a highly-parallel quantum chemistry density matrix renormalization group (DMRG) eigenstate and Green's function solver [26, 27]. The use of delocalized (i.e., molecular orbital) representations reduces the entanglement and allows us to converge the many-body solvers. Within our framework, we simulate the series of seven $3d$ magnetic impurities (Ti, V, Cr, Mn, Fe, Co, Ni) in a bulk copper host at zero and finite temperatures, computing quantities such as the local density of states and quasiparticle (QP) renormalization, excited states, orbital occupancies, and spin correlations. Using the QP renormalization and orbital occupancies as sensitive metrics, we demonstrate convergence of our simulations to the parent basis solution, and estimate the remaining error in the parent basis. Extracting the Kondo temperature from the quasiparticle renormalization, the converged simulations capture subtle trends across the $3d$ series as seen in experiments (Fig. 2.1b), give new insights into the element-specific mechanisms, and improve predictions from models that use standard parametrizations by an order of magnitude or more. They thus demonstrate the potential of approaches based on fully *ab initio* simulations in the interpretation of complex correlated electron phenomena.

2.3 Numerical strategy

Our basic plan is to describe the magnetic impurity atom with as complete a basis of electronic orbitals as practical in an impurity-bath embedding setup (Fig. 2.1a). As the impurity orbital space is increased, it formally converges to the Hilbert space of the material and thus to an exact electronic description (i.e., phonon effects are excluded); for any finite impurity space, the bath approximates the neglected degrees of freedom in the material. While achieving convergence for bulk properties would require including orbitals that span the electronic space of all atoms of the material, here we are focused on observables on the impurity, where convergence of an impurity-centered basis expansion is more rapid. Converging the representation in this way means that we do not need to first downfold the Hamiltonian to derive a model.

More specifically, we study the series of seven $3d$ transition metal impurities (Ti, V, Cr, Mn, Fe, Co, Ni) in bulk Cu, with associated Kondo temperatures that span three orders of magnitude. We started from a Gaussian atomic orbital representation of all atoms: a split-valence double-ζ polarization basis (def2-SVP) [28] for the impurity atoms and a slightly smaller (def2-SV(P)) basis for Cu (which omits the $4f$ basis shell). The def2-SVP basis for the impurity atoms contains the $1s2s2p3s3p3d4s4p4d4f5s$ shells (denoted a $5s3p2d1f$ basis, from the shell-count) and thus goes significantly beyond the $3d$ shell considered in a model Hamiltonian treatment. To test the convergence of the results, for a subset of the calculations we also used a larger cc-pVTZ basis [29] on the impurity atom, corresponding to a $7s6p4d2f1g$ basis. This further improves the electronic treatment of the impurity. We will refer to these as the parent bases and below we demonstrate convergence towards the exact solutions within the parent bases. We estimate the remaining error of the parent basis by the difference between the def2-SVP and cc-pVTZ results.

Starting from DFT-optimized XCu$_{63}$ structures (X = impurity), we performed periodic DFT calculations in the Gaussian atomic orbital bases with the PBE functional [30, 31]. The Gaussian basis functions were then transformed into an orthogonal basis of intrinsic atomic orbitals plus projected atomic orbitals (IAO+PAO) [32]. The impurity IAOs and PAOs are visualized in Fig. 2.1a. The higher shell orbitals in this picture extend away from the impurity atom onto the neighbours, and because of the close packing of the atoms, start to capture important electronic degrees of freedom of the atoms neighbouring the impurity. For example, using the Löwdin population to measure the spatial extent of the $4s$ orbital of an Fe impurity, we find that it is close to 66% on the neighbouring Cu atoms in FeCu$_{63}$. The large basis sets may thus be viewed as forming an "impurity-centered" basis expansion, similar to well-studied local correlation treatments in quantum chemistry.

The impurity-bath embedding Hamiltonian takes the form

$$H_{\text{emb}} = \sum_{ij}^{\text{imp}} \tilde{F}_{ij} a_i^\dagger a_j + \frac{1}{2}\sum_{ijkl}^{\text{imp}} (ij|kl) a_i^\dagger a_k^\dagger a_l a_j + \sum_{ip} V_{ip}(a_i^\dagger c_p + c_p^\dagger a_i) + \sum_p \epsilon_p c_p^\dagger c_p \tag{2.1}$$

where the impurity sum extends over all IAOs and PAOs in the impurity basis, $\{a_i^{(\dagger)}\}$ are creation/annihilation operators for impurity states, and $\{c_p^{(\dagger)}\}$ are creation/annihilation operators for bath states. The impurity Coulomb interaction matrix $(ij|kl)$ is taken as the bare Coulomb interaction in the IAO+PAO basis, while the impurity one-particle interaction $\tilde{F}_{ij}$ in Eq. 2.1 is defined as the Hartree-Fock effective Hamiltonian with the local mean-field potential subtracted (this subtraction is diagrammatically exact, so there is no double counting). All interactions are treated non-relativistically (spin-orbit coupling is beyond the scope of this work). The impurity-metal hybridization function $\Delta(\omega)$ was obtained at the PBE level. Since we used a Hamiltonian-based impurity solver, we discretized the $3d4s$ valence block of the hybridization function on a non-uniform grid along the real frequency axis [33]

$$\Delta_{ij}(\omega) = \sum_p \frac{V_{ip}V_{jp}}{\omega - \epsilon_p}, \; ij \in 3d4s \tag{2.2}$$

where $\{\epsilon_p\}$ and $\{V_{ip}\}$ are the bath energies and impurity-bath couplings in Eq. 2.1. We used 49 bath orbitals to couple to each valence impurity orbital. The total embedding problem thus consisted of 300 electrons in 316 (impurity plus bath) orbitals using the impurity def2-SVP basis, denoted (300e, 316o), and 300 electrons in 353 orbitals using the impurity cc-pVTZ basis, denoted (300e, 353o).

To compute and converge the impurity Green's function, we constructed a series of smaller orbital spaces (active spaces) that are subspaces of the full orbital space of the embedding problem. We then monitored the convergence of the eigenstate and dynamical quantities as a function of the active space size. The active spaces were defined to span natural orbitals (eigenvectors of the one-particle density matrix) of an (approximate) ground state of the impurity problem, taking natural orbitals with the largest orbital entropy (a procedure which has been shown to yield highly compact orbital subspaces in model impurity problems [35]). We used active spaces of up to (36e, 52o) for the ground-state problem in the impurity def2-SVP basis and (46e, 76o) in the impurity cc-pVTZ basis, and up to (26e, 36o) for the dynamical properties and the finite temperature simulations. We computed ground states and associated properties (e.g., density matrices and correlation functions), and as many as several hundred excited states, using *ab initio* DMRG [26, 27, 36]. For dynamical properties, we used a new zero-temperature *ab initio* dynamical DMRG (DDMRG) solver to compute the impurity self-energy on the real frequency axis [27, 37]. (Benchmarks of the DDMRG solver on the single-impurity Anderson model are shown in Supplementary Note 2).

2.4 Convergence towards parent basis and an exact simulation

We first consider the Fe impurity to illustrate general features of the results. In Fig. 2.1c we show the orbital-resolved excitation spectra and self-energies of the Fe $3d$ orbitals. As expected, we see sharp Kondo resonance peaks, also known

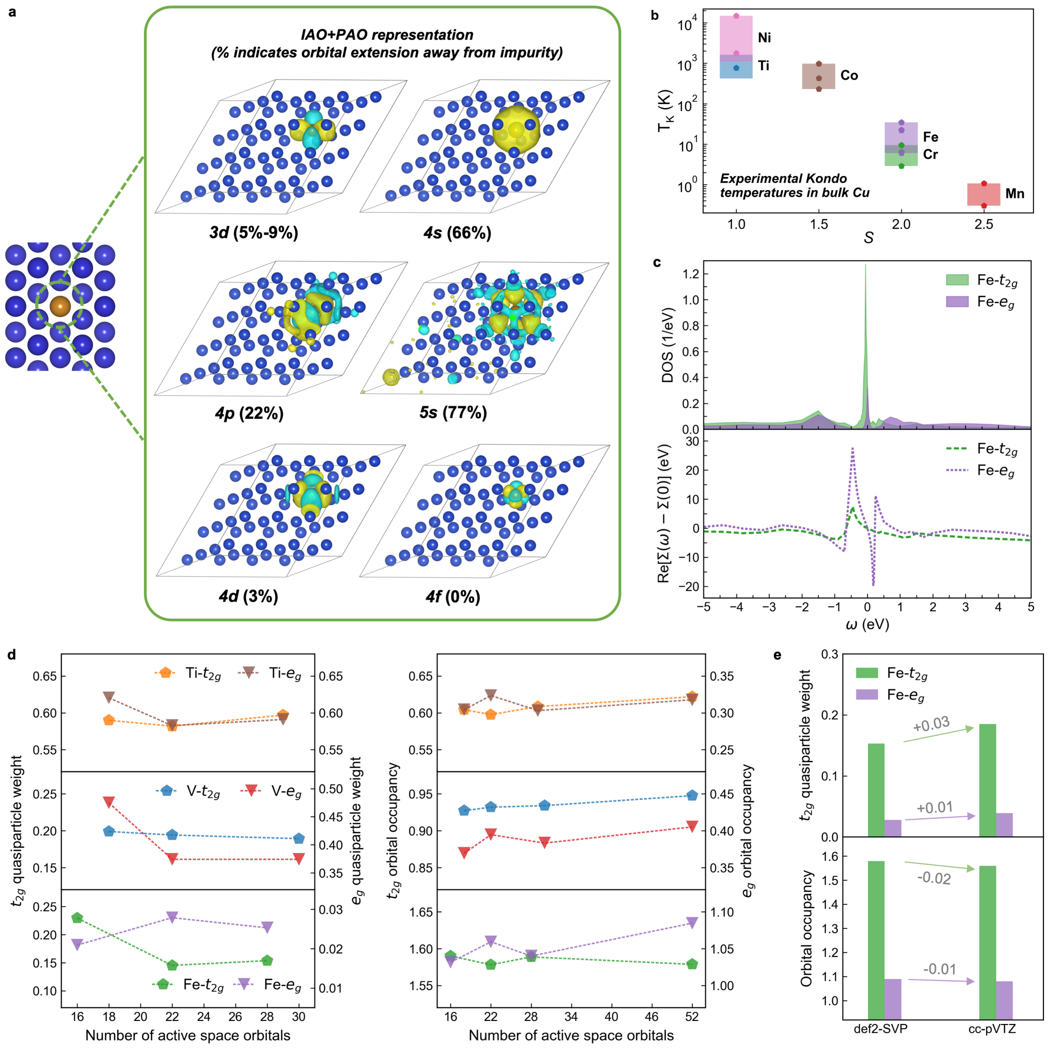

Figure 2.1: Illustration and validation of computational strategy. (a) All-orbital quantum embedding strategy, where general Coulomb interactions between all valence and high-virtual orbitals of the impurity atom are treated at the quantum many-body level. The percentage of orbital extension onto neighbouring Cu atoms is estimated through a Löwdin population analysis. (b) Experimentally measured Kondo temperatures for 3d transition metal impurities in bulk Cu. Each dot corresponds to a distinct measurement, while the shaded areas illustrate the range of Kondo temperatures from different observables and their associated measurement uncertainties (where applicable) [34]. The x-axis shows the nominal spin (S) of the isolated impurity atoms. (c) Simulated Kondo resonance and self-energies of the t_{2g} and e_g orbitals of the Fe impurity with an active space of (22e, 22o) in the def2-SVP basis. (d) Estimated convergence of the quasiparticle renormalization weights and orbital occupancies of the t_{2g} and e_g orbitals, averaged within each manifold, of Ti, V, and Fe impurities as the DMRG active space increases in the def2-SVP basis. (e) Comparison of quasiparticle renormalization weights and orbital occupancies of 3d orbitals of the Fe impurity calculated in the def2-SVP basis versus the cc-pVTZ basis.

as Abrikosov-Suhl resonances [38], around the Fermi level for both the t_{2g} and e_g orbitals, with broad Hubbard shoulder peaks at higher energies. We find that the Fe-e_g Kondo peak is narrower and smaller than the Fe-t_{2g} peak from the stronger QP renormalization, which can also be seen from the real part of the real-axis self-energies shown in Fig. 2.1c. The imaginary part of the real-axis self-energies of both the t_{2g} and e_g orbitals approaches zero at the Fermi level (Fig. S5), i.e., $\mathrm{Im}\Sigma(T = 0, \omega) \to 0$ as $\omega \to 0$. The splitting of the Hubbard peaks is roughly $2.5 \sim 3$ eV (in the range of the screened interaction for Fe $3d$ orbitals [39]) and is slightly smaller for the t_{2g} orbitals than for the e_g orbitals.

We then examine the convergence of impurity observables towards the parent basis limit. In Fig. 2.1d, we show the orbital-resolved QP renormalization weight Z (calculated on the real axis as $\left[1 - \left.\frac{\partial \Sigma(\omega)}{\partial \omega}\right|_{\omega=0}\right]^{-1}$) and the orbital occupancy n of the $3d$ orbitals, for the Ti, V, and Fe impurities, as a function of active space size with a parent def2-SVP basis. Additional convergence data are in the Supplementary Notes 3 and 4, including the convergence with respect to the DMRG bond dimension (for which the uncertainty is substantially smaller than the uncertainty from the active space for all cases other than Mn). We observe that the QP weight is clearly more challenging to converge. Examining the full series of elements (Supplementary Notes 3 and 4) we conservatively estimate that, with the exception of Mn, n is converged to at least ~ 0.04 and Z to at least ~ 0.05 of the exact parent basis result. The latter exception arises because it was difficult to fully converge the DMRG calculations in the largest active spaces for Mn.

Beyond these errors, the primary source of deviation from an exact simulation comes from the insufficiency of the parent basis itself. To estimate the error from the parent basis, in Fig. 2.1e we show the change in Z and n as we increase the parent basis from def2-SVP to cc-pVTZ, for the Fe impurity. We see that both quantities change by less than ~ 0.03. Standard quantum chemistry arguments suggest that most quantities converge like the inverse cube of the cardinal number of the basis [40] (2 in the case of def2-SVP, 3 for cc-pVTZ), which indicates that Z and n are well converged with respect to the representation of the electronic degrees of freedom of the Fe impurity and its close neighbours. Only the contribution from fluctuations involving long-range Coulomb interactions beyond the closest neighbours remains outside of our treatment and this error analysis.

2.5 Detailed Kondo temperature trends and mechanisms

Having examined the convergence of our numerical results, we now study the trends in Kondo physics across the series of 7 elements. For $3d$ magnetic impurities in bulk Cu, experiments observe an exponential decay in Kondo temperatures moving from nominally low-spin (e.g., Ti) to high-spin (e.g., Mn) impurities [34]. The estimated experimental Kondo temperatures for the $3d$ magnetic impurities, along with the nominal spins S of the atom, are shown in Fig. 2.1b. Note that the experimental estimates of T_{K} involve significant interpretation (for a full discussion see Ref. [34]) and thus a range of characteristic temperatures are obtained depending on the type of measurement and method to extract T_{K}.

We estimate theoretical Kondo temperatures from Hewson's renormalized perturbation theory of the Anderson impurity model [41]

$$T_{\mathrm{K}} = -\frac{\pi}{4} Z \cdot \mathrm{Im}\Delta(0). \tag{2.3}$$

Here $\Delta(0)$ is the hybridization function at the Fermi level and Z is the QP renormalization weight on the real axis (Fig. S4 and Table S6). Hewson's formula gives separate estimates of T_{K} for the e_g and t_{2g} orbitals; the lower of the two Kondo temperatures is the relevant one for the comparison to measurements (see, e.g., Ref. [42] for resistivity).

Our predicted Kondo temperatures for all the studied elements are shown in Fig. 2.2c. We capture the trend in T_{K} across the full set of elements in good agreement with the experimental estimates, and reproduce subtle differences such as the relative ordering of the lowest Kondo temperatures $T_{\mathrm{K}}(\mathrm{Cr})$, $T_{\mathrm{K}}(\mathrm{Mn})$, $T_{\mathrm{K}}(\mathrm{Fe})$. With the exception of Cr and Mn, the range of our predicted T_{K} is within a factor of 2∼3 of at least one of the experimental estimates of T_{K}. As our calculations do not include long-range Coulomb fluctuations (beyond those captured by the basis extending to neighbouring atoms), this suggests that they do not contribute significantly at this level of accuracy. On the other hand, Mn, which has the lowest T_{K}, is a system where we could not achieve numerical convergence of our results to the parent basis. This is the likely origin of the larger quantitative discrepancy for Mn.

Conventionally, the origin of the observed trend in T_{K} is ascribed to strong Hund's coupling in the impurity spins. In particular, when we represent the system by a multi-spin Kondo model, in the strong coupling limit the impurity spins are locked, which reduces the space of fluctuations and the effective exchange coupling J_{eff} [43, 44] (see Supplementary Note 15 for a brief summary). Fixing the metallic host, and

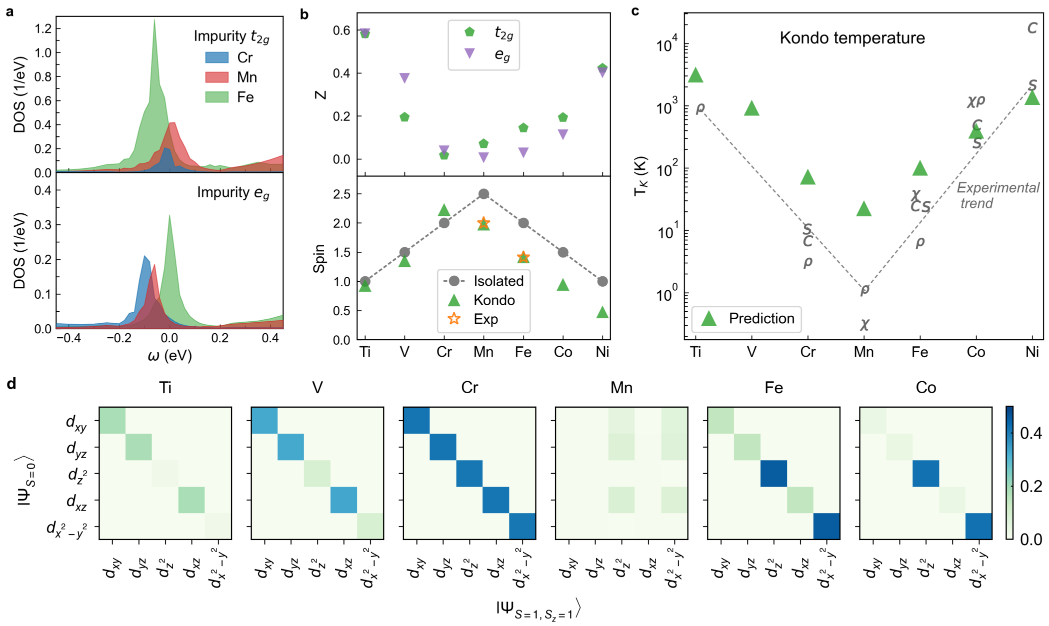

Figure 2.2: Trends in impurity DOS, quasiparticle renormalization, spin moment, Kondo temperature, and orbital character of the lowest triplet excited state. All results are in the def2-SVP basis with ground-state active space of (36e, 52o) and Green's function active space of (22e, 22o). (a) Comparison of DOS of 3d orbitals of Cr, Mn, and Fe impurities. (b) Top: Orbital-resolved quasiparticle renormalization weights Z. Bottom: Local spin moments of impurity atoms compared to nominal spins of isolated atoms and experimental values. (c) Kondo temperatures from all-orbital simulations, estimated by zero-temperature Green's function calculations using Hewson's formula, compared to experimental values [34]. The experimental trend lines are provided as a visual aid. Symbols for each type of measurement are: ρ: resistivity, χ: susceptibility, C: specific heat, S: thermoelectric power. (d) Orbital-resolved spin-flip transition density matrix for the lowest triplet excited state $|\langle\Psi_{S=0}|c^{\dagger}_{i\downarrow}c_{j\uparrow}|\Psi_{S=1,S_z=1}\rangle|$ within the impurity 3d subspace.

assuming all other effects are the same for different impurities, this Hund's driven relation can be simplified to

$$T_{\mathrm{K}} \propto \exp(-1/J_{\mathrm{eff}}) \propto \exp(-S), \tag{2.4}$$

where S is the spin of the magnetic atom. The above theoretical form gives qualitative agreement with the experimental data, as shown by the trend in Fig. 2.1b. However, it also misses quantitative differences between certain magnetic impurities. For example, it does not explain why the T_{K} of Cr (3~10 K) is lower than the T_{K} of Fe (30 K), if we consider both Cr and Fe atoms to have nominal $S = 2$. Given that our *ab initio* simulations faithfully reproduce the experimental trend in Kondo temperatures, we can now examine the Hund's suppression mechanism within our calculations.

We start with the computed local ground-state properties of the impurity, such as the t_{2g} and e_g orbital occupancies across the impurity elements (Table S7) and the effective spin (extracted from $\langle S^2 \rangle$) in Fig. 2.2b. (Fig. 2.2a further illustrates the t_{2g} and e_g resolved DOS for Cr, Mn, Fe). Charge transfer takes place to the impurity atom in all systems, giving negatively charged $3d$ shells compared to the isolated impurities. For instance, we find Fe in bulk Cu to be on average in a d^7 occupancy ($n_{\mathrm{Fe}}(3d) = 6.92$), in excellent agreement with recent experimental estimates [45]. The strong QP renormalization in Fig. 2.2b tracks the partially-filled nature of the impurity $3d$ orbitals. For example, we obtain $n(t_{2g}) = 0.99$ in Cr and $n(e_g) = 1.03$ in Mn (i.e., very close to half filling), which correlates well with their very small QP weights.

As a result of the charge transfer, the local spin moments of the magnetic impurities differ from their isolated-atom values (Fig. 2.2b). For Mn, Fe, Co, and Ni, we predict $S = 1.99, 1.42, 0.95, 0.48$, about 0.5 lower than the isolated-atom spins. These S values agree well with the available experimental data for Mn and Fe [34, 45, 46]. Cr has the highest spin moment ($S = 2.23$) among all $3d$ transition metal impurities, which deviates from the common understanding of this Kondo series [4], but is also supported by experimental measurements that suggest Cr is a high-spin impurity ($S = 5/2$) [46, 47].

Taking into account the quantitative differences in the observed S in the Kondo systems and the isolated atoms, our results partially confirm a Hund's driven suppression mechanism. With the exception of the relative ordering of $T_{\mathrm{K}}(\mathrm{Cr})$ and $T_{\mathrm{K}}(\mathrm{Mn})$, higher observed S indeed correlates with lower T_{K}. For example, accounting for the charge transfer to Fe and Cr that modifies their effective spin, we can predict the observed relation $T_{\mathrm{K}}(\mathrm{Cr}) < T_{\mathrm{K}}(\mathrm{Fe})$. The Hund's picture can further be confirmed by examining the nature of the lowest triplet excited states which are associated with the destruction of the Kondo singlet. As seen in Fig. 2.2d, for most of the elements, the main character of the excitation is a coherent spin-flip of all the (close to) singly occupied d orbitals, as expected in the limit of strong Hund's coupling.

The exception to this is Mn. Note that from the computed effective spin, the Hund's mechanism would predict Cr to have a lower T_K than Mn, contrary to the experimental findings. However, after charge transfer, the Mn ion has an excess (0.66) electron in the t_{2g} shell, which experiences an unfavourable repulsion. We find that the lowest triplet excitation corresponds to a partial transfer of an electron from t_{2g} to the bath, accompanied by a spin-flip (see Supplementary Note 13). The low energy of this triplet state recalls the double-exchange mechanism [48], which favours same-spin alignment to enable charge delocalization. In fact, in our calculations, other than for Cr (which has a close to exactly half-filled d-shell when embedded in Cu) this type of excitation occurs at low energy in all the elements, but is especially low in energy for Mn. The inclusion of orbital degrees of freedom is thus an important part of the systematic trends in the Kondo temperatures, not only through the effective spin, but also through fluctuations.

Some additional insight is provided by examining the detailed contributions to Hewson's formula. Because it starts from a Fermi liquid it naturally captures some effects omitted in the Kondo model, such as the effect of charge fluctuations and the crystal field splitting. Generally, the lower of the $T_\mathrm{K}(t_{2g})$ and $T_\mathrm{K}(e_g)$ estimates corresponds to the shell with the most unpaired electron character, consistent with a Kondo model where the impurity is replaced by a spin. However, for impurities where both t_{2g} and e_g have significant unpaired electron character (such as in Cr) the Hewson formula further identifies which shell gives rise to the lower Kondo temperature. We find that the Kondo energy scales of Mn, Fe, Co, and Ni are associated with e_g, while they are associated with t_{2g} for Cr, V, and Ti. As $\Delta(0)$ only varies slightly across the series (from −0.59 eV (Ti) to −0.43 eV (Fe) for the t_{2g} orbital and from −0.64 eV (Ti) to −0.38 eV (Ni) for the e_g orbital), the trend is generated primarily by the QP renormalization weight, which contains both the Hund's coupling mechanism as well as the effect of charge fluctuations.

2.6 Comparison to low-energy models

Finally, to place the fidelity of our results in perspective, we check to see if the above predictions are easily captured within a standard application of the downfolded model approach. For this, we employ a five-orbital Anderson impurity model using the Kanamori Hamiltonian [44, 49] with screened Coulomb interaction and exchange parameters U and J taken from constrained random phase approximation (cRPA) calculations [50]. (Note these parameters are also very close to previous parameters used in other model Kondo studies, e.g., for Co in Cu [15, 18]). We employed the

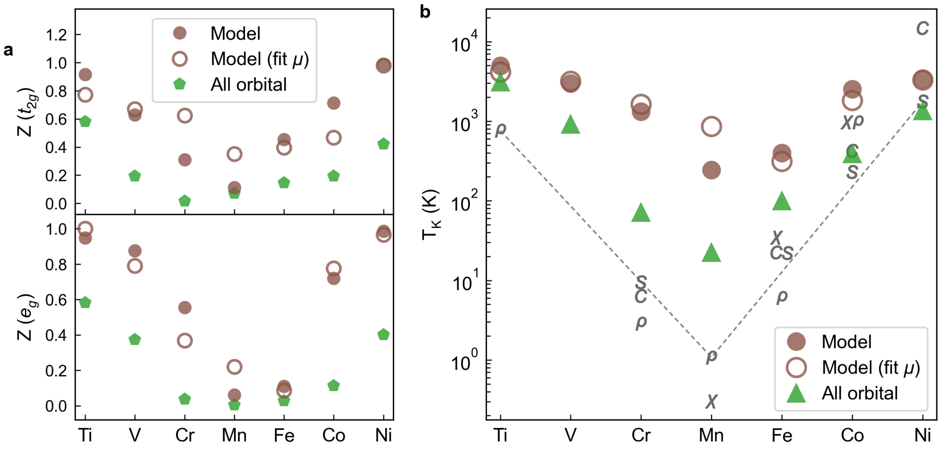

Figure 2.3: Comparison of *ab initio* all-orbital simulations with model simulations using either the same chemical potentials ("Model") or fitted chemical potentials to match the total $3d$ orbital occupancy of the all-orbital simulations ("Model (fit μ)"). (a) Orbital-resolved quasiparticle renormalization weights. (b) Predicted Kondo temperatures compared to the experimental estimates.

same valence hybridization, bath discretization, and active-space DMRG solvers described above. The model was tested using both the same chemical potentials as in the all-orbital calculations, and refitted ones to match the total $3d$ orbital occupancies in the all-orbital results. Further details and analysis are given in Supplementary Notes 10 and 11. Fig. 2.3 shows the estimated Kondo temperatures and quasiparticle renormalizations obtained from this model. We find that the quasiparticle renormalization weights of most magnetic impurities are significantly overestimated compared to our all-orbital simulations. As a result, the predicted T_{K}'s do not even show a clear exponential trend, with a large overestimation of T_{K}. In addition, the relative T_{K}'s of Cr, Mn, and Fe, are not reproduced using either the same chemical potential as in the *ab initio* all-orbital calculations, or the refitted chemical potential. The quantitative improvement in the Kondo temperatures moving from the model to *ab initio* calculations is as much as 2 orders of magnitude. Our standard model includes the density-density, spin-flip, and pair-hopping interactions in rotationally invariant form. In principle, a model that allows for all possible terms in the $3d$ shell, together with their full frequency dependence, should yield better estimates of the Kondo temperatures [18]. However, determining such a large number of downfolded parameters is challenging.

2.7 Discussion

We have demonstrated the predictive power of *ab initio* quantum many-body simulations in the prototypical Kondo physics materials problem, namely, that of $3d$ transition metal impurities in bulk copper. By converging the material description and many-body treatment, we could reach an accuracy for the Kondo temperature that captures the subtle experimental trends across the $3d$ transition metal series.

In contrast to previous approaches, we achieved this accuracy by performing the quantum many-body simulations of the bare electronic problem with all orbitals, rather than within a downfolded model. This allows for a straightforward control of many aspects of converging our results towards an exact description of the phenomena. Within the zero-temperature electronic picture of our work, the physics of very long-range Coulomb fluctuations remain as an uncontrolled uncertainty, although these effects appear to be small on the scale of our results. However, our computational framework does not lie in opposition to model approaches. In particular, we showed how, after establishing the faithfulness of the physics within our framework, we can extract understanding in terms of traditional low-energy pictures. Moving forwards, the accuracy achieved here suggests that with continuing advances, we may move beyond qualitative descriptions of correlated electron phenomena, towards a systematically improvable simulation of observables directly measured by experiments.

2.8 Appendix

Computational methods

We generated initial XCu_{63} (X = Ti, V, Cr, Mn, Fe, Co, Ni) structures by replacing one Cu atom in a $4 \times 4 \times 4$ supercell of bulk Cu with an impurity atom. We carried out DFT geometry relaxations for all XCu_{63} structures with the PBE functional and projector-augmented-wave (PAW) basis using the Vienna Ab initio Simulation Package (VASP) [51, 52]. The calculations were performed with a plane wave cutoff of 400 eV and a Γ-centered $3 \times 3 \times 3$ $\mathbf{k}$-mesh. The forces on each atom were converged to less than 0.01 eV/Å. With DFT-optimized structures, we performed single-point DFT calculations with the PBE functional in a periodic Gaussian basis set using the PySCF quantum chemistry software package [31]. We employed a split-valence double-ζ polarization basis (def2-SVP) for all impurity atoms and a split-valence double-ζ basis (def2-SV(P)) for Cu [28]. The correlation-consistent polarized triple-ζ basis (cc-pVTZ) was also employed for the Fe impurity to test the parent basis convergence [29]. The libDMET code [20, 22] was used to transform mean-field Fock matrix, density matrix, and electron repulsion integrals to the intrinsic atomic orbital plus projected atomic orbital (IAO+PAO) basis [32]. $3d4s$ atomic orbitals of all metal atoms were used as the predefined valence (minimal) orbitals in the IAO+PAO construction.

We incorporate the full impurity atom into the embedding problem. In the IAO+PAO basis, the $3d4s4p4d4f5s$ (def2-SVP) and $3d4s4p4d4f5s5p5d5f5g6s6p6d7s7p$ (cc-pVTZ) orbitals of the impurity atoms were treated in the many-body impurity solvers, while the $1s2s2p3s3p$ orbitals were frozen at the mean-field level and left out of the embedding problem. The fcDMFT code [19, 21, 53] was used to perform the all-orbital calculations. We employed the bare Coulomb interaction $(ij|kl)$ within the impurity as the two-particle interaction matrix in the embedding Hamiltonian in Eq. 2.1. The one-particle impurity interaction matrix in Eq. 2.1 is defined as

$$\tilde{F}_{ij} = F_{ij}^{\text{imp}} - \sum_{kl\in\text{imp}} \gamma_{kl}^{\text{imp}}[(ij|lk) - \frac{1}{2}(ik|lj)], \tag{2.5}$$

where F^{imp} is the impurity Fock matrix computed by Hartree-Fock using the PBE density, and γ^{imp} is the impurity block of PBE density matrix. This definition ensures that there is no double counting in the impurity Hamiltonian.

The hybridization function for each impurity atom was obtained at the PBE level using a $4 \times 4 \times 4$ $\mathbf{k}$-point sampling of the XCu_{63} supercell:

$$\Delta(\omega + i\delta) = \omega + i\delta - F_{\text{imp}} - G_{\text{imp}}^{-1}(\omega + i\delta), \tag{2.6}$$

where δ is the broadening factor taken to be $\delta = 0.01$ Ha. Since Hamiltonian-based impurity solvers (that require a bath) were employed, we discretized the $3d4s$ block of the hybridization function on a non-uniform grid along the real frequency axis using a pole-merging direct discretization method [33] to obtain bath energies $\{\epsilon_p\}$ and impurity-bath couplings $\{V_{ip}\}$ in Eq. 2.1, and 49 bath orbitals were coupled to each of the $3d4s$ valence orbitals. Among these 49 bath orbitals, 5 orbitals were placed within a $\mu \pm 0.027$ eV energy window, 18 orbitals were placed within the $[\mu \pm 0.027, \mu \pm 0.6]$ eV energy window, and the remaining 26 orbitals were placed at a higher energy window of $[\mu \pm 0.6, \mu \pm 8.0]$ eV. In total, the embedding problem contained 22 (impurity) + 294 (bath) = 316 orbitals in the def2-SVP impurity basis calculations. The same bath discretization procedure was applied to the cc-pVTZ impurity basis calculation of the Fe impurity, resulting in an embedding problem of 59 (impurity) + 294 (bath) = 353 orbitals.

To solve the embedding Hamiltonian, we first performed a Hartree-Fock calculation with the chemical potential fixed at the supercell DFT value, to define the number of electrons in the embedding problem. We note that the value of the chemical potential is often chosen to tune the orbital fillings, but we found that the current strategy gave excellent agreement with experimental occupancies of Mn and Fe. Following the HF solution, we carried out a configuration interaction with singles and doubles (CISD) calculation and computed natural orbitals by diagonalizing the CISD one-particle density matrix. A (36e, 52o) natural-orbital active space was then derived in the def2-SVP impurity basis calculations ((36e, 46o) for Ni, (46e, 76o) in the cc-pVTZ impurity basis calculation of Fe), where all kept natural orbitals have eigenvalues n_i that satisfy $\min(n_i, 2 - n_i) > 10^{-7}$. An *ab initio* quantum chemistry DMRG calculation was then conducted on this active space to obtain ground-state properties including one-particle and two-particle density matrices and spin-spin correlation functions. The DMRG calculation was done with a bond dimension of $M = 3500$ ($M = 4000$ for Mn and Fe) using the block2 code [26, 27], where the discarded weight was below 2×10^{-5} in all ground-state DMRG calculations. We further derived a series of smaller natural-orbital active spaces from the DMRG density matrix (see Supplementary Note 3 for details). The dynamical DMRG (DDMRG) [37] calculation was carried out for the smaller active spaces with a bond dimension up to $M = 1500$ along the real axis at zero temperature. Larger bond dimensions of up to $M = 4000$ were employed for strongly correlated sites to ensure that the discarded weight in the DDMRG calculations was below 0.02. To accommodate the non-uniform bath discretization, we used a broadening factor of $\eta = 0.02$ eV within the $\mu \pm 0.25$ eV energy window, $\eta = 0.05$ eV within the $[\mu \pm 0.25, \mu \pm 0.5]$ eV energy window, $\eta = 0.2$ eV within the $[\mu \pm 0.5, \mu \pm 2.0]$ eV energy window, and $\eta = 0.6$ eV within the $[\mu \pm 2.0, \mu \pm 5.0]$ eV energy window in the DDMRG calculations.

From the DDMRG calculations, we extracted the self-energy of the active space $\Sigma_{\text{DMRG,act}}(\omega)$ as

$$\Sigma_{\text{DMRG,act}}(\omega) = G^{-1}_{\text{DFT,act}}(\omega) - G^{-1}_{\text{DMRG,act}}(\omega), \tag{2.7}$$

where $G_{\text{DFT,act}}$ was calculated from the effective DFT Hamiltonian rotated to the active space. The active-space self-energy was then rotated back to the full embedding space

$$\Sigma_{\text{DMRG,emb}}(\omega) = C^{\text{emb,act}} \Sigma_{\text{DMRG,act}}(\omega) (C^{\text{emb,act}})^{\dagger}, \tag{2.8}$$

where $C^{\text{emb,act}} = C^{\text{CISD}} C^{\text{DMRG}}$. Here, C^{CISD} represents the rotation matrix from the full embedding space to the natural-orbital active space derived from CISD calculations, while C^{DMRG} represents the rotation matrix from the CISD active space to the natural-orbital active space derived from ground-state DMRG calculations. Finally, the local Green's function of the impurity was calculated from Dyson's equation

$$G_{\text{loc}}(\omega) = [G^{-1}_{\text{DFT,emb}}(\omega) - \Sigma_{\text{DMRG,emb}}(\omega)]^{-1}. \tag{2.9}$$

Benchmark of DDMRG solver on Anderson impurity model

We benchmark the accuracy of the active-space DMRG and dynamical DMRG (DDMRG) solvers on a single-impurity Anderson model (SIAM), the fundamental model of Kondo physics, where high-accuracy numerical results are available (e.g., from NRG [54] or DMRG [55]). The Hamiltonian of the SIAM is

$$H = \sum_{\sigma} \epsilon_f f^{\dagger}_{\sigma} f_{\sigma} + U f^{\dagger}_{\uparrow} f_{\uparrow} f^{\dagger}_{\downarrow} f_{\downarrow} + \sum_{k\sigma} \epsilon_k c^{\dagger}_{k\sigma} c_{k\sigma} + \sum_{k\sigma} V_k (f^{\dagger}_{\sigma} c_{k\sigma} + c^{\dagger}_{k\sigma} f_{\sigma}), \tag{2.10}$$

where $f^{(\dagger)}_{\sigma}$ are creation/annihilation operators for impurity states with spin σ and energy ϵ_f, $c^{(\dagger)}_{k\sigma}$ are creation/annihilation operators for band states with spin σ and energy ϵ_k, U is the impurity on-site Coulomb interaction, and V_k are the k-dependent coupling between impurity and band states. We followed Ref. [54] and employed the flat-band hybridization function:

$$\text{Im}\Delta(\omega + i0^+) = -0.015D, \ |\omega| < D \tag{2.11}$$

where $2D$ is the conduction electron bandwidth. For convenience, we set $D = 1$. The flat-band hybridization on a logarithmic grid was then discretized along the real axis to obtain $\{\epsilon_k, V_k\}$:

$$-\text{Im}\Delta(\omega + i0^+) = \sum_k \frac{V_k^2}{\omega - \epsilon_k}. \tag{2.12}$$

We coupled 39 bath orbitals to the single impurity orbital. Furthermore, only the half-filling case was considered, which means $\epsilon_f = -\frac{1}{2}U$. We tested our impurity solver on three interaction strengths: $U = 0.1, 0.2, 0.3$.

We first solved the SIAM Hamiltonian using the Hartree-Fock approximation to determine an initial set of orbitals. Within this (untruncated basis) we subsequently carried out a ground-state configuration interaction with single and double excitations (CISD) calculation or a ground-state DMRG calculation. Using these, we then derived CISD and DMRG natural-orbital-based active spaces by diagonalizing the one-particle density matrices. We denote the n-electron n-orbital active space as (ne, no). We then solved within the active space using ground-state DMRG with bond dimension $M = 1200$ and then dynamic DMRG with bond dimension $M = 800$ [26, 27]. To understand the accuracy of this active-space DMRG solver, we also solved the full 40-orbital SIAM problem using DMRG/DDMRG with the same bond dimensions.

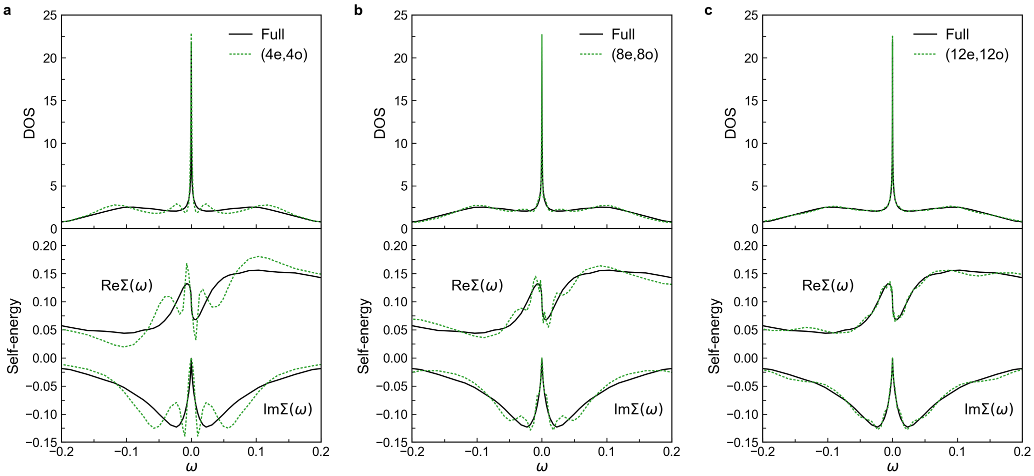

Figure 2.4: Impurity density of states and self-energy in the single-impurity Anderson model calculated by full DMRG and active-space DMRG (in CISD natural orbital basis). $U = 0.2$. (a) (4e, 4o) active space. (b) (8e, 8o) active space. (c) (12e, 12o) active space.

We first present the impurity density of states (DOS) and self-energy at $U = 0.2$ in Fig. 2.4. It shows a sharp Kondo resonance peak and two broad Hubbard bands in the full DMRG calculation, which agrees quantitatively with previous NRG results [54]. Compared to the full (40e, 40o) DMRG results (Fig. 2.4a), the CISD (4e, 4o) active-space result shows multiple spurious oscillations in the DOS and self-energy. However, we point out that even with this very small CISD (4e, 4o) active space, the impurity solver correctly predicts the shape of the Kondo resonance around the Fermi level, which is also confirmed in the self-energy comparison around $\omega = 0$. We find that the accuracy improves rapidly when the CISD active space is increased from (4e, 4o) to (8e, 8o) and (12e, 12o). At the (12e, 12o) level, the DOS and self-energy from active-space DMRG are almost indistinguishable from the full DMRG results.

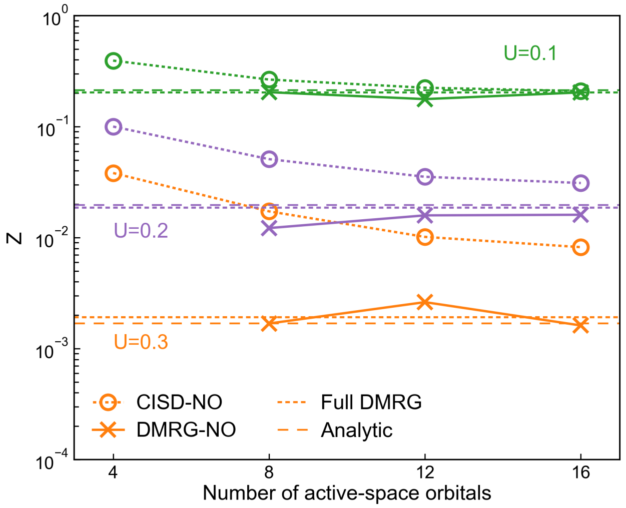

Figure 2.5: Quasiparticle renormalization weight Z for increasing sizes of active space in $U = 0.1, 0.2, 0.3$ SIAM models. The active spaces consist of CISD natural orbitals ("CISD-NO") or DMRG natural orbitals ("DMRG-NO"). The full (40e, 40o) DMRG calculated Z and analytic (exact) Z values are shown as horizontal dashed lines.

In Fig. 2.5, we further compare the quasiparticle renormalization factors Z defined as

$$Z = \left[1 - \frac{\partial\Sigma(\omega)}{\partial\omega}\bigg|_{\omega=0}\right]^{-1} \tag{2.13}$$

using the CISD and DMRG active spaces, denoted "CISD-NO" and "DMRG-NO," respectively. At moderate interaction strength ($U = 0.1$), the active-space DMRG predicts $Z = 0.21$ at the CISD (16e, 16o) level, in excellent agreement with full DMRG $Z = 0.20$ and the exact $Z = 0.21$ [1]. The exact Z is analytically calculated from Hewson's formula $Z = 4T_\mathrm{K}/\pi\Delta_0$ (with $\Delta_0 = 0.015$) and the T_K for large $\frac{U}{\Delta_0}$ [1]

$$T_\mathrm{K} = \sqrt{\frac{U\Delta_0}{2}}\exp\left(-\frac{\pi U}{8\Delta_0} + \frac{\pi\Delta_0}{2U}\right). \tag{2.14}$$

However, at stronger interaction strengths, the CISD active spaces become less accurate and overestimate Z. In contrast, the DMRG active spaces are more accurate, and even with the small (8e, 8o) active space, the computed Z values are reasonably close to the full DMRG and exact results: at $U = 0.2$ ($U = 0.3$), the active-space DMRG predicts $Z = 0.012$ ($Z = 0.0017$), while the full DMRG predicts $Z = 0.019$ ($Z = 0.0019$) and the exact result is $Z = 0.020$ ($Z = 0.0017$). With the DMRG (16e, 16o) active space, the computed Z values are almost indistinguishable from the exact results on the scale of Fig. 2.5. This confirms the effectiveness of an active-space strategy to reduce the number of orbitals needed to represent the properties of the impurity.

Table 2.1: Orbital occupancy cut-off thresholds for DMRG occupied and virtual natural orbitals to obtain active spaces of 6-16 orbitals in $U = 0.2$ SIAM model.

Active space size	Threshold (occupied)	Threshold (virtual)
6o	2×10^{-3}	2×10^{-3}
8o	4×10^{-4}	4×10^{-4}
10o	9×10^{-5}	8×10^{-5}
16o	2×10^{-6}	8×10^{-7}

Table 2.2: Orbital occupancy cut-off thresholds for occupied and virtual natural orbitals to obtain the largest active spaces used in dynamical and finite temperature calculations (around 28 orbitals) in *ab initio* calculations of various impurity elements.

Element	Threshold (occupied)	Threshold (virtual)
Ti	4×10^{-5}	4×10^{-4}
V	2×10^{-4}	7×10^{-4}
Cr	4×10^{-4}	3×10^{-3}
Mn	2×10^{-4}	4×10^{-3}
Fe	1×10^{-4}	4×10^{-3}
Co	1×10^{-4}	1×10^{-3}
Ni	2×10^{-5}	2×10^{-3}

We cannot rigorously infer the accuracy of the active-space DMRG in the *ab initio* Kondo simulations from the SIAM calculations because of the different Hamiltonian. However, we can assign a rough correspondence to the SIAM problem by dividing the number of active space orbitals used in the *ab initio* calculation by the number of effective singly occupied orbitals in the impurity atom, and using Z in the *ab initio* calculations to define a corresponding effective U. The most difficult systems are those with the lowest Kondo temperatures, namely Cr, Mn, and Fe, which have between 3-5 singly occupied orbitals. For Cr and Fe, the largest active space used in the computation of Z had 28 orbitals, thus we infer an effective SIAM active space size of 6-10 orbitals. Similar correspondence can be obtained by comparing the natural orbital cut-off thresholds used to obtain active spaces in the *ab initio* calculations and in the SIAM model (Tables 2.1 and 2.2). The cut-off thresholds in *ab initio* calculations are on the order of 10^{-4} or 10^{-3}, which are in the range of the thresholds of SIAM active spaces of 6-10 orbitals. The renormalization factors of Cr and Fe computed in the largest active space were 0.023 and 0.026, respectively. These Z values correspond roughly to $U = 0.2$, where with this effective (CISD) active space size in the SIAM problem we expect Z to be overestimated by ~ 3, which is similar to the observed overestimation of T_K with respect to the experimental estimates in the *ab initio* calculations. For Mn, where we could only use a 22-orbital active space (see below) and $Z \approx 0.006$, corresponding to $U > 0.2 \sim 0.3$, we expect Z to be overestimated by an order of magnitude. This also roughly agrees with the larger overestimation of T_K for Mn. The convergence of the SIAM calculations can thus be seen to be consistent with our *ab initio* results, and further provide an estimate of the required resources for more accurate *ab initio* calculations in the future.

Convergence of impurity observables towards parent basis limit

In this section, we present detailed benchmarks of the convergence of local impurity observables in the active-space DMRG calculations towards the parent basis limit. By diagonalizing the one-particle density matrix obtained from ground-state DMRG calculations within the (36e, 52o) active space ((36e, 46o) for Ni) in the def2-SVP basis, we further derived a series of smaller active spaces for performing the more time-consuming dynamical DMRG (DDMRG) calculations. The tested active spaces are listed in Table 2.3, where the corresponding orbital occupancies n and quasiparticle (QP) renormalization weights Z of impurity $3d$ orbitals are shown in Table 2.3 and Fig. 2.6. We find that, with the exception of Mn (where we could not converge the DDMRG calculation with respect to bond dimension for an active space larger than (22e, 22o)), Z and n are converged with small errors for all impurities at an active-space size of (22e, 22o) ((22e, 27o) for Co).

Table 2.3: Occupancies (n) and quasiparticle renormalization weights (Z) of impurity t_{2g} and e_g orbitals obtained from different DMRG/DDMRG active-space simulations. All results are in the def2-SVP basis unless specified.

Impurity	Active space	$n(t_{2g})$	$n(e_g)$	$Z(t_{2g})$	$Z(e_g)$
Ti	(10e, 10o)	0.59	0.26	0.64	0.59
	(18e, 18o)	0.60	0.30	0.59	0.62
	(22e, 22o)	0.60	0.32	0.58	0.58
	(30e, 29o)	0.61	0.30	0.60	0.59
	(36e, 52o)	0.62	0.32		
V	(10e, 10o)	0.99	0.19	0.27	0.45
	(18e, 18o)	0.93	0.37	0.20	0.47
	(22e, 22o)	0.93	0.39	0.19	0.37
	(28e, 30o)	0.93	0.38	0.19	0.37
	(36e, 52o)	0.95	0.41		
Cr	(10e, 10o)	0.91	0.82	0.12	0.12
	(14e, 16o)	1.10	0.61	0.092	0.16
	(22e, 22o)	0.97	0.94	0.017	0.038
	(28e, 28o)	0.99	0.93	0.023	0.047
	(36e, 52o)	0.99	0.96		
Mn	(10e, 10o)	1.06	1.07	0.045	0.011
	(16e, 16o)	1.16	1.00	0.068	0.018
	(22e, 22o)	1.17	1.03	0.071	0.0058
	(36e, 52o)	1.22	1.03		
Fe	(10e, 10o)	1.46	1.14	0.27	0.12
(def2-SVP)	(16e, 16o)	1.59	1.03	0.23	0.021
	(22e, 22o)	1.58	1.06	0.15	0.028
	(28e, 28o)	1.59	1.04	0.15	0.026
	(36e, 52o)	1.58	1.08		
Co	(10e, 10o)	1.85	1.16	0.29	0.11
	(16e, 16o)	1.90	1.09	0.37	0.060
	(22e, 27o)	1.80	1.26	0.19	0.11
	(26e, 36o)	1.79	1.28	0.20	0.11
	(36e, 52o)	1.77	1.32		
Ni	(10e, 10o)	1.77	1.77	0.50	0.47
	(16e, 16o)	1.74	1.85	0.48	0.47
	(22e, 22o)	1.80	1.80	0.42	0.40
	(28e, 28o)	1.78	1.81	0.40	0.38
	(36e, 46o)	1.80	1.82		
Fe	(26e, 29o)	1.54	1.08	0.19	0.039
(cc-pVTZ)	(46e, 76o)	1.56	1.08		

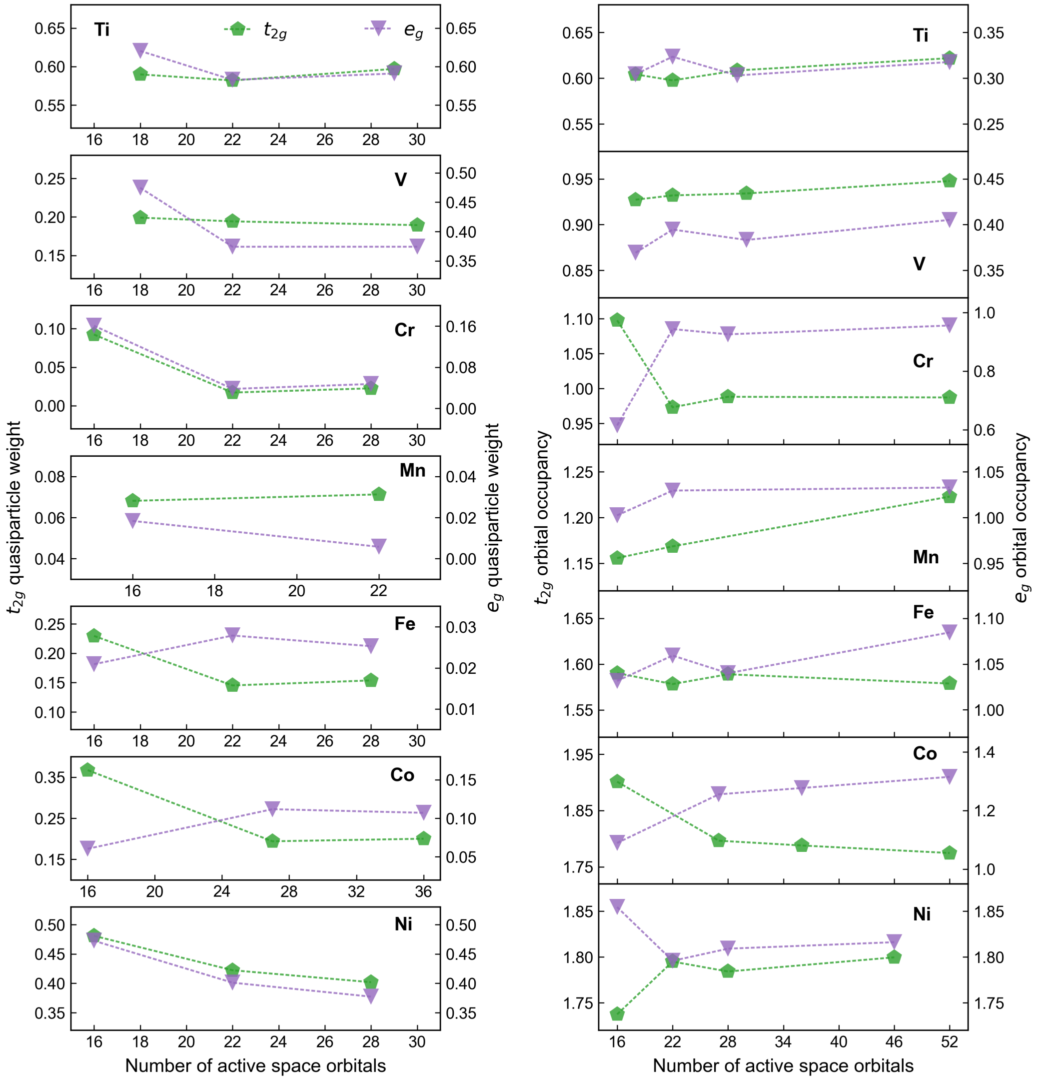

Figure 2.6: Convergence of the quasiparticle renormalization weights (left) and orbital occupancies (right) of the $3d$ orbitals of all impurities as the DMRG active space increases.

Many-body solver error estimates

We next present an estimate of the errors from two of the approximations in our calculations: active space size and DMRG bond dimension, which are the main many-body solver errors with respect to the exact parent-basis limit (in this case, def2-SVP). First, we analyze the errors in the predicted impurity observables due to the use of active spaces. As shown in Table 2.4, for orbital occupancies, we estimate the remaining errors relative to the parent-basis limit by comparing the largest and second largest ground-state (GS) active-space calculations (assuming (36e, 52o) is a sufficiently large active space). For example, for Fe, we obtain $\Delta n(t_{2g}) = 0.010$ and $\Delta n(e_g) = 0.045$ by comparing the 52o (largest GS) and 28o (second largest GS) results. Using the maximum Δn across all impurities (except Mn), we estimate that the active space associated orbital occupancy error to be at most 0.045. For estimating the QP weight errors, we adopt a two-step procedure: (1) Compare the largest and second largest Green's function (GF) active-space calculations. For Fe, we obtain $\Delta Z(t_{2g}) = 0.009$ and $\Delta n(e_g) = 0.002$ by taking the difference between the 28o (largest GF) and 22o (second largest GF) results. (2) Estimate the QP weight errors between the largest and second largest GS active spaces by assuming a linear relationship between Δn and ΔZ:

$$\begin{aligned}\Delta Z(\text{largest GS vs. 2nd largest GS}) = &\frac{\Delta n(\text{largest GS vs. 2nd largest GS})}{\Delta n(\text{largest GF vs. 2nd largest GF})} \\ &\times \Delta Z(\text{largest GF vs. 2nd largest GF}). \end{aligned} \tag{2.15}$$

Following this procedure, we estimate the Z errors for Fe to be $\Delta Z(t_{2g}) = 0.008$ and $\Delta n(e_g) = 0.005$. Furthermore, using the maximum ΔZ across all impurities (except Mn), we estimate the active space associated QP weight error to be at most 0.048.

We then analyze the numerical errors due to finite bond dimension in DMRG calculations. We find that the DMRG predicted orbital occupancies are very well converged with respect to the bond dimension (M) in all impurities. For example, for Cr, the orbital occupancy differences between $M = 3000$ and $M = 4000$ calculations are negligibly small: $\Delta n(t_{2g}) = 2 \times 10^{-4}$ and $\Delta n(e_g) = 1 \times 10^{-4}$.

We then focus on the DMRG bond dimension associated QP weight errors. In Table 2.5, we present DDMRG Z values and discarded weights at various bond dimensions for V, Cr, Fe, and Co, in their largest GF active-space calculations. We also performed a two-point linear extrapolation against the discarded weights to estimate the Z values at infinite DDMRG bond dimension. By comparing the largest

Table 2.4: Active-space error analysis of orbital occupancies (n) and quasiparticle renormalization weights (Z) of impurity $3d$ impurity orbitals. The "est." values are estimated according to Eq. 2.15.

Impurity	Comparison btw. active spaces	$\Delta n(t_{2g})$	$\Delta n(e_g)$	$\Delta Z(t_{2g})$	$\Delta Z(e_g)$
Ti	22o vs. 29o	0.011	0.020	0.015	0.008
	29o vs. 52o	0.013	0.015	0.018 (est.)	0.006 (est.)
V	22o vs. 30o	0.002	0.011	0.007	0.001
	30o vs. 52o	0.014	0.022	0.048 (est.)	0.001 (est.)
Cr	22o vs. 28o	0.015	0.018	0.005	0.010
	28o vs. 52o	0.001	0.030	0.000 (est.)	0.016 (est.)
Fe	22o vs. 28o	0.011	0.019	0.009	0.002
	28o vs. 52o	0.010	0.045	0.008 (est.)	0.005 (est.)
Co	22o vs. 36o	0.009	0.022	0.006	0.005
	36o vs. 52o	0.013	0.038	0.010 (est.)	0.008 (est.)
Ni	22o vs. 28o	0.011	0.013	0.020	0.024
	28o vs. 46o	0.015	0.007	0.029 (est.)	0.013 (est.)

M results against the extrapolated values, we find that the largest bond dimension associated Z error is around 5×10^{-3} (Cr), an order of magnitude smaller than the largest active space associated Z error.

In summary, combining the maximum errors from the active space and bond dimension error analysis, we conservatively estimate that our predicted n values are converged to at least ~ 0.04 and Z values are converged to at least ~ 0.05 compared to the exact parent basis result.

DFT hybridization functions

We present DFT-calculated real-axis hybridization functions of magnetic impurity atoms in bulk Cu in Fig. 2.7. It is observed that the t_{2g} hybridization has a greater magnitude than the e_g hybridization in all impurities, especially in the range of [3, 6] eV. Meanwhile, we find that the magnitudes of both t_{2g} and e_g hybridization functions become smaller from Ti to Ni.

Table 2.5: Error analysis of quasiparticle renormalization weights of impurity $3d$ orbitals against DDMRG maximum bond dimensions and discarded weights. The "extrap." values are obtained through two-point linear extrapolation against discarded weights.

Impurity	Max. bond dimension	Max. discarded weight	$Z(t_{2g})$	$Z(e_g)$
V (28e, 30o)	2500	1.52×10^{-2}	0.1893	0.3742
	4000	9.41×10^{-3}	0.1867	0.3736
	extrap.	0	0.1825	0.3726
	$\lvert Z(M = 4000) - Z(\text{extrap.}) \rvert$		4.2×10^{-3}	1.0×10^{-3}
Cr (28e, 28o)	2500	2.24×10^{-2}	0.0202	0.0473
	3500	1.47×10^{-2}	0.0226	0.0474
	extrap.	0	0.0273	0.0476
	$\lvert Z(M = 3500) - Z(\text{extrap.}) \rvert$		4.7×10^{-3}	1.9×10^{-4}
Fe (28e, 28o)	2500	5.28×10^{-3}	0.1538	0.0253
	3500	2.97×10^{-3}	0.1538	0.0255
	extrap.	0	0.1539	0.0258
	$\lvert Z(M = 3500) - Z(\text{extrap.}) \rvert$		7.3×10^{-5}	2.9×10^{-4}
Co (26e, 36o)	1500	3.46×10^{-2}	0.2011	0.1088
	2500	1.29×10^{-3}	0.2003	0.1071
	extrap.	0	0.1999	0.1062
	$\lvert Z(M = 2500) - Z(\text{extrap.}) \rvert$		4.5×10^{-4}	9.9×10^{-4}

Self-energies of magnetic impurity orbitals

We show real-axis self-energies of Cr, Mn, and Fe impurities in bulk Cu calculated by all-orbital simulations in Fig. 2.8. When ω approaches the Fermi level, the imaginary part of the self-energies of the $3d$ orbitals approaches zero, while the real part of the self-energies of the $3d$ orbitals changes linearly with respect to the frequency, which agrees with the expected Fermi liquid behavior.

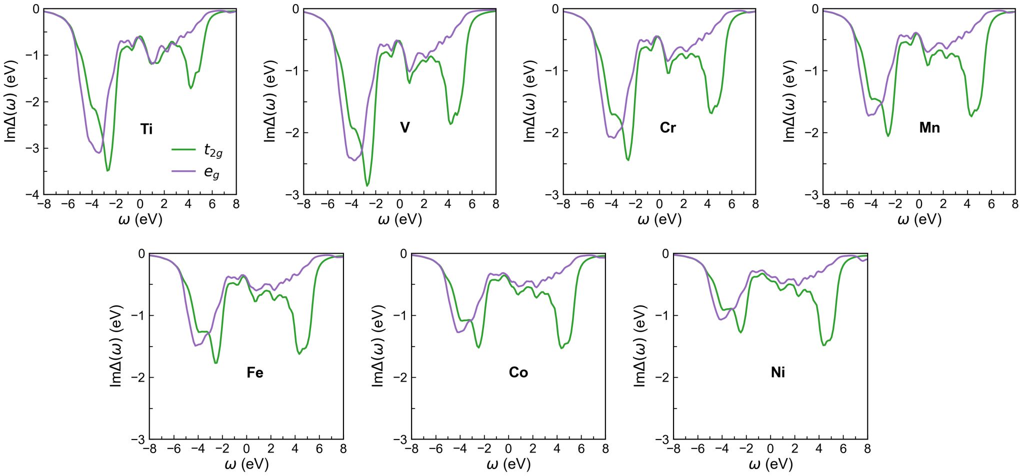

Figure 2.7: Real-axis hybridization function of $3d$ orbitals of magnetic impurities in bulk Cu calculated by DFT with the PBE functional.

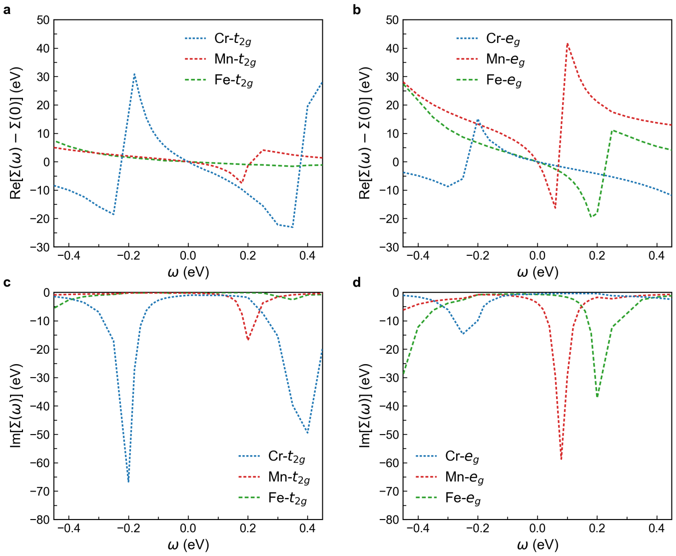

Figure 2.8: Real-axis self-energies of Cr, Mn, and Fe impurities from all-orbital calculations. (a) Real part of the self-energy matrix elements diagonal in the orbital indices associated with the t_{2g} orbitals. (b) Real part of the self-energy matrix elements diagonal in the orbital indices associated with the e_g orbitals. (c) Imaginary part of self-energies of t_{2g} orbitals. (d) Imaginary part of self-energies of e_g orbitals.

Density of state of magnetic impurity orbitals

We present the local DOS of the $3d$ orbitals of the Co impurity in bulk Cu calculated by all-orbital simulations in Fig. 2.9, in addition to the DOS of Cr, Mn and Fe impurities in Figure 2. Compared to results from the 5-orbital model calculations in Ref. [15], the all-orbital DOS exhibits qualitatively similar resonance and shoulder

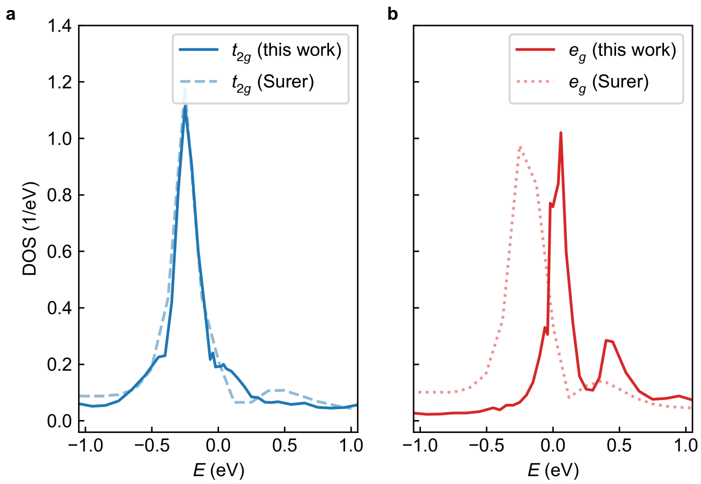

Figure 2.9: (a) t_{2g} and (b) e_g resolved DOS of Co impurity in bulk Cu from all-orbital calculations (“this work”), compared to DOS taken from Ref. [15] (“Surer”).

peaks near the Fermi level. Quantitatively, resonance peaks near the Fermi level from all-orbital calculations are narrower, especially for the e_g orbitals. The narrower widths are consistent with the smaller quasiparticle renormalization weights Z = 0.19 (t_{2g}) and 0.11 (e_g) from our all-orbital calculation compared to the Z = 0.42 (t_{2g}) and 0.47 (e_g) from Ref. [15].

Summary of ground-state and spectral properties

The ground-state and spectral properties of magnetic impurities calculated by all-orbital simulations are summarized in Table 2.6 and Table 2.7. In Table 2.7, we include the natural orbital occupancies of t_{2g} and e_g symmetry derived from the (36e, 52o) active-space DMRG density matrix. We choose to show the most fractional occupancies with $n_{\text{nat}} > 1$. We observe that the natural occupancies in Table 2.7 correlate well with the quasiparticle renormalization Z in Table 2.6, i.e., more fractionally occupied orbitals are found to possess stronger quasiparticle renormalization.

Spin and charge fluctuations in Kondo impurities

The spin fluctuation in all magnetic impurities can be better understood by calculating the spin-spin correlation within the 3d shell

$$S_{ij} = \langle \hat{S}_i \hat{S}_j \rangle - \langle \hat{S}_i \rangle \langle \hat{S}_j \rangle. \tag{2.16}$$

Table 2.6: Hybridization function values at the Fermi level $\Delta(0)$, quasiparticle renormalization weights Z, and Kondo temperatures T_K of magnetic impurities in bulk Cu computed by all-orbital simulations. All results are in the def2-SVP basis with Green's function active space of (22e, 22o) ((22e, 27o) for Co).

Impurity	$\Delta(0, t_{2g})$ (eV)	$\Delta(0, e_g)$ (eV)	$Z(t_{2g})$	$Z(e_g)$	$T_K(t_{2g})$ (K)	$T_K(e_g)$ (K)
Ti	−0.59	−0.64	0.58	0.58	3144	3412
V	−0.52	−0.56	0.19	0.37	924	1895
Cr	−0.47	−0.48	0.017	0.038	73	167
Mn	−0.44	−0.43	0.071	0.0058	287	23
Fe	−0.43	−0.40	0.15	0.028	565	101
Co	−0.43	−0.38	0.19	0.11	761	396
Ni	−0.44	−0.38	0.42	0.40	1709	1374

Table 2.7: Orbital occupancies n, natural orbital occupancies n_{nat}, and spin moments S of magnetic impurities in bulk Cu computed by all-orbital simulations. All results are in the def2-SVP basis with ground-state active space of (36e, 52o) ((36e, 46o) for Ni).

Impurity	$n(t_{2g})$	$n(e_g)$	$n_{\text{nat}}(t_{2g})$	$n_{\text{nat}}(e_g)$	$n(3\text{d})$	S
Ti	0.62	0.32	1.84	1.93	2.50	0.93
V	0.95	0.40	1.57	1.86	3.65	1.36
Cr	0.99	0.96	1.24	1.21	4.87	2.23
Mn	1.22	1.03	1.46	1.20	5.73	1.98
Fe	1.58	1.09	1.64	1.29	6.92	1.42
Co	1.77	1.31	1.76	1.52	7.94	0.95
Ni	1.80	1.82	1.89	1.89	9.03	0.48

As shown in Fig. 2.10a, Cr has the strongest intra- and inter-orbital spin correlation among all impurities. From Cr to Co, the intra-orbital spin correlation in t_{2g} orbitals is largely suppressed, while the intra- and inter-orbital spin correlation within the e_g orbitals stays strong or moderate, which is consistent with the orbital-dependent trend in quasiparticle renormalization. Fig. 2.10a also reveals that, in the Mn, Fe, and Co systems, the inter-orbital spin correlations have the following relation: $S_{i\neq j}(t_{2g}\text{-}t_{2g}) < S_{i\neq j}(t_{2g}\text{-}e_g) < S_{i\neq j}(e_g\text{-}e_g)$. We also include the impurity charge fluctuation in Fig. 2.10b, which is calculated as $C_{ij} = \langle \hat{n}_i \hat{n}_j \rangle - \langle \hat{n}_i \rangle \langle \hat{n}_j \rangle$.

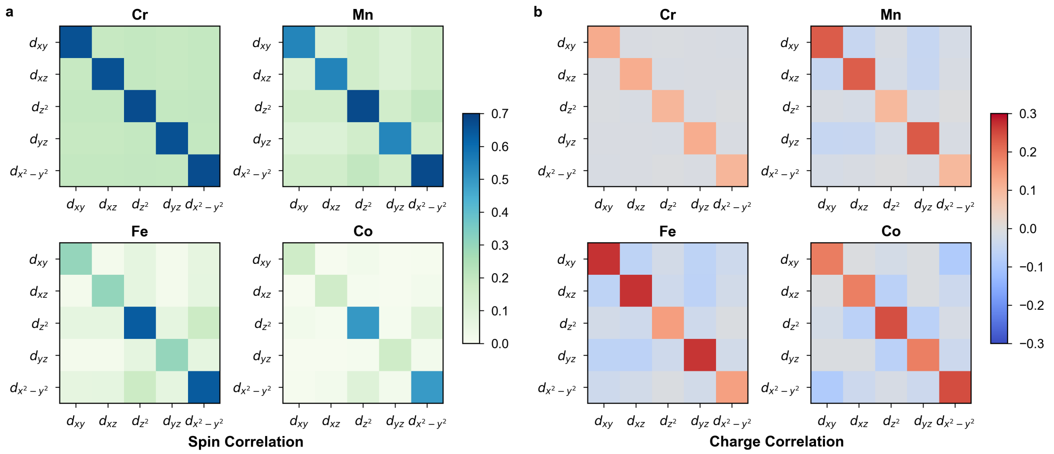

Figure 2.10: Orbital-resolved (a) spin and (b) charge correlations for Cr, Mn, Fe, and Co impurities.

Effective $3d$-model calculations

To compare our all-orbital simulations against downfolded effective model calculations, we derived a multi-orbital Anderson impurity model with Hamiltonian

$$\begin{aligned} H = {} & \sum_{ij\sigma} \tilde{F}_{ij} f^{\dagger}_{i\sigma} f_{j\sigma} + \frac{1}{2} \sum_{ijkl} \sum_{\sigma\sigma'} U_{ijkl} f^{\dagger}_{i\sigma} f^{\dagger}_{j\sigma'} f_{l\sigma'} f_{k\sigma} \\ & + \sum_{k\sigma} \epsilon_k c^{\dagger}_{k\sigma} c_{k\sigma} + \sum_{ki\sigma} V_{ik} (f^{\dagger}_{i\sigma} c_{k\sigma} + c^{\dagger}_{k\sigma} f_{i\sigma}), \end{aligned} \tag{2.17}$$

where the indices i, j, k, l run over five $3d$ orbitals and U_{ijkl} is the screened Coulomb interaction tensor within the $3d$ shell. In practice, approximations such as the density-density approximation are often employed for the Coulomb interaction tensor. Here, we adopted a Kanamori Hamiltonian [18] that goes beyond the density-density approximation, where the Coulomb tensor (second term in Eq. 2.17) is written as

$$\begin{aligned} H_K = {} & \sum_{i} U_{iiii} \hat{n}_{i\uparrow} \hat{n}_{i\downarrow} + \sum_{i \neq j} \sum_{\sigma\sigma'} (U_{ijij} - U_{ijji} \delta_{\sigma\sigma'}) \hat{n}_{i\sigma} \hat{n}_{j\sigma'} \\ & + \sum_{i \neq j} U_{ijji} (f^{\dagger}_{i\uparrow} f^{\dagger}_{j\downarrow} f_{i\downarrow} f_{j\uparrow} - f^{\dagger}_{i\uparrow} f^{\dagger}_{i\downarrow} f_{j\uparrow} f_{j\downarrow}). \end{aligned} \tag{2.18}$$

We give the Coulomb integrals for $3d$ electrons in the basis of cubic harmonics, where U_{iiii}, U_{ijij}, and U_{ijji} are expressed using parameters U_0, J_1, J_2, J_3, J_4. The readers are referred to Ref. [18] for the detailed parametrization. The U_0, J_1, J_2, J_3, J_4

parameters can be expressed in terms of Slater integrals F^0, F^2, and F^4:

$$U_0 = F^0 + \frac{8}{7}\frac{1}{14}(F^2 + F^4), \tag{2.19}$$

$$J_1 = \frac{1}{49}(3F^2 + \frac{20}{9}F^4), \tag{2.20}$$

$$J_2 = -2\frac{5}{7}\frac{1}{14}(F^2 + F^4) + 3J_1, \tag{2.21}$$

$$J_3 = 6\frac{5}{7}\frac{1}{14}(F^2 + F^4) - 5J_1, \tag{2.22}$$

$$J_4 = 4\frac{5}{7}\frac{1}{14}(F^2 + F^4) - 3J_1. \tag{2.23}$$

The Slater integrals F^0, F^2, and F^4 are obtained from two parameters U and J, where $U = F_0$ and $J = \frac{1}{14}(F^2 + F^4)$ with a constant ratio $F^2/F^4 = 0.625$. In summary, the Kanamori Hamiltonian in Eq. 2.18 is fully characterized by two parameters U and J. In Kondo simulation literature, U and J are usually treated as adjustable parameters. Here, we took the U and J values of magnetic impurities from cRPA calculations in Ref. [50], which are listed in Table 2.8.

Table 2.8: Coulomb interaction parameters in Kanamori Hamiltonian taken from Ref. [50].

Parameter (eV)	Ti	V	Cr	Mn	Fe	Co	Ni
U	3.1	3.2	4.4	4.4	3.8	4.3	3.8
J	0.5	0.6	0.7	0.7	0.7	0.8	0.8

Table 2.9: Quasiparticle renormalization weights Z and Kondo temperatures T_K of magnetic impurities in bulk Cu from five-orbital model Hamiltonian calculations.

Impurity	$Z(t_{2g})$	$Z(e_g)$	$T_\mathrm{K}(t_{2g})$ (K)	$T_\mathrm{K}(e_g)$ (K)
Ti	0.92	0.95	4953	5556
V	0.63	0.87	2993	4431
Cr	0.31	0.55	1318	2445
Mn	0.11	0.062	449	243
Fe	0.45	0.11	1769	398
Co	0.71	0.72	2800	2524
Ni	0.99	0.99	3999	3383

The one-particle Hamiltonian in Eq. 2.17 was treated in a similar fashion as in the all-orbital calculations, where we adopted the Hartree-Fock effective Hamiltonian for five $3d$ orbitals so that the double-counting term can be exactly removed. The $3d$

Table 2.10: Orbital occupancies n and natural orbital occupancies n_{nat} of magnetic impurities in bulk Cu from five-orbital model Hamiltonian calculations.

Impurity	$n(t_{2g})$	$n(e_g)$	$n_{\text{nat}}(t_{2g})$	$n_{\text{nat}}(e_g)$	$n(3\text{d})$
Ti	0.32	0.13	1.98	1.94	1.23
V	0.75	0.15	1.86	1.89	2.54
Cr	1.23	0.27	1.63	1.85	4.23
Mn	1.26	0.84	1.59	1.50	5.45
Fe	1.60	1.07	1.84	1.52	6.95
Co	1.68	1.74	1.93	1.80	8.51
Ni	1.94	1.97	1.91	1.88	9.76

Table 2.11: Five-orbital model Hamiltonian results after fitting the chemical potential. Shown in the table are the changes in the chemical potential $\Delta\mu$, orbital occupancies n, quasiparticle renormalization weights Z, and Kondo temperature T_{K}.

Impurity	$\Delta\mu$ (eV)	$n(t_{2g})$	$n(e_g)$	$n(3\text{d})$	$Z(t_{2g})$	$Z(e_g)$	$T_{\text{K}}(t_{2g})$ (K)	$T_{\text{K}}(e_g)$ (K)
Ti	4.0	0.73	0.13	2.45	0.77	1.00	4171	5870
V	3.7	1.12	0.15	3.66	0.67	0.79	3183	4003
Cr	2.7	1.44	0.27	4.87	0.62	0.37	2649	1627
Mn	1.1	1.40	0.76	5.72	0.35	0.22	1411	864
Fe	−0.1	1.60	1.06	6.93	0.40	0.087	1547	315
Co	−1.9	1.56	1.62	7.93	0.47	0.78	1833	2719
Ni	−4.4	1.80	1.82	9.03	0.98	0.97	3963	3314

block of the DFT hybridization function was discretized on the same non-uniform grid to obtain the bath parameters ϵ_k and V_{ik}, which resulted in 49 bath orbitals per $3d$ impurity orbital.

To solve the embedding problem consisting of 5 impurity orbitals and 245 bath orbitals, we employed the same active-space DMRG solver. A Hartree-Fock calculation with fixed chemical potential at the DFT level was first performed, followed by a CISD calculation on the full embedding problem. A (40e, 40o) natural-orbital active space was derived by diagonalizing the CISD density matrix. We then conducted ground-state DMRG calculations with bond dimension $M = 3500$ on the (40e, 40o) active space and further derived a (20e, 20o) DMRG natural-orbital active space. Finally, a dynamical DMRG calculation was done on the (20e, 20o) active space with bond dimension $M = 1200$, and DMRG self-energies were used to estimate the quasiparticle renormalizations and Kondo temperatures in magnetic impurities.

We summarize the Green's function results obtained using the same chemical potential as in the all-orbital calculations in Table 2.9 and the ground-state properties in Table 2.10. We find that the natural occupancies in the downfolded model calculations are less close to singly occupied than in the all-orbital calculations. In the meantime, the quasiparticle renormalization weights and the predicted Kondo temperatures are much higher in the model calculations compared to the all-orbital simulations. We also observe that the total $3d$ occupancies in the model differ from those in the all-orbital calculation by up to 1.27 electrons. Because the $3d$ occupancy can significantly impact the correlation strength and the Kondo temperature [56], for a fair comparison with the all-orbital calculations, we also performed the model calculation with chemical potentials μ fitted such that the total $3d$ occupancies match those in the all-orbital calculations in Table 2.7. The model results with the fitted μ are shown in Table 2.11. The Kondo temperatures calculated using the new quasiparticle renormalization weight decrease slightly for a few elements (e.g., Fe and Co) compared to without the chemical potential fitting, but there is no consistent improvement in the absolute T_K or its trends. With or without fitting the chemical potential in the low-energy model calculations, our all-orbital results are an order of magnitude better.

Specific heat calculation on the Anderson impurity model

We benchmark the accuracy of a specific heat calculation on the symmetric single-impurity Anderson model (SIAM) (see 2.8 for an introduction) within the numerical framework of this work. In the symmetric SIAM, for large $\frac{U}{\Delta_0}$, T_K can be calculated analytically as a function of the impurity on-site Coulomb interaction U and the hybridization strength Δ_0, $T_\mathrm{K} = \sqrt{\frac{U\Delta_0}{2}} \exp\left(-\frac{\pi U}{8\Delta_0} + \frac{\pi\Delta_0}{2U}\right)$ [1]. Additionally, the specific heat has been solved exactly through Bethe Ansatz and computed numerically [57, 58]. This allows us to analyze the errors due to the bath discretization and active space truncation on the peak temperature of the specific heat and also verify the nature of the excitations that give rise to the Kondo singlet breaking (see 2.8).

To compute the finite temperature properties, we solve for the excited states of the SIAM in the canonical ensemble using the ground-state DMRG solver with SU(2) symmetry and a level-shifted Hamiltonian for the n^{th} eigenstate

$$\hat{H}'_n = \hat{H} + \sum_{i=1}^{n-1} c_i |\Psi_i\rangle\langle\Psi_i| \tag{2.24}$$

where $\hat{H}$ is the original DMRG Hamiltonian, c_i is the energy shift multiplier, and $|\Psi_i\rangle$ is the i^{th} converged eigenstate to be projected out [27, 59, 60]. We used $c_i = 5D$ for all i and a DMRG bond dimension of $M = 1200$. With this bond dimension, DMRG converged to a small discarded weight of less than 5×10^{-9}.

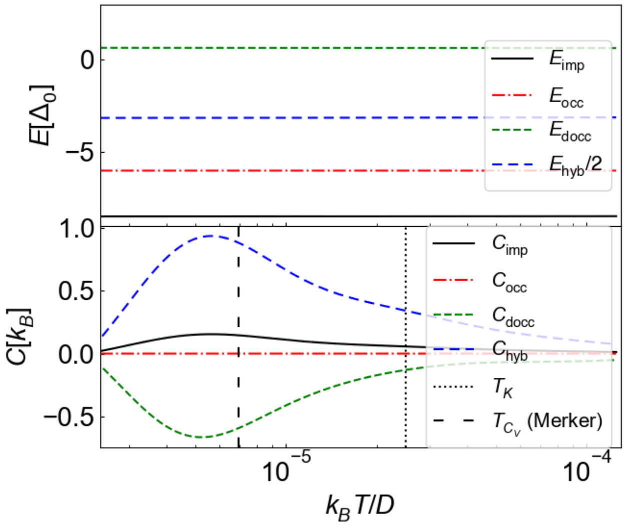

Figure 2.11: Benchmark of finite temperature results from the DMRG solver on the SIAM with $U = 0.012D$ and $\Delta_0 = 0.001D$, using the logarithmic discretization with base $b = 4$ and the procedure to extract impurity specific heat as outlined in Ref. [61]. Different components of the energy and specific heat are defined the same as in Fig. 4 of Ref. [61]. The exact T_{K} (vertical black dotted line) and specific heat peak temperature from numerical renormalization group results in Ref. [61] (vertical black dashed line, "Merker") are included as references.

We benchmarked on the SIAM with the same parameters as in Ref. [61], $U = 0.012D$ and a flat-band hybridization $\text{Im}\Delta(\omega + i0^+) = -\Delta_0,\ |\omega| < D$ where $\Delta_0 = 0.001D$. For convenience, we set $D = 1$. We used the same logarithmic discretization, consistent with the rest of the manuscript, but with 19 orbitals and logarithmic intervals defined using a larger log base $b = 4$ as used in Ref. [61] to achieve a small spacing near the Fermi level. Using the procedure to extract the impurity specific heat contribution as outlined in Ref. [61], we obtained a peak in the impurity specific heat at 0.22 T_{K} (Fig. 2.11), in good agreement with the peak in Ref. [61] at around 0.28 T_{K}.

In Fig. 2.12 we show the estimated specific heat peak temperatures $T_{C_{\text{V}}}$ as a function of the (DMRG natural orbital) active space size. We see that the position of the peak varies by about a factor of 3 as a function of the active space size (and thus the estimated Kondo temperature also varies by about a factor of 3). This is different from the behaviour of the estimated Kondo temperatures from the Hewson formula, as shown in 2.8, which are already reasonably converged with an active space size of 8 orbitals. Since the location of the C_V peak depends on different excitations (in particular the neutral excitations) than those that enter into the self-energy and Z, it is unsurprising that there are different finite size effects. These numerical results support the use of T_K from the Hewson formula as our primary estimate in the main text.

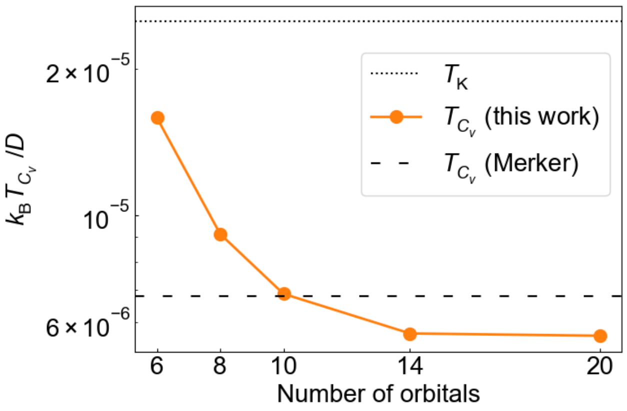

Figure 2.12: Specific heat peak temperature (T_{C_V}) of SIAM with $U = 0.012D$ and $\Delta_0 = 0.001D$, using active spaces of different numbers of orbitals taken out of the full space of 20 orbitals, the logarithmic discretization with base $b = 4$ and the procedure to extract the impurity specific heat as outlined in Ref. [61]. The exact T_K (black dotted line) and specific heat peak temperature from numerical renormalization group results in Ref. [61] (black dashed line) are shown as references.

From the excited states, we can also examine the nature of the excitations that give rise to the peak in the heat capacity. To verify the spin-flip nature of the lowest energy excitations, we compute the impurity spin-flip weight $w_{ii}^2 = |\langle \Psi_{S=0}|c_{i\beta}^\dagger c_{i\alpha}|\Psi_{S=1}\rangle|^2$ where i indexes the impurity orbital (here, the $S_z = 1$ state of the $|\Psi_{S=1}\rangle$ multiplet is used as an example). This quantity satisfies $w_{ii}^2 \leq 1$ and is equal to 1/2 for a pure localized impurity spin flip. We show the weights for the lowest excited states, with their corresponding energies, in Table 2.12.

Ab initio impurity specific heat

We calculated the finite-temperature and excited state properties in the all-electron simulations within different active spaces, using the procedure outlined in 2.8. We used a grand canonical formalism and extracted the canonical C_V using the relations in Ref. [62]. The chemical potential was chosen to ensure that the average electron number of the impurity and bath at T_K (estimated from Hewson's formula Eq. 2.3)

Table 2.12: Impurity spin-flip weight w_{ii}^2, its normalized value $w_{ii}^2/\sum_{pq} w_{pq}^2$, and the excitation energies E/D of the lowest singlet-triplet excitations that give rise to the specific heat peak, calculated in active spaces of different number of orbitals (N_{orb}).

N_{orb}	threshold (occupied)	threshold (virtual)	w_{ii}^2	$w_{ii}^2/\sum_{pq} w_{pq}^2$	E/D
20	0	0	0.071	0.123	1.2×10^{-5}
14	1×10^{-7}	1×10^{-7}	0.073	0.105	1.2×10^{-5}
10	3×10^{-5}	3×10^{-5}	0.087	0.138	1.5×10^{-5}
8	2×10^{-4}	2×10^{-4}	0.101	0.169	2.0×10^{-5}
6	2×10^{-3}	2×10^{-3}	0.121	0.210	3.4×10^{-5}

matched the electron number of the ground state. The excited states were obtained in a DMRG active space of up to (26e, 36o) size with maximum DMRG bond dimension $M = 4000$, converging to a discarded weight of less than 5×10^{-5}. In this way, 449, 129, 83, 44, 42, 38, and 80 excited states in total were calculated for the Ti, V, Cr, Mn, Fe, Co, and Ni impurities, respectively.

In the SIAM, the impurity contribution to the specific heat was obtained by partitioning the energy between the impurity and the bath, as described in Ref. [61]. However, in the case of the ab initio model, the partitioning is ambiguous. This is in part because energy partitioning is always non-unique (as the only constraint is that the parts sum up to the same whole), but also because as we converge to the basis limit of the all-electron basis, the additional impurity orbitals necessarily extend beyond the impurity atom into the bulk (see discussion in main text). We found that this either made the estimated C_{V} sensitive to various choices, or gave unphysical results (e.g., the impurity specific heat capacity could be negative).

Consequently, to produce a (rough) estimate of T_{K}, similar to the analysis of the excitation character of the excited states in 2.8, we quantified the degree of "impurity" character of each excited state and only included those above a given threshold when computing the impurity specific heat. Concretely, for the $S_z = 1$ component of a triplet excited state, we computed

$$w_{ij} = \langle \Psi_0 | c_{i\alpha}^{\dagger} c_{j\beta} | \Psi_1 \rangle \tag{2.25}$$

where $c_{i\alpha}^{\dagger}, c_{j\beta}$ are creation and annihilation operators on orbitals that are localized on the impurity or on the bath, respectively (these orbitals were obtained by a rotation of the active space). Then, the impurity character is defined as

$$\lambda = \frac{\sum_{i\notin \text{bath or} j\notin \text{bath}} w_{ij}^2}{\sum_{ij} w_{ij}^2}. \tag{2.26}$$

A similar analysis was carried out for the quintet excited states. Using a threshold of $\lambda > 0.12$, we show the estimated T_{C_V} from the impurity specific heat peak in Fig. 2.13. In the SIAM, the peak of the specific heat is always below T_K. We see that this is true in our calculations for Ti and V, but not for the other impurity elements, suggesting that T_{C_V} is overestimated in the other cases. Given the strong finite size effects observed in specific heat capacity calculations in general (as studied in the SIAM in 2.8), we consider the estimation of T_K from the Hewson formula to be better converged. However, this rough treatment indicates that similar trends can be reproduced through the heat capacity (see Fig. 2.14).

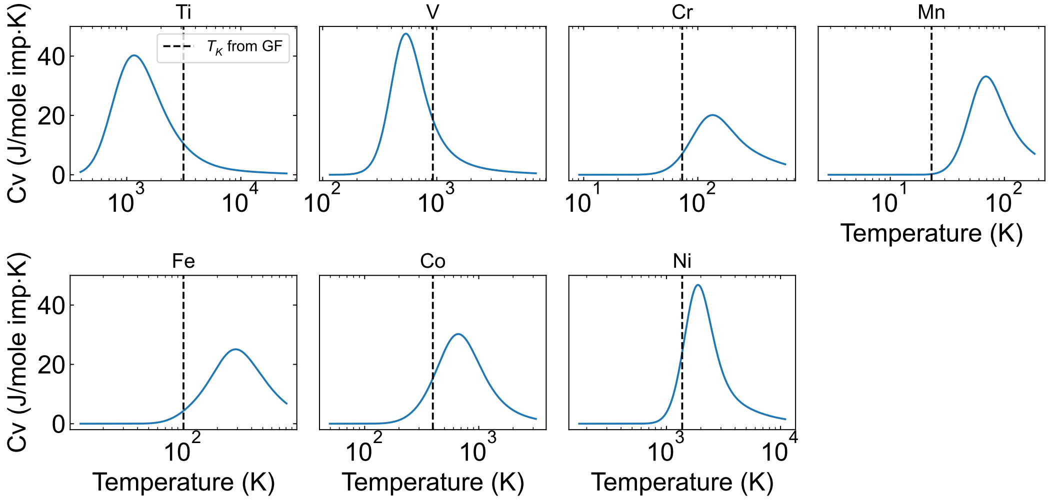

Figure 2.13: Impurity specific heat per mole of magnetic impurities in bulk Cu from ab initio all-orbital calculations. The Kondo temperatures predicted using Herson's formula with the quasiparticle renormalization weights from the Green's function calculations ("T_K from GF") are shown for comparison.

Ab initio and model excited state analysis

To illustrate the difference in the excited states in the ab initio all electron treatment and in the model calculations, we performed excited state model calculations for Mn in the (20e, 20o) active space with the same chemical potential as in the all-orbital calculations, and compared those to the excited states seen in the ab initio

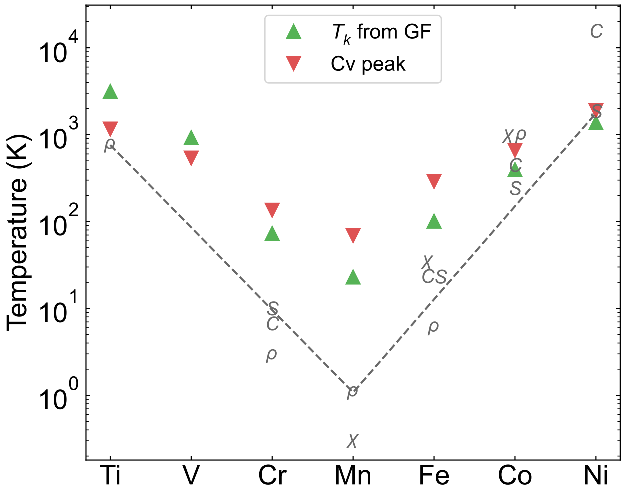

Figure 2.14: The temperatures corresponding to the peak in the impurity specific heat compared to the Kondo temperatures predicted by Hewson's formula from ab initio all-orbital calculations and those measured in experiments.

calculations. As shown in Fig. 2.15, in both the model and *ab initio* all-orbital calculations, we observed multiple near-degenerate low-energy triplets that involve partial transfer of an electron from t_{2g} to e_g and to the bath orbitals, accompanied by a spin-flip (orange), as well as one low-energy triplet that corresponds to a simultaneous on-site spin-flip of all fractionally occupied d orbitals (purple). The latter corresponds to the low-energy excitation of a large spin Kondo model. However, in the model calculations, the charge transfer triplets are higher in energy than the Kondo model triplet, which is opposite to the all-orbital calculations where the charge-transfer triplets are the lowest triplets. As discussed in the main text, correctly capturing the charge-transfer triplet excitations appears to be critical to reproducing the quantitative Kondo trends, which highlights again the power of the all-orbital calculations.

Fig. 2.16 further shows the ab initio transition density matrix between the groundstate and the low-energy triplet state which is dominated by a pure intra-impurity spin-flip for all the elements, corresponding to the excitation in the multi-orbital Kondo model. For Ti and V, the singlet-triplet excitation is dominated by the t_{2g} intraorbital excitations, while for Fe and Co it is dominated by the e_g intraorbital excitations. The excitations in Cr and Mn have significant contributions from both t_{2g} and e_g orbitals.

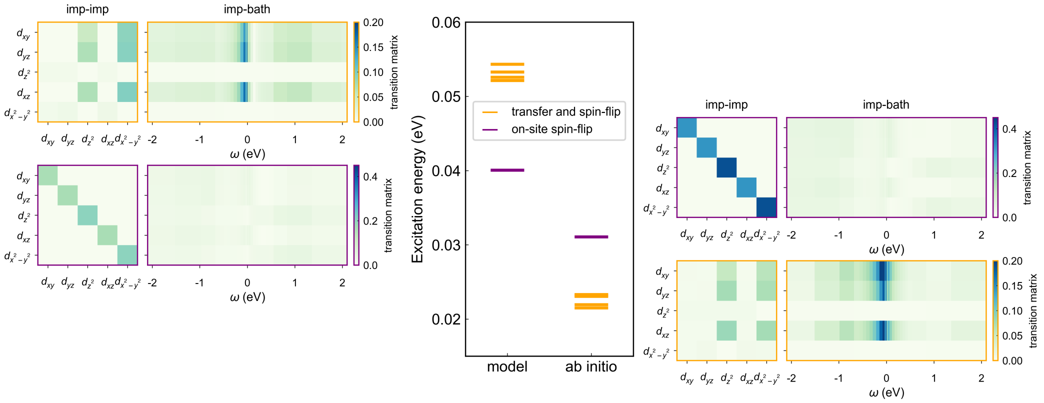

Figure 2.15: The excitation energies of triplets associated with on-site spin-flip (purple) from the ground state and of triplets associated with charge transfer between different orbitals and spin-flip (orange) from the ground state for the Mn impurity. The impurity-impurity and impurity-bath blocks of spin-flip transition density matrices $|\langle\Psi_{S=0}|c^{\dagger}_{i\downarrow}c_{j\uparrow}|\Psi_{S=1,S_z=1}\rangle|$ from the ground state (vertical axis) to the triplet(s) (horizontal axis) from model calculations and *ab initio* all-orbital calculations are shown on the left and right, respectively, to illustrate the on-site spin-flip (purple) and the charge transfer and spin-flip (orange) process. The bath orbitals are ordered based on their bath energies ω. The transition density matrices of charge-transfer triplets are summed over all near-degenerate states.

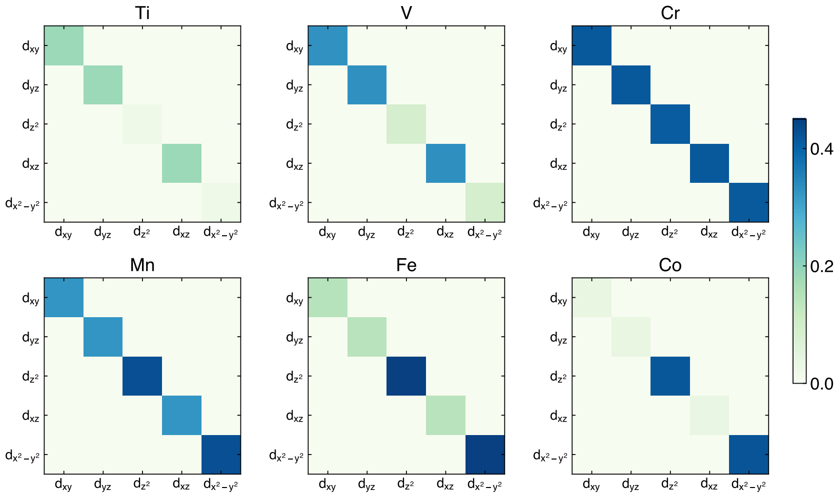

Figure 2.16: Orbital resolved spin-flip transition density matrix $|\langle\Psi_{S=0}|c^{\dagger}_{i\downarrow}c_{j\uparrow}|\Psi_{S=1,S_z=1}\rangle|$ between the ground state and the lowest triplet excited state that is dominated by intra-impurity orbital excitations, across the series of impurities from Ti to Co.

Computational time

	Ground state (36e, 52o)		**Green's function** (22e, 22o)		C_V **(28e, 28o)**	
Impurity	wall time (h)	core hours	wall time (h)	core hours	wall time (h)	core hours
Ti	27	2556	60	5776	1019	119784
V	55	7984	94	18057	733	95274
Cr	64	9215	99	18959	645	50843
Mn	100	14395	105	20088	489	49726
Fe	82	11853	135	25848	237	15174
Co	78	11225	298	71534	171	21884
Ni	49	9407	66	12753	50	3179

Table 2.13: Computational time of various tasks: ground state DMRG calculations in the largest active space (36e, 52o); Green's function calculations with DDMRG at 7 frequency points near the Fermi level in active spaces of around (22e, 22o) ((22e, 27o) for Co); and specific heat (C_V) calculations where we calculated ground and excited eigenstates in spin manifolds of up to $S = 8$ in the canonical ensemble in active spaces of around (28e, 28o) ((30e, 29o) for Ti, (28e, 30o) for V, (26e, 36o) for Co). The ground state and Green's function calculations were performed on 2–8 nodes with 24 cores per node, while the specific heat calculations in each spin manifold were performed on 1–8 nodes with 64 cores per node.

Kondo temperature in multi-orbital impurities

The exponential decrease in the Kondo temperature with the spin S of the impurity [34] has previously been discussed using a mechanism involving Hund's coupling [63]. We briefly summarize the literature arguments here.

As a simple example, consider an Anderson model with $l = 2$ conduction electrons scattering off an impurity with a half-filled d-shell,

$$H = \sum_{\boldsymbol{k}m\sigma} \epsilon_{\boldsymbol{k}} n_{\boldsymbol{k}m\sigma} + \sum_{\boldsymbol{k}m\sigma} V_{\boldsymbol{k}m} \left(c^{\dagger}_{\boldsymbol{k}\sigma} f_{m\sigma} + f^{\dagger}_{m\sigma} c_{\boldsymbol{k}\sigma} \right) + H_{\text{imp}}, \tag{2.27}$$

where H_{imp} includes the interaction on impurity sites and m, σ are the labels of the atomic orbital and spin separately.

In the presence of strong on-site electron repulsion and Hund's coupling, we can focus solely on the spin degree of freedom of the impurity. The spin configuration of the impurity is constrained to $S = 5/2$. Using the Schrieffer-Wolff transformation [63, 64], the effective Hamiltonian is reduced to the following form:

$$H = \sum_{\boldsymbol{k}m\sigma} \epsilon_{\boldsymbol{k}} n_{\boldsymbol{k}m\sigma} + \sum_{\boldsymbol{k}\boldsymbol{k}'m} J_{m\boldsymbol{k}\boldsymbol{k}'} \boldsymbol{S} \cdot c^{\dagger}_{\boldsymbol{k}'m} \frac{\boldsymbol{\sigma}}{2} c_{\boldsymbol{k}m}. \tag{2.28}$$

The orbital angular momentum of the scattering conduction electrons is conserved. Because the impurity is half-filled, conduction electrons cannot exchange orbital angular momentum with the impurity. The exchange interaction $J_{m\boldsymbol{k}\boldsymbol{k}'}$ is second order in the hybridization term:

$$J_{m\boldsymbol{k}\boldsymbol{k}'} = \frac{V_{\boldsymbol{k}m}V_{\boldsymbol{k}'m}}{2S}\left(\frac{1}{E_+} + \frac{1}{E_-}\right), \tag{2.29}$$

where E_+ and E_- represent the additional energy of the virtual process involving the addition or removal of an electron. The factor of $2S$ in the denominator arises from the representation of the $S = 5/2$ spin operator in terms of five $S = 1/2$ impurity electron operators.

For an impurity without a half-filled d-shell, the effective Hamiltonian includes both orbital and spin exchange. However, if we focus only on the spin degree of freedom and assume that all singly occupied states are spin-up, with the remaining states either doubly occupied or empty, the spin dependence of $J_{m\boldsymbol{k}\boldsymbol{k}'}$ can be generalized, where spin corresponds to the spin of the singly occupied orbitals [63]. Although simplistic, this formula provides a rationalization for the trend of the Kondo temperature T_{K} of transition metal impurities within host alloys [4, 34] with

$$T_{\mathrm{K}} \sim \exp(-1/J^{\mathrm{eff}}\rho). \tag{2.30}$$

Here, J^{eff} is inversely proportional to the spin S as in Eq. 2.29, and consequently, the Kondo temperature is predicted to exhibit an exponential dependence on S.

Another way to estimate the Kondo temperature is through the bandwidth of the Kondo resonance (Abrikosov-Suhl resonance), $\tilde{\Delta}$, at the Fermi level, with

$$T_k = \frac{\pi}{4}\tilde{\Delta}. \tag{2.31}$$

If there is no quantum phase transition between the non-interacting limit and the finite-interaction case, the low-energy behavior of the interacting system can be described by a local Fermi liquid theory [65]. The bandwidth $\tilde{\Delta}$ in the interacting case is related to the non-interacting hybridization width Δ through the quasiparticle renormalization weight Z :

$$\tilde{\Delta} = Z\Delta. \tag{2.32}$$

The entire effect of the interaction is encapsulated in Z. If the renormalization weight Z can be estimated non-perturbatively, this formula can be applied to address the finite interaction case, which is the basis of the Hewson estimate of the Kondo temperature used in the main text.

References

1. Hewson, A. C. *The Kondo Problem to Heavy Fermions* ISBN: 9780521363822. doi:`10.1017/CBO9780511470752` (Cambridge University Press, 1993).
2. Kondo, J. Resistance minimum in dilute magnetic alloys. *Progress of Theoretical Physics* **32,** 37–49. doi:`10.1143/ptp.32.37` (1964).
3. Knorr, N., Schneider, M. A., Diekhöner, L., Wahl, P. & Kern, K. Kondo effect of single Co adatoms on Cu surfaces. *Physical Review Letters* **88,** 096804. doi:`10.1103/PhysRevLett.88.096804` (2002).
4. Nevidomskyy, A. H. & Coleman, P. Kondo resonance narrowing in d- and f-electron systems. *Physical Review Letters* **103,** 147205. doi:`10.1103/PhysRevLett.103.147205` (2009).
5. Prüser, H., Wenderoth, M., Dargel, P. E., Weismann, A., Peters, R., Pruschke, T. & Ulbrich, R. G. Long-range Kondo signature of a single magnetic impurity. *Nature Physics* **7,** 203–206. doi:`10.1038/nphys1876` (2011).
6. Kouwenhoven, L. & Glazman, L. Revival of the Kondo effect. *Physics World* **14,** 33–38. doi:`10.1088/2058-7058/14/1/28` (2001).
7. Lucignano, P., Mazzarello, R., Smogunov, A., Fabrizio, M. & Tosatti, E. Kondo conductance in an atomic nanocontact from first principles. *Nature Materials* **8,** 563–567. doi:`10.1038/nmat2476` (2009).
8. Anderson, P. W. Localized magnetic states in metals. *Physical Review* **124,** 41. doi:`10.1103/PhysRev.124.41` (1961).
9. Wilson, K. G. The renormalization group: Critical phenomena and the Kondo problem. *Reviews of Modern Physics* **47,** 773. doi:`10.1103/RevModPhys.47.773` (1975).
10. Karp, J., Hampel, A. & Millis, A. J. Dependence of DFT+DMFT results on the construction of the correlated orbitals. *Physical Review B* **103,** 195101. doi:`10.1103/PhysRevB.103.195101` (2021).
11. Aryasetiawan, F., Imada, M., Georges, A., Kotliar, G., Biermann, S. & Lichtenstein, A. I. Frequency-dependent local interactions and low-energy effective models from electronic structure calculations. *Physical Review B* **70,** 195104. doi:`10.1103/PhysRevB.70.195104` (2004).
12. Wang, X., Han, M. J., de'Medici, L., Park, H., Marianetti, C. A. & Millis, A. J. Covalency, double-counting, and the metal-insulator phase diagram in transition metal oxides. *Physical Review B* **86,** 195136. doi:`10.1103/PhysRevB.86.195136` (2012).
13. Muechler, L., Badrtdinov, D. I., Hampel, A., Cano, J., Rösner, M. & Dreyer, C. E. Quantum embedding methods for correlated excited states of point defects: Case studies and challenges. *Physical Review B* **105,** 235104. doi:`10.1103/PhysRevB.105.235104` (2022).

14. Jacob, D., Haule, K. & Kotliar, G. Kondo effect and conductance of nanocontacts with magnetic impurities. *Physical Review Letters* **103,** 016803. doi:`10.1103/PhysRevLett.103.016803` (2009).

15. Surer, B., Troyer, M., Werner, P., Wehling, T. O., Läuchli, A. M., Wilhelm, A. & Lichtenstein, A. I. Multiorbital Kondo physics of Co in Cu hosts. *Physical Review B* **85,** 85114. doi:`10.1103/PhysRevB.85.085114` (2012).

16. Gardonio, S., Karolak, M., Wehling, T. O., Petaccia, L., Lizzit, S., Goldoni, A., Lichtenstein, A. I. & Carbone, C. Excitation spectra of transition-metal atoms on the Ag (100) surface controlled by Hund's exchange. *Physical Review Letters* **110,** 186404. doi:`10.1103/PhysRevLett.110.186404` (2013).

17. Dang, H. T., Dos Santos Dias, M., Liebsch, A. & Lounis, S. Strong correlation effects in theoretical STM studies of magnetic adatoms. *Physical Review B* **93,** 115123. doi:`10.1103/PhysRevB.93.115123` (2016).

18. Valli, A., Bahlke, M. P., Kowalski, A., Karolak, M., Herrmann, C. & Sangiovanni, G. Kondo screening in Co adatoms with full Coulomb interaction. *Physical Review Research* **2,** 33432. doi:`10.1103/PhysRevResearch.2.033432` (2020).

19. Zhu, T., Cui, Z.-H. & Chan, G. K.-L. Efficient formulation of ab initio quantum embedding in periodic systems: Dynamical mean-field theory. *Journal of Chemical Theory and Computation* **16,** 141–153. doi:`10.1021/acs.jctc.9b00934` (2020).

20. Cui, Z.-H., Zhu, T. & Chan, G. K.-L. Efficient implementation of ab initio quantum embedding in periodic systems: Density matrix embedding theory. *Journal of Chemical Theory and Computation* **16,** 119–129. doi:`10.1021/acs.jctc.9b00933` (2020).

21. Zhu, T. & Chan, G. K.-L. Ab initio full cell GW+DMFT for correlated materials. *Physical Review X* **11,** 021006. doi:`10.1103/PhysRevX.11.021006` (2021).

22. Cui, Z. H., Zhai, H., Zhang, X. & Chan, G. K.-L. Systematic electronic structure in the cuprate parent state from quantum many-body simulations. *Science* **377,** 1192–1198. doi:`10.1126/science.abm2295` (2022).

23. Cui, Z.-H., Yang, J., Tölle, J., Ye, H.-Z., Yuan, S., Zhai, H., Park, G., Kim, R., Zhang, X., Lin, L., *et al.* Ab initio quantum many-body description of superconducting trends in the cuprates. *Nature Communications* **16,** 1845. doi:`10.1038/s41467-025-56883-x` (2025).

24. Larsson, H. R., Zhai, H., Umrigar, C. J. & Chan, G. K.-L. The chromium dimer: closing a chapter of quantum chemistry. *Journal of the American Chemical Society* **144,** 15932–15937. doi:`10.1021/jacs.2c06357` (2022).

25. Yang, J., Hu, W., Usvyat, D., Matthews, D., Schütz, M. & Chan, G. K.-L. Ab initio determination of the crystalline benzene lattice energy to sub-kilojoule/mole accuracy. *Science* **345,** 640–643. doi:`10.1126/science.1254419` (2014).

26. Zhai, H. & Chan, G. K.-L. Low communication high performance ab initio density matrix renormalization group algorithms. *Journal of Chemical Physics* **154,** 224116. doi:`10.1063/5.0050902` (2021).

27. Zhai, H., Larsson, H. R., Lee, S., Cui, Z. H., Zhu, T., Sun, C., Peng, L., Peng, R., Liao, K., Tölle, J., Yang, J., Li, S. & Chan, G. K. L. Block2: A comprehensive open source framework to develop and apply state-of-the-art DMRG algorithms in electronic structure and beyond. *Journal of Chemical Physics* **159,** 234801. doi:`10.1063/5.0180424/2930207` (2023).

28. Weigend, F. & Ahlrichs, R. Balanced basis sets of split valence, triple zeta valence and quadruple zeta valence quality for H to Rn: Design and assessment of accuracy. *Physical Chemistry Chemical Physics* **7,** 3297–3305. doi:`10.1039/b508541a` (2005).

29. Balabanov, N. B. & Peterson, K. A. Systematically convergent basis sets for transition metals. I. All-electron correlation consistent basis sets for the 3d elements Sc-Zn. *Journal of Chemical Physics* **123,** 64107. doi:`10.1063/1.1998907/932754` (2005).

30. Perdew, J. P., Burke, K. & Ernzerhof, M. Generalized gradient approximation made simple. *Physical Review Letters* **77,** 3865. doi:`10.1103/PhysRevLett.77.3865` (1996).

31. Sun, Q., Zhang, X., Banerjee, S., Bao, P., Barbry, M., Blunt, N. S., Bogdanov, N. A., Booth, G. H., Chen, J., Cui, Z. H., Eriksen, J. J., Gao, Y., Guo, S., Hermann, J., Hermes, M. R., Koh, K., Koval, P., Lehtola, S., Li, Z., Liu, J., Mardirossian, N., McClain, J. D., Motta, M., Mussard, B., Pham, H. Q., Pulkin, A., Purwanto, W., Robinson, P. J., Ronca, E., Sayfutyarova, E. R., Scheurer, M., Schurkus, H. F., Smith, J. E., Sun, C., Sun, S. N., Upadhyay, S., Wagner, L. K., Wang, X., White, A., Whitfield, J. D., Williamson, M. J., Wouters, S., Yang, J., Yu, J. M., Zhu, T., Berkelbach, T. C., Sharma, S., Sokolov, A. Y. & Chan, G. K. L. Recent developments in the PySCF program package. *Journal of Chemical Physics* **153,** 024109. doi:`10.1063/5.0006074` (2020).

32. Knizia, G. Intrinsic atomic orbitals: An unbiased bridge between quantum theory and chemical concepts. *Journal of Chemical Theory and Computation* **9,** 4834–4843. doi:`10.1021/ct400687b` (2013).

33. De Vega, I., Schollwöck, U. & Wolf, F. A. How to discretize a quantum bath for real-time evolution. *Physical Review B* **92,** 155126. doi:`10.1103/PhysRevB.92.155126` (2015).

34. Daybell, M. D. & Steyert, W. A. Localized magnetic impurity states in metals: Some experimental relationships. *Reviews of Modern Physics* **40,** 380–389. doi:`10.1103/RevModPhys.40.380` (1968).

35. Zgid, D., Gull, E. & Chan, G. K.-L. Truncated configuration interaction expansions as solvers for correlated quantum impurity models and dynamical mean-field theory. *Physical Review B* **86,** 165128. doi:`10.1103/PhysRevB.86.165128` (2012).

36. Chan, G. K. L. & Sharma, S. The density matrix renormalization group in quantum chemistry. *Annual Review of Physical Chemistry* **62,** 465–481. doi:`10.1146/annurev-physchem-032210-103338` (2011).

37. Ronca, E., Li, Z., Jimenez-Hoyos, C. A. & Chan, G. K. L. Time-step targeting time-dependent and dynamical density matrix renormalization group algorithms with ab initio hamiltonians. *Journal of Chemical Theory and Computation* **13,** 5560–5571. doi:`10.1021/acs.jctc.7b00682` (2017).

38. Tsvelick, A. & Wiegmann, P. Exact results in the theory of magnetic alloys. *Org. Chem. Advances in Physical Organic Chemistry* **32,** 453–713. doi:`10.1080/00018738300101581` (1983).

39. Nakamura, K., Arita, R. & Imada, M. Ab initio derivation of low-energy model for iron-based superconductors LaFeAsO and LaFePO. *Journal of the Physical Society of Japan* **77,** 93711. doi:`10.1143/JPSJ.77.093711` (2008).

40. Helgaker, T., Klopper, W., Koch, H. & Noga, J. Basis-set convergence of correlated calculations on water. *Journal of Chemical Physics* **106,** 9639–9646 (1997).

41. Hewson, A. C. Renormalized perturbation expansions and Fermi liquid theory. *Physical Review Letters* **70,** 4007–4010. doi:`10.1103/PhysRevLett.70.4007` (1993).

42. Daybell, M. & Steyert, W. Observation of Nagaoka's bound state for conduction electrons in dilute magnetic alloys. *Physical Review Letters* **18,** 398. doi:`10.1103/PhysRevLett.18.398` (1967).

43. Okada, I. & Yosida, K. Singlet ground state of the localized d-electrons coupled with conduction electrons in metals. *Progress of Theoretical Physics* **49,** 1483–1502. doi:`10.1143/PTP.49.1483` (1973).

44. Georges, A., De Medici, L. & Mravlje, J. Strong correlations from hund's coupling. *Annual Review of Condensed Matter Physics* **4,** 137–178. doi:`10.1146/annurev-conmatphys-020911-125045` (2013).

45. Joly, L., Kappler, J. P., Ohresser, P., Sainctavit, P., Henry, Y., Gautier, F., Schmerber, G., Kim, D. J., Goyhenex, C., Bulou, H., Bengone, O., Kavich, J., Gambardella, P. & Scheurer, F. Kondo screening of the spin and orbital magnetic moments of Fe impurities in Cu. *Physical Review B* **95,** 41108. doi:`10.1103/PhysRevB.95.041108` (2017).

46. Haen, P., Souletie, J. & Teixeira, J. The resistivity of Cu and CuMn and CuCr alloys: Kondo effect and deviations from Matthiessen's rule. *Journal of Low Temperature Physics* **23,** 191–224. doi:`10.1007/BF00117251` (1976).

47. Sacramento, P. D. & Schlottmann, P. Thermodynamic properties of dilute CuCr alloys. *Physical Review B* **42,** 743–746. doi:`10.1103/PhysRevB.42.743` (1990).

48. Anderson, P. W. & Hasegawa, H. Considerations on double exchange. *Physical Review* **100,** 675. doi:`10.1103/PhysRev.100.675` (1955).

49. Kanamori, J. Electron correlation and ferromagnetism of transition metals. *Progress of Theoretical Physics* **30,** 275–289. doi:`10.1143/ptp.30.275` (1963).

50. Şaşioğlu, E., Friedrich, C. & Blügel, S. Effective Coulomb interaction in transition metals from constrained random-phase approximation. *Physical Review B* **83,** 121101–121102. doi:`10.1103/PhysRevB.83.121101` (2011).

51. Kresse, G. & Furthmüller, J. Efficient iterative schemes for ab initio total-energy calculations using a plane-wave basis set. *Physical Review B* **54,** 11169. doi:`10.1103/PhysRevB.54.11169` (1996).

52. Kresse, G. & Joubert, D. From ultrasoft pseudopotentials to the projector augmented-wave method. *Physical Review B* **59,** 1758. doi:`10.1103/PhysRevB.59.1758` (1999).

53. Zhu, T., Jiménez-Hoyos, C. A., McClain, J., Berkelbach, T. C. & Chan, G. K.-L. Coupled-cluster impurity solvers for dynamical mean-field theory. *Physical Review B* **100,** 115154. doi:`10.1103/PhysRevB.100.115154` (2019).

54. Bulla, R., Hewson, A. C. & Pruschke, T. Numerical renormalization group calculations for the self-energy of the impurity Anderson model. *Journal of Physics: Condensed Matter* **10,** 8365–8380. doi:`10.1088/0953-8984/10/37/021` (1998).

55. Nishimoto, S. & Jeckelmann, E. Density-matrix renormalization group approach to quantum impurity problems. *Journal of Physics: Condensed Matter* **16,** 613–625. doi:`10.1088/0953-8984/16/4/010` (2004).

56. Jacob, D. Towards a full ab initio theory of strong electronic correlations in nanoscale devices. *Journal of Physics: Condensed Matter* **27,** 245606. doi:`10.1088/0953-8984/27/24/245606` (2015).

57. Wiegmann, P. & Tsvelick, A. Exact solution of the Anderson model: I. *Journal of Physics C: Solid State Physics* **16,** 2281. doi:`10.1088/0022-3719/16/12/017` (1983).

58. Okiji, A. & Kawakami, N. Thermodynamic properties of the Anderson model. *Physical Review Letters* **50,** 1157. doi:`10.1103/PhysRevLett.50.1157` (1983).

59. Wouters, S., Poelmans, W., Ayers, P. W. & Van Neck, D. CheMPS2: A free open-source spin-adapted implementation of the density matrix renormalization group for ab initio quantum chemistry. *Computer Physics Communications* **185,** 1501–1514. doi:`10.1016/j.cpc.2014.01.019` (2014).

60. Fishman, M., White, S. & Stoudenmire, E. M. The ITensor software library for tensor network calculations. *SciPost Physics Codebases,* 004. doi:`10.21468/SciPostPhysCodeb.4` (2022).

61. Merker, L. & Costi, T. Numerical renormalization group calculation of impurity internal energy and specific heat of quantum impurity models. *Physical Review B* **86,** 075150. doi:`10.1103/PhysRevB.86.075150` (2012).

62. Ströker, P. & Meier, K. Classical statistical mechanics in the grand canonical ensemble. *Physical Review E* **104,** 014117. doi:`10.1103/PhysRevE.104.014117` (2021).

63. Schrieffer, J. R. The Kondo effect—The link between magnetic and nonmagnetic impurities in metals? *Journal of Applied Physics* **38,** 1143–1150. doi:`10.1063/1.1709517` (1967).

64. Schrieffer, J. R. & Wolff, P. A. Relation between the Anderson and Kondo Hamiltonians. *Physical Review* **149,** 491–492. doi:`10.1103/PhysRev.149.491` (2 1966).

65. Nozieres, P. A "Fermi-liquid" description of the Kondo problem at low temperatures. *Journal of Low Temperature Physics* **17,** 31–42. doi:`10.1007/BF00654541` (1974).

Chapter 3

ACCURATE CRYSTAL FIELD HAMILTONIANS OF SINGLE-ION MAGNETS AT MEAN-FIELD COST

This chapter is based on the following publication:

1. **Peng, L**, Liu, S., Zhang, X., Chen, X., Li, C., Cheng, H.-P. & Chan, G. K.-L. Accurate crystal field Hamiltonians of single-ion magnets at mean-field cost. *arXiv preprint arXiv:2505.16905*. doi:`10.48550/arXiv.2505.16905` (2025).

3.1 Abstract

The effective crystal field Hamiltonian provides the key description of the electronic properties of single-ion magnets, but obtaining its parameters from ab initio computation is challenging. We introduce a simple approach to derive the effective crystal field Hamiltonian through density functional calculations of randomly rotated mean-field states within the low-energy manifold. In benchmarks on five lanthanide-based complexes, we find that we compute with mean-field cost an effective crystal field Hamiltonian that matches the state-of-the-art from much more expensive multi-configurational quantum chemistry methods. In addition, we are able to reproduce the experimental low-energy spectrum and magnetic properties with an accuracy exceeding prior attempts. Due to its low cost, our approach provides a crucial ingredient in the computational design of single-ion magnets with tailored physical properties and low-energy spectra.

3.2 Introduction

Tuning the electronic properties of single-ion molecular complexes is a goal of synthetic chemistry for potential applications in areas of molecular magnetism [1, 2], molecular spintronics [3, 4], and in quantum information processing [5–7]. In these systems, the effective crystal field Hamiltonian $\hat{H}_{\text{CF}}$ provides the theoretical rationalization of the low-energy properties, such as the excited states and electronic pathways for decoherence. For lanthanide complexes in particular, to which we will devote our attention in this work, $\hat{H}_{\text{CF}}$ describes the interplay between the strong spin-orbit coupling and associated zero-field splitting in the f-orbital shell and the crystal field, leading to a large number of effective parameters that need to be determined, especially in low-symmetry complexes. This complicates both experimental and theoretical procedures to accurately estimate $\hat{H}_{\mathrm{CF}}$ in lanthanide complexes.

From a theory perspective, state-of-the-art procedures aim to determine multiple electronic eigenstates of the lanthanide complex which are subsequently fitted to the crystal field Hamiltonian [8–10]. However, the character of these eigenstates involving the partially filled $4f$-shell often requires a sophisticated multi-configurational wavefunction description. Quantitative results can be obtained using the complete active space self-consistent field method (CASSCF) [11–13] augmented by second-order perturbation theory such as complete active space perturbation theory (CASPT2) [14, 15] or n-electron valence state perturbation theory (NEVPT2) [16, 17], or by multi-reference configuration interaction [18–20], but these are prohibitively expensive for many of the lanthanide-based single-ion complexes of experimental interest.

In this work, we introduce a method to calculate the effective crystal field Hamiltonian for lanthanide-based single-ion complexes with an accuracy comparable to the state-of-the-art multireference theories, but at the cost of (several) mean-field Kohn-Sham density functional theory calculations. The basic insight is that although representing the eigenstates of $\hat{H}_{\mathrm{CF}}$ might require a multireference treatment, obtaining the parameters of $\hat{H}_{\mathrm{CF}}$ may not, and in particular by considering a sufficient number of single-reference states Ψ_i (which need not be eigenstates) and their energies E_i, we can deduce the corresponding parameters of $\hat{H}_{\mathrm{CF}}$. Similar techniques are used to derive effective Hamiltonians in other contexts, for example exchange parameters in spin Hamiltonians, which are often derived from the energies of broken symmetry spin states [21], and in the context of ligand field theory, the ligand field Hamiltonian has been derived in a similar procedure involving Slater determinants with both ground- and excited-occupancies [22]. Here, we choose as our Ψ_i single-configurational states that are optimized to (approximately) lie within the lowest spin-orbit coupled $|JM\rangle$ manifold using a variant of constrained density functional theory (cDFT) [23–27] and we deduce the effective couplings of the crystal field Hamiltonian from their energies. We therefore refer to this as deriving the constrained DFT ab initio crystal field Hamiltonian.

Our method captures both the dynamical and static effects of electron correlation on the crystal field Hamiltonian and, as we shall show below, achieves accuracy on par with state-of-the-art CASPT2- or NEVPT2- methods in small systems. However, as it has the same low computational scaling as density functional theory, it enables the derivation of the crystal field Hamiltonian in large molecules. As an example of the latter, we demonstrate our method on the holmium double–decker complex which has 113 atoms, achieving an accuracy surpassing that of CASSCF and NEVPT2 in predicting both the energy spectrum and the magnetic properties.

3.3 Constrained DFT ab initio crystal field Hamiltonian

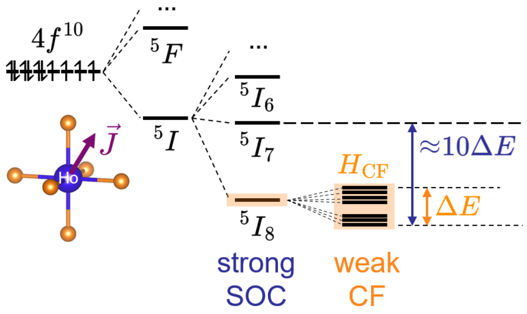

Figure 3.1: An illustration of the origin of the zero-field energy splitting (orange) in a Ho-based single-ion complex. Energy levels are not drawn to scale.

We will be interested in single-ion complexes where there is a strong spin-orbit coupling. At the two-component level of treating relativistic effects, this means that the electronic Hamiltonian $\hat{H}$ contains a spin-orbit operator and the eigenstates are no longer eigenfunctions of spin. In addition to the spin-orbit coupling, which splits the non-relativistic atomic degeneracies, there is also the crystal field of the ligands. Fig. 3.1 illustrates the structure of the low-energy manifold and the range of splittings for a typical lanthanide complex.

The effective crystal field Hamiltonian is an operator in the space of the lowest manifold of states (the right of Fig. 3.1)

$$\hat{H}_{\rm CF} = \sum_{JMJ'M'} h_{JM,J'M'} |JM\rangle\langle J'M'|. \tag{3.1}$$

Assuming that these derive from a multiplet manifold from a single J (which is the case when the SOC is stronger than the crystal field splitting) the above effective Hamiltonian can also be written in terms of operators within this $|JM\rangle$ manifold, known as extended Stevens operator equivalents [28]

$$\hat{H}_{\rm CF}(J) = \sum_{k=2,4,6} \sum_{q=-k}^{k} B_k^q \hat{O}_k^q(J) \tag{3.2}$$

where we use the definitions of $\hat{O}_k^q(J)$ in terms of $|JM\rangle\langle JM'|$ following the convention in Ref. [29–32], and the coefficients B_k^q are the molecular-specific parameters to be determined.

Given a set of electronic low-energy states $\{\Psi_i\}$ within the manifold on which $\hat{H}_{\mathrm{CF}}$ acts, we can determine the coefficients of $\hat{H}_{\mathrm{CF}}$ from

$$\begin{aligned}
E_i &= \text{const} + \langle \Psi_i \,|\, \hat{H}_{\mathrm{CF}}(J) \,|\, \Psi_i \rangle, \; i = 1 \ldots D' \\
\Psi_i &= \sum_{JM} C_{JM,i} \Psi_i^{JM} \\
E_i &= \text{const} + \sum_{JMJM'} C^*_{JM,i} C_{JM',i} h_{JM,JM'}
\end{aligned} \tag{3.3}$$

where const is an energy zero, and the above constitutes a set of linear equations for the coefficients of $\hat{H}_{\mathrm{CF}}$ (if $D' = D$ where D is the number of symmetry-allowed nonzero B_k^q to be determined, generically we expect a unique solution; for $D' > D$, the linear equations can be solved in the least squares sense). The key to an efficient procedure is to use states $\{\Psi_i\}$ for which the energy E_i can be easily computed. Note that Ψ_i need not be an eigenstate of the electronic Hamiltonian. Instead, we can choose $\{\Psi_i\}$ to be low-energy single-configurational states in the manifold of interest, whose energies can be accurately approximated by affordable electronic structure methods, such as density functional approximations.

For example, we can consider the case where $\hat{H}_{\mathrm{CF}}$ acts on a single $\{|JM\rangle\}$ manifold where J is the maximal J associated with the given occupancy of the f-shell. The azimuthal projection angle is free to be chosen, and we denote the angular momentum state with projection axis $\vec{n}$, $|JM_{\vec{n}}\rangle$; then states of the form $\{|J(M_{\vec{n}} = J)\rangle\}$ are formed by a single f-shell Slater determinant composed of the set of generalized spin (spinor) orbitals with maximal projected angular momentum, i.e., $|j(m_{\vec{n}} = j)\rangle$, $|j(m_{\vec{n}} = j-1)\rangle$, etc., where the lowercase j, m denote the single-orbital angular momenta. There is an infinite number of such single-determinant states, obtained by rotating the projection axis $\vec{n}$, and we can use the energies of these states in Eq. 3.3.

In the general case, it may be necessary to partially expand the electronic manifold outside of the specific manifold of interest where $\hat{H}_{\mathrm{CF}}$ is defined, in order to construct low energy states of single-determinant character. For example, if $\hat{H}_{\mathrm{CF}}$ acts on a $\{|JM\rangle\}$ manifold where J is not the maximal J, then we may not find single-determinant states within the $\{|JM\rangle\}$ manifold (e.g., consider the case where $J = 0$). However, by expanding the manifold to multiple J's, $\{|JM\rangle, |J'M'\rangle\}$, we can construct low-energy single determinant states which are not eigenstates of J (i.e.

broken symmetry states) but with well defined $M_{\vec{n}}$ (equal to some specified J). These may be used to fit an effective $\hat{H}_{\mathrm{CF}}$ over the expanded manifold and the effective Hamiltonian can then be restricted to the single manifold of interest after the fact. This more general procedure is analogous to the use of broken-symmetry density functional and wavefunction calculations to determine effective Heisenberg parameters [21, 33, 34].

Formally, the Kohn-Sham density functional energies of the single-determinant states with $M_{\vec{n}} = J$ are defined through

$$E[\rho] = \min_{\Psi(M_{\vec{n}}=J)\rightarrow\rho} \left[\langle\Psi|\hat{h}_1 + \hat{V}_{\mathrm{eff}}|\Psi\rangle\right] \tag{3.4}$$

where Ψ is a Slater determinant with the azimuthal angular momentum constraint, $\hat{h}_1$ is the two-component one-electron part of the Hamiltonian in the given spin-orbit coupling treatment, and $\hat{V}_{\mathrm{eff}}$ includes the Coulomb, exchange, and correlation in a general Kohn-Sham expressoin. In practice, the constraint can be easily implemented by applying a penalty [35], i.e., we minimize

$$E[\rho, \vec{n}, \lambda] = \min_{\Psi\rightarrow\rho} \left[\langle\Psi|\hat{h}_1 + \hat{V}_{\mathrm{eff}}|\Psi\rangle - \lambda(|\vec{J}| - \vec{n}\cdot\vec{J})\right] \tag{3.5}$$

where $\vec{J} = (\langle J_x\rangle, \langle J_y\rangle, \langle J_z\rangle)$. Given such a formal definition, we therefore obtain the energy by minimizing the standard Kohn-Sham density functional energy with the additional penalty, and we choose λ sufficiently large such that the constraint is well satisfied.

Because of the presence of different J multiplets in an actual electronic structure calculation, the result of the above minimization is not a perfect $|J(M_{\vec{n}} = J)\rangle$ state, but contains a small admixture of other J states. To expand the determinant into its $|JM\rangle$ components, we apply the group theoretic projection [36] $C_{JM',i}|\Psi_{JM,i}\rangle = P^J_{M,M'}|\Psi_i\rangle$ where $C_{JM',i} = \langle\Psi_{JM',i} \mid \Psi_i\rangle$, and the operator $P^J_{M,M'}$ is defined as

$$P^J_{M,M'} = \frac{2J+1}{8\pi^2}\int d\Omega D^{J*}_{M,M'}(\Omega)\hat{R}_L(\Omega)\hat{R}_S(\Omega) \tag{3.6}$$

where $\Omega = (\alpha, \beta, \gamma)$ are the Euler angles in z-y-z convention, $\hat{R}_L$ is the orbital rotation operator $\hat{R}_L = e^{-i\alpha\hat{L}_z}e^{-i\beta\hat{L}_y}e^{-i\gamma\hat{L}_z}$, $\hat{R}_S$ is the similarly defined spin rotation operator, and $D^J_{M,M'}(\Omega) = \langle JM \mid \hat{R}(\Omega) \mid JM'\rangle$ is the Wigner D-matrix. The integration in the above can be efficiently computed by quadrature. Once the $|JM\rangle$ coefficients are obtained, we can solve Eq. 3.3 for $h_{JM,J'M'}$ by least squares. We refer to the effective crystal field Hamiltonian derived this way as the constrained DFT ab initio crystal field Hamiltonian.

3.4 Computational implementation and details

We have implemented the above procedure based on the PySCF quantum chemistry package [37, 38]. For the SOC treatment, we used the "exact two-component" Hamiltonian including only the one-electron term (including the one-electron spin-orbit coupling but not including the two-electron spin-same-orbit and spin-other-orbit coupling [39, 40]). For the systems we study below (involving Er, Dy, Ho), the lowest $|JM\rangle$ multiplet is energetically well separated and corresponds to a maximal J for the ground-state f-shell configuration. We first converged the generalized Kohn-Sham calculations without any constraint to find the lowest energy spin-orbit coupled mean-field solution. We then applied spin- and orbital-rotation operators to rotate the $\vec{J}$ vector to generate a new initial guess and minimized the energy with the penalty term $\lambda(\vec{J} \cdot \vec{n} - J)$ for a given $\vec{n}$, using $\lambda = 0.1E_h$. The set of projection axes were chosen to be Haar random, and the generalized Kohn-Sham energies were converged to 10^{-9} E_h. For a fixed target vector $\vec{n}$ and appropriate functionals (see below), we found that this procedure converges to constrained determinants within the ground spin-orbit manifold.

Given these GKS solutions, we evaluated their energies and $C_{JM,i}$ coefficients as outlined above and fitted the crystal field parameters B_k^q to Eq. 3.3. We only included B_k^q up to order $k = 6$ as the higher order terms are conventionally ignored. The matrix forms of the operators O_k^q in the $|JM\rangle$ basis were calculated with the PyCCE program [32].

The structures of Er-trensal (H_3trensal = $2, 2', 2''$-tris(salicylideneimino)triethylamine) (**1**) [8], $Cs_2NaDyCl_6$ (**2**) [41], $(C(NH_2)_3)_5[Er(CO_3)_4]\cdot 11H_2O$ (**3**) [42], $[(Cp^{iPr5})Dy(Cp^*)]^+$ (Cp^{iPr5} = penta-iso-propylcyclopentadienyl; Cp* = pentamethylcyclopentadienyl) (**4**) [43], and $[HoPc_2]^-$ (**5**) [44] were taken from the literature. The z axes of $\hat{H}_{\mathrm{CF}}$ were defined as the pseudo-C_3 symmetry axis, one of the three C_4 axes in the O_h symmetry group, the pseudo-C_{2v} symmetry axis, and the main magnetization axis of the ground Kramers doublet calculated at the CASSCF level with an f-shell active space (because the molecule has no symmetry), and the pseudo-C_4 symmetry axis, respectively.

In the generalized Kohn-Sham calculations, we used the segmented all-electron relativistically contracted basis of valence triple-zeta quality (SARC-TZV) basis [45] for the lanthanides and the 6-31G basis [46–49] for the other elements. As discussed in the results, we performed calculations using pure and hybrid density functionals,

Functional	HF	M06	PBE0	B97-D	B3LYP	PBE	r2SCAN
J	7.5	7.3	7.1	7.1	7.1	6.7	5.9
L	5.1	5.1	5.1	5.1	5.1	4.9	4.6
S	2.4	2.4	2.4	2.3	2.4	2.3	2.4

Table 3.1: The approximate J quantum number as defined by $J(J+1) = \langle J^2 \rangle$ and similarly defined L and S of the lanthanide f-shells in the ground state wavefunction of compound **2**, calculated using HF and various DFT functionals.

namely PBE [50], B97-D [51], TPSS [52], r^{2}SCAN [53],B3LYP [54–56], PBE0[57], M06[58]. It is well known that the ground-spin-state of a metal ion can be strongly influenced by the choice of functional. In these systems we found that the choice of functional can have a significant impact on the effective J state of the ground-state ion, as seen in Table 3.1. In particular, we found that although density functionals (other than, perhaps r^{2}SCAN) give reasonable effective L and S values for the central ion, most do not give ground-state J values consistent with Hund's rule (which here would mean that $J = L + S$). In fact, only the Hartree-Fock functional yielded a ground-state with an overwhelming weight in the Hund's rule $|JM\rangle$ manifold (which is expected to be a well isolated manifold for the ions of interest due to the strong spin-orbit coupling).

Consequently, we also performed calculations where the Slater determinant was determined using generalized Hartree-Fock theory, and the energies were subsequently computed using a different functional, to avoid the above unphysical nature of the DFT ground-state, and in the spirit of minimizing density driven errors in DFT calculations [59]. In the latter case, we refer to the calculation as $X@Y$ where X is the method used to generate the density matrix, and Y is the method use to evaluate the energy. For each compound, 80 target orientations were sampled, except for compound **5** where 120 orientations were used. We estimate that sampling 80 orientations was sufficient to achieve a standard deviation in the relative eigenstate energies of $\hat{H}_{\mathrm{CF}}$ of less than 5 cm^{-1}, 1 cm^{-1}, and 10 cm^{-1} for compounds **1**, **2**, and **3**, respectively.

For the Ho compound (compound **5**) we generated additional benchmark data using CASSCF with spin-orbit coupling included via state-interaction (CASSCF-SISO) and CASSCF/NEVPT2-SISO, which additionally includes dynamical correlations through NEVPT2, using ORCA version 5.0.4 [60, 61] and subsequently, the effective crystal field Hamiltonians were calculated with the SINGLE_ANISO program [8, 62]. In the following, we will refer to the two approaches as CASSCF and NEVPT2, respectively, and similarly refer to CASSCF/CASPT2-SISO as CASPT2. In these calculations, the second-order scalar relativistic Douglas–Kroll–Hess (DKH) Hamiltonian [63, 64] was used for Ho and the second-order DKH transformation was applied to the one-electron part of the SOC operator [65, 66] with the two-electron part of the SOC operator treated by the spin-orbit mean field (SOMF) approximation. [67] The SARC2-DKH-QZVP basis set [68] was used for the Ho atom, and the DKH-def2-TZVP basis set [69, 70] was used for all the other atoms. The spin-orbit interaction was included via quasi-degenerate perturbation theory (QDPT), a type of state interaction method [12, 13], using 35 lowest-energy quintet roots, 106 lowest-energy triplet roots, 31 lowest-energy singlet roots.

Finally, for compound **5**, the finite temperature field-dependent magnetization was simulated with the program PHI [71].

For compounds **2** and **3**, only the central clusters $Er(CO_3)_4$ and $[DyCl_6]^-$ were treated quantum mechanically. The clusters were embedded in infinite lattices of classical charges of the remaining atoms to represent the crystal environment [72]. The classical charges were derived from the Bader population analysis of the Γ-point PBE calculation of the lattices using the VASP program [73–76] with periodic boundary conditions applied to the primitive unit cells and with the energy converged to 10^{-8} eV per cell. These atomic charges were then modeled as Gaussian-distributed charges on the remaining atoms using ionic radii [77] for Er^{3+} and Dy^{3+} and covalent radii [78] for the other atoms.

3.5 Results and discussion

We now discuss the constrained DFT ab initio $\hat{H}_{\mathrm{CF}}$ derived for five single-ion lanthanide magnets: Er-trensal (**1**), $Cs_2NaDyCl_6$ (**2**), $(C(NH_2)_3)_5[Er(CO_3)_4]\cdot 11H_2O$ (**3**), $[(Cp^{i\mathrm{Pr5}})Dy(Cp^*)]^+$ (**4**), and $[HoPc_2]^-$ (**5**). We compare our results to the energies and wavefunctions obtained by diagonalizing model Hamiltonians in the literature, obtained from experiment or multi-configurational methods, and in the case of compound **5**, to additional data computed in this work using multi-configurational methods.

System **1** [84] is a single-ion magnet (SIM) that has been extensively studied both experimentally [79, 80] and theoretically [8, 79]. It has an approximate C_3 symmetry and an Er $^4I_{7.5}$ ground state. Due to the time-reversal symmetry, each eigenstate is doubly degenerate, forming in total 8 Kramers doublets (KDs) in the ground-

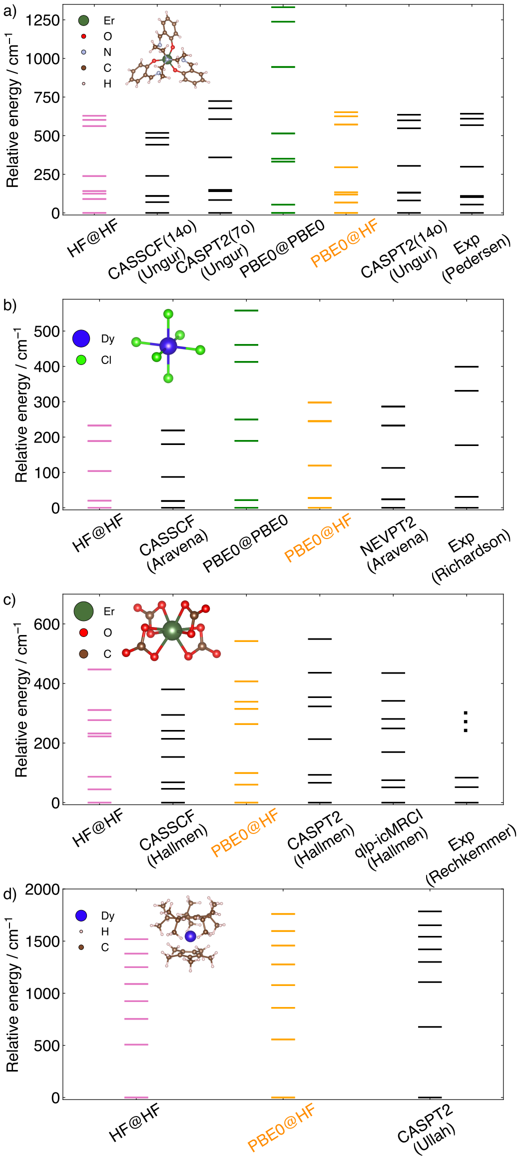

Figure 3.2: Relative energies of ground and low-energy excited states of **1–4** (**a–d**) from $\hat{H}_{\mathrm{CF}}$ using the constrained DFT methodology in this work. Results are shown for three choices of functionals: HF@HF (pink), PBE0@PBE0 (green), and PBE0@HF (orange). We compare to spectra from literature CASSCF, CASPT2 or NEVPT2, and experiments (black) [8, 42, 43, 79–83].

state $J = 7.5$ manifold. Figure 3.2**a** shows the energies of the 16 states from the constrained DFT ab initio crystal field Hamiltonian using the HF, PBE0 [57] and PBE0@HF mean-field functionals, and from theory and experiments in the literature. The HF-derived Hamiltonian yields a spectrum comparable to that of CASSCF, while the PBE0@HF derived $\hat{H}_{\mathrm{CF}}$ yields a spectrum closer to that from the much more expensive XMS-CASPT2 method using the 11 electrons in 14 orbitals active space. In fact, the PBE0@HF $\hat{H}_{\mathrm{CF}}$ and the XMS-CASPT2 (11e, 14o active space) spectrum are in best agreement with the experimentally derived spectrum. We note that using DFT functionals (beyond HF) to include dynamical correlation in our procedure is required to correctly order the closely-spaced 3rd and 4th KDs, and that similarly out of the wavefunction methods only XMS-CASPT2 (11e, 14o active space) obtains the correct ordering of these states. However, the density-driven error effect of DFT can be significant. For example, deriving $\hat{H}_{\mathrm{CF}}$ using the PBE0 density matrix and PBE0 energy leads to worse results, due to the unphysical nature of the ground-state observed above. In general, we find that neglecting dynamical correlation in the modeling (e.g., by using HF energies to derive $\hat{H}_{\mathrm{CF}}$ or by obtaining the spectrum from CASSCF) tends to predict too narrow of a spectral spread while dynamical correlation (e.g., using our PBE0@HF energies, or from literature CASPT2 results) results in a larger spread, more comparable to that of experiment.

Similar observations apply to complexes **2**-**4**: the ab initio crystal field Hamiltonian derived from Hartree-Fock energies produces a spectrum comparable to the literature CASSCF derived spectra, while using DFT energies evaluated for the Hartree-Fock density matrices, such as when using PBE0@HF to derive $\hat{H}_{\mathrm{CF}}$, yields (for most functionals) spectra comparable to the best multi-reference perturbation theory results in the literature, with similarly good agreement with experiment where available (see Figure 3.2, 3.3, 3.6, and 3.7).

We observe that our ab initio $\hat{H}_{\mathrm{CF}}$ also accurately predicts the $|JM\rangle$ composition of the crystal field eigenstates. We consider, for example, compound **1**. As shown in Figure 3.4, the $\hat{H}_{\mathrm{CF}}$ derived from the PBE0@HF energies yields $|JM\rangle$ compositions for the 8 Kramers doublets that deviate from the experimentally derived compositions by only 0.6% on average. To obtain a similar accuracy in a multiconfigurational calculation requires using a second-order perturbative correction and a large active space of 14o as neither CASSCF(14o) nor CASPT2(7o) capture the correct energy ordering, as seen in Figure 3.4.

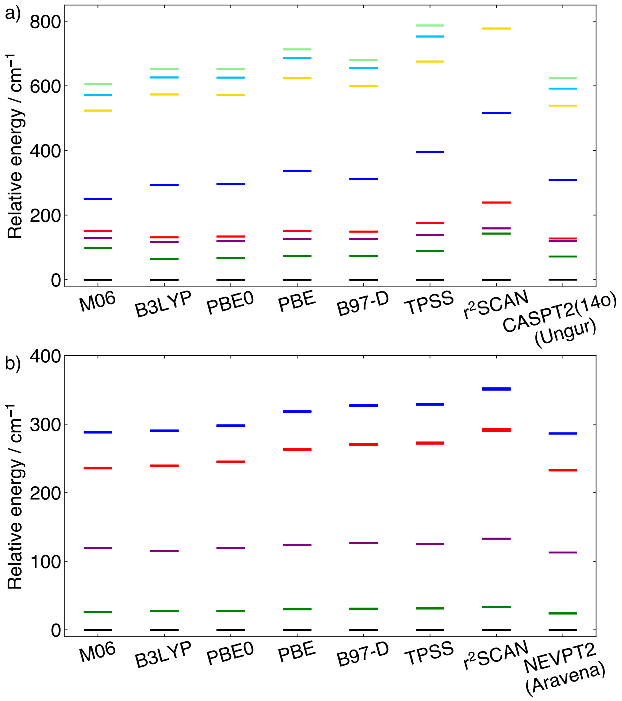

Figure 3.3: Relative eigenstate energies of **a**) **1** and **b**) **2** from $\hat{H}_{\mathrm{CF}}$ derived from DFT@HF sampled energies with various DFT functionals [51–58]. We compare to the best available multireference perturbation theory calculations using CASPT2 [8] or NEVPT2 [42] (last column). Each color represents a doublet in **a**) and an energy level with ideally 2 or 4 degeneracy in **b**).

Lastly, we investigate a larger complex, the holmium double decker compound **5** [85]. Since its discovery two decades ago as one of the first lanthanide SIMs [85], multiple experiments and calculations have sought to understand the relative energies and wavefunctions of the ground-state J manifold [44, 85, 86], but have arrived at different conclusions. The primary challenge in this compound is that the size of the molecule makes it computationally challenging to apply CASPT2 or NEVPT2 levels of theory in conjunction with (potentially necessary) large active spaces and large basis sets.

However, the computational efficiency of our method allows it to be readily applied. Figure 3.5 compares the excitation energies predicted using $\hat{H}_{\mathrm{CF}}$ derived using our method and PBE0@HF energies, compared to predictions from other techniques. As shown in Figure 3.5, the excitation energies predicted by our method match the peaks in the spectrum very well. (Note that the experimental peak near 150 cm^{-1} is a phonon peak and should be ignored). In contrast, neither the ligand field model directly fitted to NMR and susceptibility experiments ("Exp fit") [85]

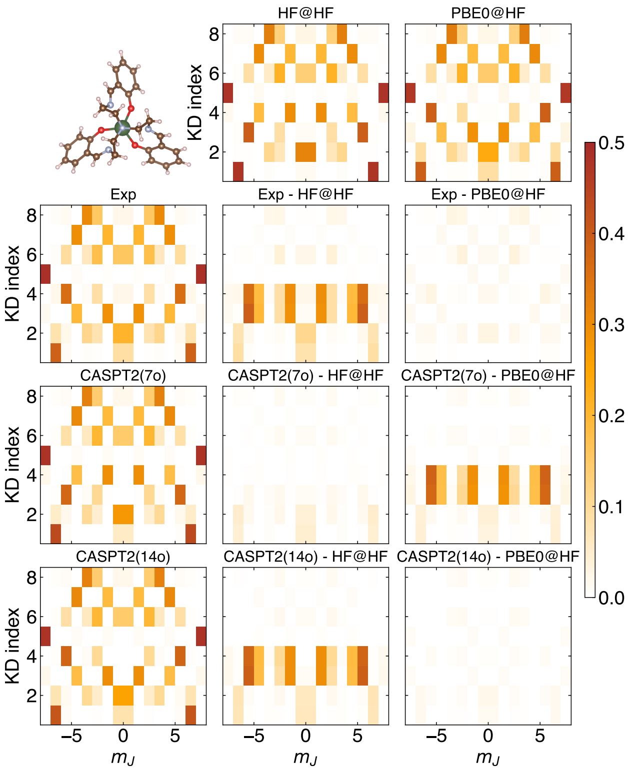

Figure 3.4: $|JM\rangle$ compositions, $|c_{JM}|^2$ where $c_{JM} = \langle JM\,|\,\Psi\rangle$, of each Kramers doublet (KD) of **1** from diagonalizing $\hat{H}_{\text{CF}}$. Each panel corresponds to a different $\hat{H}_{\text{CF}}$, derived from the constrained DFT methodology using the HF@HF functional ("HF@HF") and PBE0@HF functional ("PBE0@HF"), from experimental measurements [79] ("Exp"), from CASPT2 in a 7-orbital active space ("CASPT2(7o)") [8], and from CASPT2 in a 14-orbital active space ("CASPT2(14o)") [8], as well as differences between pairs. $|JM\rangle$ compositions of a KD are calculated as the average $|c_{JM}|^2$ of the two corresponding degenerate eigenstates.

nor the parameterized effective point charge model fit to experimental χT curves ("Point charge") [86] correctly captures the second set of excited quasi-doublets (purple). The energies predicted by CASSCF (7o) must be rescaled by an empirical factor 1.3 to match the lowest three observed excited quasi-doublets in the spectrum [44] while our method requires no empirical adjustment. We also performed NEVPT2 calculations using a 7-orbital active space, which, at the CASSCF level, accurately reproduced the CASSCF (7o) results in the literature [44], and found that the excitations deviate from the experimental spectrum even more than the CASSCF results, perhaps due to the small active space, as observed previously in compound **1**. To further compare against experimental observables, we computed the field-dependent magnetization (Figure 3.5**b**) and temperature-dependent

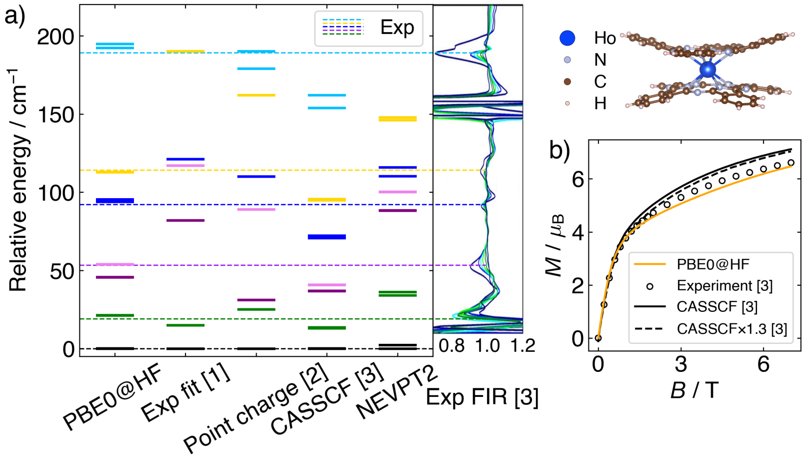

Figure 3.5: **a**) Relative energies of ground and low-energy excited states of **5** from $\hat{H}_{\mathrm{CF}}$ fitted to HF determinants and PBE0 energies ("PBE0@HF"), from $\hat{H}_{\mathrm{CF}}$ fitted to NMR and susceptibility experiments [85] ("Exp fit [1]"), from a point charge model [86] ("Point charge [2]"), from CASSCF in an active space of (10e, 14o) [44] ("CASSCF [3]"), and from NEVPT2 in an active space of (10e, 7o), in comparison with the experimental FIR spectrum [44] ("Exp FIR [3]"). The energy levels are grouped into quasi-doublets, with each pair–along with the corresponding experimental peaks (dashed lines)–colored consistently according to their energy order. The light and dark purple quasi-doublets are both assigned to the broad FIR peak near 51 cm^{-1}. The peak near 150 cm^{-1} in the experimental FIR spectrum is likely phononic instead of magnetic and thus ignored. Experimental FIR spectrum is reproduced with permission from the reference by Marx, et al. [44]. **b**) Calculated magnetization ("PBE0@HF") as a function of the applied field at 1.8 K on a powder sample of **5**, in comparison with the literature [44]: the experimental measurement ("Experiment [3]"), the prediction from CASSCF as in **a**) ("CASSCF [3]"), the prediction after the CASSCF relative energies are scaled by 1.3 ("CASSCF×1.3 [3]").

magnetic susceptibility (Figure 3.10) using our ab initio $\hat{H}_{\mathrm{CF}}$, where we find good agreement with the experimentally measured curves, improving on the CASSCF derived curves.

3.6 Conclusion

In conclusion, we have developed a method to determine the effective crystal field Hamiltonian of single-ion magnets with quantitative accuracy at mean-field cost. The accuracy of the crystal field Hamiltonian parameters that we obtain is comparable to that of the best multi-reference perturbation theory calculations in the literature, as we have demonstrated on four benchmark literature systems. In addition, we showcased an application to the large holmium double decker complex whose low-energy spectrum has previously been challenging to assign theoretically. Using our mean-field derived Hamiltonian, we were able to reproduce all low-energy states measured in the experimental spectra as well as the field-dependent magnetic susceptibility curve. The low-computational cost and high-accuracy of our approach will allow for applications to larger and more complex molecules and thus lays the foundation for future quantitative simulations of the low-energy physics of single-ion magnets and optimizing their design.

3.7 Appendix

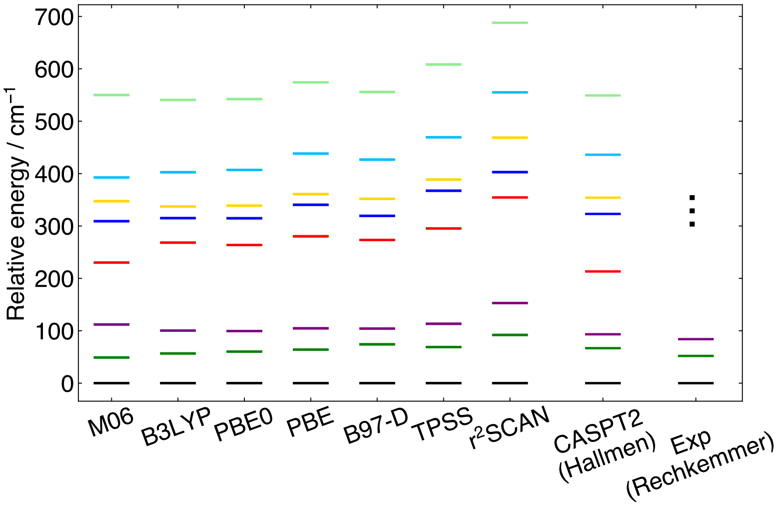

Figure 3.6: Relative energies of eigenstates of **3** when different DFT functionals are used to evaluate energy expectation values of cHF determinants in comparison to values from CASPT2 [82] and experiments [83] (last two columns). Each color represents a degenerate doublet.

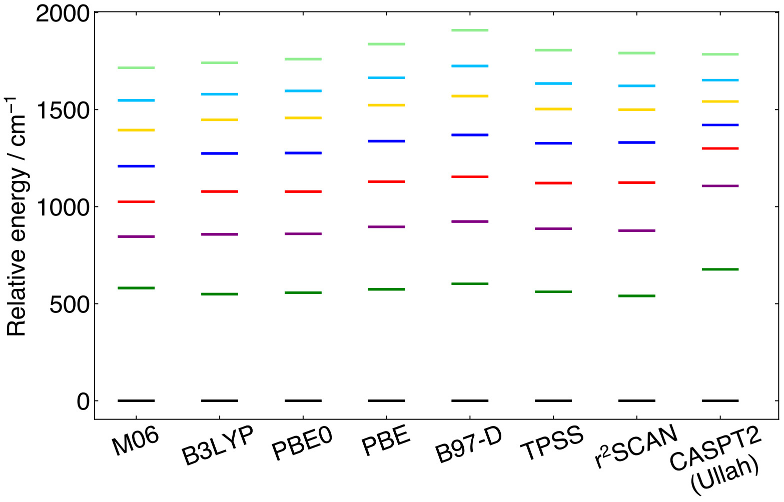

Figure 3.7: Relative energies of eigenstates of **4** when different DFT functionals are used to evaluate energy expectation values of cHF determinants in comparison to values calculated by CASPT2 [43] (last column). Each color represents a degenerate doublet.

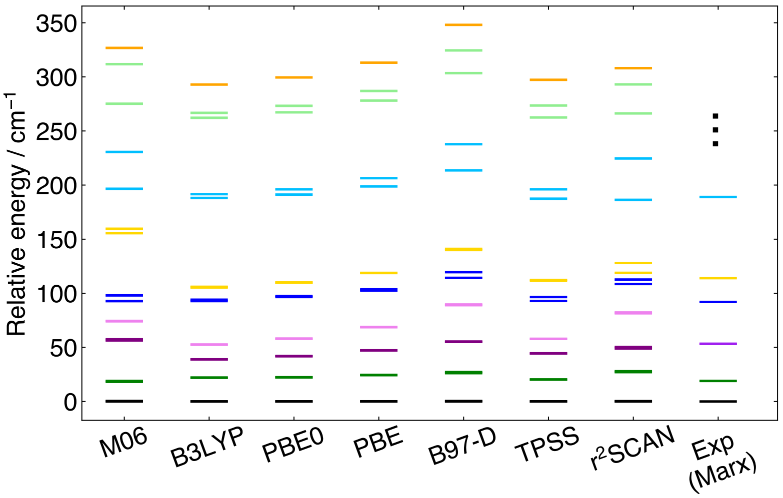

Figure 3.8: Relative energies of eigenstates of **5** when different DFT functionals are used to evaluate energy expectation values of cHF determinants in comparison to values extracted from the experiment [44] (last column). Each color except black represents a quasi-doublet.

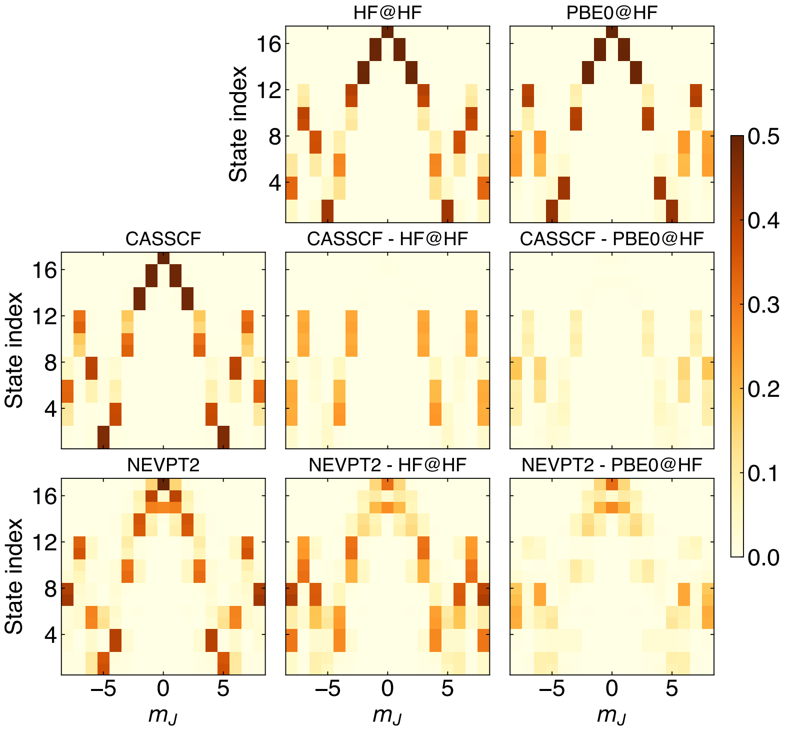

Figure 3.9: $|JM\rangle$ compositions, $|c_{JM}|^2$ where $c_{JM} = \langle JM \mid \Psi\rangle$, of each eigenstate of **5** from diagonalizing $\hat{H}_{\text{CF}}$. Each panel corresponds to a different $\hat{H}_{\text{CF}}$, derived from the constrained DFT methodology using HF@HF functional ("HF@HF") and PBE0@HF functional ("PBE0@HF"), from CASSCF in an active space of (10e, 14o)("CASSCF"), and by NEVPT2 in an active space of (10e, 7o) ("NEVPT2"), as well as differences between pairs.

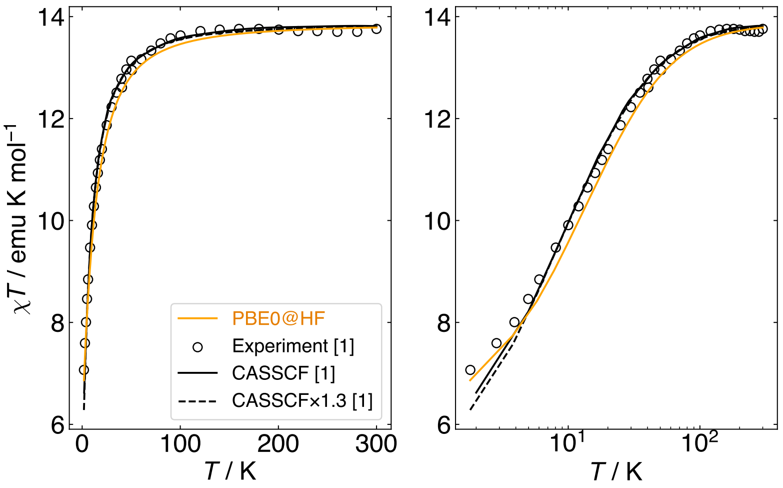

Figure 3.10: Calculated magnetic susceptibility (“PBE0@HF”) as a function of temperature on a powder sample of **5**, in comparison with the literature [44]: the experimental measurement (“Experiment [1]”), the prediction from CASSCF in an active space of (10e, 14o) (“CASSCF [1]”), the prediction after the CASSCF relative energies are scaled by 1.3 (“CASSCF×1.3 [1]”). Note: the main mismatch between the experiment and all theoretical calculations at high temperatures is likely due to experimental uncertainties because χT is expected to change monotonically in the high temperature regime.

References

1. Christou, G., Gatteschi, D., Hendrickson, D. N. & Sessoli, R. Single-molecule magnets. *MRS Bulletin* **25,** 66–71. doi:`10.1557/mrs2000.226` (2000).
2. Sessoli, R. Magnetic molecules back in the race. *Nature* **548,** 400–401. doi:`10.1038/548400a` (2017).
3. Bogani, L. & Wernsdorfer, W. Molecular spintronics using single-molecule magnets. *Nature Materials* **7,** 179–186. doi:`10.1038/nmat2133` (2008).
4. Thiele, S., Balestro, F., Ballou, R., Klyatskaya, S., Ruben, M. & Wernsdorfer, W. Electrically driven nuclear spin resonance in single-molecule magnets. *Science* **344,** 1135–1138. doi:`10.1126/science.1249802` (2014).
5. Gaita-Ariño, A., Luis, F., Hill, S. & Coronado, E. Molecular spins for quantum computation. *Nature Chemistry* **11,** 301–309. doi:`10.1038/s41557-019-0232-y` (2019).
6. Atzori, M. & Sessoli, R. The second quantum revolution: Role and challenges of molecular chemistry. *Journal of the American Chemical Society* **141,** 11339–11352. doi:`10.1021/jacs.9b00984` (2019).
7. Bayliss, S., Laorenza, D., Mintun, P., Kovos, B., Freedman, D. E. & Awschalom, D. Optically addressable molecular spins for quantum information processing. *Science* **370,** 1309–1312. doi:`10.1126/science.abb9352` (2020).
8. Ungur, L. & Chibotaru, L. F. Ab initio crystal field for lanthanides. *Chemistry–A European Journal* **23,** 3708–3718. doi:`10.1002/chem.201605102` (2017).
9. Gómez-Coca, S., Aravena, D., Morales, R. & Ruiz, E. Large magnetic anisotropy in mononuclear metal complexes. *Coordination Chemistry Reviews* **289-290.** Progress in Magnetochemistry, 379–392. ISSN: 0010-8545. doi:`10.1016/j.ccr.2015.01.021` (2015).
10. Atanasov, M., Ganyushin, D., Sivalingam, K. & Neese, F. in *Molecular Electronic Structures of Transition Metal Complexes II* (eds Mingos, D. M. P., Day, P. & Dahl, J. P.) 149–220 (Springer Berlin Heidelberg, Berlin, Heidelberg, 2012). doi:`10.1007/430_2011_57`.
11. Roos, B. O., Taylor, P. R. & Sigbahn, P. E. A complete active space SCF method (CASSCF) using a density matrix formulated super-CI approach. *Chemical Physics* **48,** 157–173. doi:`10.1016/0301-0104(80)80045-0` (1980).
12. Malmqvist, P.-Å. & Roos, B. O. The CASSCF state interaction method. *Chemical Physics Letters* **155,** 189–194. doi:`10.1016/0009-2614(89)85347-3` (1989).

13. Malmqvist, P.-Å., Roos, B. O. & Schimmelpfennig, B. The restricted active space (RAS) state interaction approach with spin–orbit coupling. *Chemical Physics Letters* **357,** 230–240. doi:`10.1016/s0009-2614(02)00498-0` (2002).

14. Andersson, K., Malmqvist, P.-Å., Roos, B. O., Sadlej, A. J. & Wolinski, K. Second-order perturbation theory with a CASSCF reference function. *Journal of Physical Chemistry* **94,** 5483–5488. doi:`10.1021/j100377a012` (1990).

15. Andersson, K., Malmqvist, P.-Å. & Roos, B. O. Second-order perturbation theory with a complete active space self-consistent field reference function. *The Journal of Chemical Physics* **96,** 1218–1226. doi:`10.1063/1.462209` (1992).

16. Angeli, C., Cimiraglia, R., Evangelisti, S., Leininger, T. & Malrieu, J.-P. Introduction of n-electron valence states for multireference perturbation theory. *The Journal of Chemical Physics* **114,** 10252–10264. doi:`10.1063/1.1361246` (2001).

17. Angeli, C., Cimiraglia, R. & Malrieu, J.-P. N-electron valence state perturbation theory: a fast implementation of the strongly contracted variant. *Chemical Physics Letters* **350,** 297–305. doi:`10.1016/S0009-2614(01)01303-3` (2001).

18. Buenker, R. J. & Peyerimhoff, S. D. Individualized configuration selection in CI calculations with subsequent energy extrapolation. *Theoretica Chimica Acta* **35,** 33–58. doi:`10.1007/PL00020553` (1974).

19. Buenker, R. J. & Peyerimhoff, S. D. Energy extrapolation in CI calculations. *Theoretica Chimica Acta* **39,** 217–228. doi:`10.1007/BF00555301` (1975).

20. Werner, H.-J. & Knowles, P. J. An efficient internally contracted multiconfiguration–reference configuration interaction method. *The Journal of Chemical Physics* **89,** 5803–5814. doi:`10.1063/1.455556` (1988).

21. Schurkus, H., Chen, D.-T., Cheng, H.-P., Chan, G. & Stanton, J. Theoretical prediction of magnetic exchange coupling constants from broken-symmetry coupled cluster calculations. *The Journal of Chemical Physics* **152.** doi:`10.1063/1.5144696` (2020).

22. Atanasov, M., Daul, C., Güdel, H.-U., Wesolowski, T. A. & Zbiri, M. Ground States, Excited States, and Metal- Ligand Bonding in Rare Earth Hexachloro Complexes: A DFT-Based Ligand Field Study. *Inorganic Chemistry* **44,** 2954–2963. doi:`10.1021/ic040105t` (2005).

23. Kaduk, B., Kowalczyk, T. & Van Voorhis, T. Constrained density functional theory. *Chemical Reviews* **112,** 321–370. doi:`10.1021/cr200148b` (2012).

24. Behler, J., Delley, B., Lorenz, S., Reuter, K. & Scheffler, M. Dissociation of O 2 at Al (111): The role of spin selection rules. *Physical Review Letters* **94,** 036104. doi:`10.1103/PhysRevLett.94.036104` (2005).

25. Dederichs, P., Blügel, S., Zeller, R. & Akai, H. Ground states of constrained systems: application to cerium impurities. *Physical Review Letters* **53,** 2512. doi:`10.1103/PhysRevLett.53.2512` (1984).

26. Behler, J., Delley, B., Reuter, K. & Scheffler, M. Nonadiabatic potential-energy surfaces by constrained density-functional theory. *Physical Review B—Condensed Matter and Materials Physics* **75,** 115409. doi:`10.1103/PhysRevB.75.115409` (2007).

27. Wu, Q. & Van Voorhis, T. Direct optimization method to study constrained systems within density-functional theory. *Physical Review A* **72,** 024502. doi:`10.1103/PhysRevA.72.024502` (2005).

28. Stevens, K. Matrix elements and operator equivalents connected with the magnetic properties of rare earth ions. *Proceedings of the Physical Society. Section A* **65,** 209. doi:`10.1088/0370-1298/65/3/308` (1952).

29. Rudowicz, C. Transformation relations for the conventional Okq and normalised O'kq Stevens operator equivalents with $k = 1$ to 6 and$-k \leq q \leq k$. *Journal of Physics C: Solid State Physics* **18,** 1415. doi:`10.1088/0022-3719/18/7/009` (1985).

30. Rudowicz, C. & Chung, C. The generalization of the extended Stevens operators to higher ranks and spins, and a systematic review of the tables of the tensor operators and their matrix elements. *Journal of Physics: Condensed Matter* **16,** 5825. doi:`10.1088/0953-8984/16/32/018` (2004).

31. Ryabov, I. On the generation of operator equivalents and the calculation of their matrix elements. *Journal of Magnetic Resonance* **140,** 141–145. doi:`10.1006/jmre.1999.1783` (1999).

32. Onizhuk, M. & Galli, G. Pycce: A python package for cluster correlation expansion simulations of spin qubit dynamics. *Advanced Theory and Simulations* **4,** 2100254. doi:`10.1002/adts.202100254` (2021).

33. Noodleman, L. Valence bond description of antiferromagnetic coupling in transition metal dimers. *The Journal of Chemical Physics* **74,** 5737–5743. doi:`10.1063/1.440939` (1981).

34. Yamaguchi, K., Takahara, Y. & Fueno, T. in *Applied Quantum Chemistry* (eds Smith, V. H., Schaefer, H. F. & Morokuma, K.) 155–184 (Springer Netherlands, Dordrecht, 1986). doi:`10.1007/978-94-009-4746-7_11`.

35. Ma, P.-W. & Dudarev, S. Constrained density functional for noncollinear magnetism. *Physical Review B* **91,** 054420. doi:`10.1103/PhysRevB.91.054420` (2015).

36. Percus, J. & Rotenberg, A. Exact eigenfunctions of angular momentum by rotational projection. *Journal of Mathematical Physics* **3,** 928–932. doi:`10.1063/1.1724308` (1962).

37. Sun, Q., Berkelbach, T. C., Blunt, N. S., Booth, G. H., Guo, S., Li, Z., Liu, J., McClain, J. D., Sayfutyarova, E. R., Sharma, S., *et al.* PySCF: the Python-based simulations of chemistry framework. *Wiley Interdisciplinary Reviews: Computational Molecular Science* **8,** e1340. doi:`10.1002/wcms.1340` (2018).

38. Sun, Q., Zhang, X., Banerjee, S., Bao, P., Barbry, M., Blunt, N. S., Bogdanov, N. A., Booth, G. H., Chen, J., Cui, Z.-H., *et al.* Recent developments in the PySCF program package. *The Journal of Chemical Physics* **153,** 024109. doi:`10.1063/5.0006074` (2020).

39. Li, Z., Xiao, Y. & Liu, W. On the spin separation of algebraic two-component relativistic Hamiltonians: Molecular properties. *The Journal of Chemical Physics* **141.** doi:`10.1063/1.4891567` (2014).

40. Liu, W. & Peng, D. Exact two-component Hamiltonians revisited. *The Journal of Chemical Physics* **131.** doi:`10.1063/1.3159445` (2009).

41. Goff, G. S., Cisneros, M. R., Kluk, C., Williamson, K., Scott, B., Reilly, S. & Runde, W. Synthesis and structural characterization of molecular Dy (III) and Er (III) tetra-carbonates. *Inorganic Chemistry* **49,** 6558–6564. doi:`10.1021/ic1004598` (2010).

42. Aravena, D., Atanasov, M. & Neese, F. Periodic trends in lanthanide compounds through the eyes of multireference ab initio theory. *Inorganic Chemistry* **55,** 4457–4469. doi:`10.1021/acs.inorgchem.6b00244` (2016).

43. Ullah, A., Cerdá, J., Baldoví, J. J., Varganov, S. A., Aragó, J. & Gaita-Arino, A. In silico molecular engineering of dysprosocenium-based complexes to decouple spin energy levels from molecular vibrations. *The Journal of Physical Chemistry Letters* **10,** 7678–7683. doi:`10.1021/acs.jpclett.9b02982` (2019).

44. Marx, R., Moro, F., Dörfel, M., Ungur, L., Waters, M., Jiang, S., Orlita, M., Taylor, J., Frey, W., Chibotaru, L., *et al.* Spectroscopic determination of crystal field splittings in lanthanide double deckers. *Chemical Science* **5,** 3287–3293. doi:`10.1039/C4SC00751D` (2014).

45. Pantazis, D. A. & Neese, F. All-electron scalar relativistic basis sets for the lanthanides. *Journal of Chemical Theory and Computation* **5,** 2229–2238. doi:`10.1021/ct900090f` (2009).

46. Ditchfield, R., Hehre, W. J. & Pople, J. A. Self-Consistent Molecular-Orbital Methods. IX. An Extended Gaussian-Type Basis for Molecular-Orbital Studies of Organic Molecules. *The Journal of Chemical Physics* **54,** 724–728. doi:`10.1063/1.1674902` (1971).

47. Hehre, W. J., Ditchfield, R. & Pople, J. A. Self-Consistent Molecular Orbital Methods. XII. Further Extensions of Gaussian-Type Basis Sets for Use in Molecular Orbital Studies of Organic Molecules. *The Journal of Chemical Physics* **56,** 2257–2261. doi:`10.1063/1.1677527` (1972).

48. Francl, M. M., Pietro, W. J., Hehre, W. J., Binkley, J. S., Gordon, M. S., DeFrees, D. J. & Pople, J. A. Self-consistent molecular orbital methods. XXIII. A polarization-type basis set for second-row elements. *The Journal of Chemical Physics* **77,** 3654–3665. doi:`10.1063/1.444267` (1982).

49. Gordon, M. S., Binkley, J. S., Pople, J. A., Pietro, W. J. & Hehre, W. J. Self-consistent molecular-orbital methods. 22. Small split-valence basis sets for second-row elements. *Journal of the American Chemical Society* **104,** 2797–2803. doi:`10.1021/ja00374a017` (1982).

50. Perdew, J. P., Burke, K. & Ernzerhof, M. Generalized gradient approximation made simple. *Physical Review Letters* **77,** 3865. doi:`10.1103/PhysRevLett.77.3865` (1996).

51. Grimme, S. Semiempirical GGA-type density functional constructed with a long-range dispersion correction. *Journal of Computational Chemistry* **27,** 1787–1799. doi:`10.1002/jcc.20495` (2006).

52. Tao, J., Perdew, J. P., Staroverov, V. N. & Scuseria, G. E. Climbing the density functional ladder: Nonempirical meta–generalized gradient approximation designed for molecules and solids. *Physical Review Letters* **91,** 146401. doi:`10.1103/PhysRevLett.91.146401` (2003).

53. Furness, J. W., Kaplan, A. D., Ning, J., Perdew, J. P. & Sun, J. Accurate and numerically efficient r2SCAN meta-generalized gradient approximation. *The Journal of Physical Chemistry Letters* **11,** 8208–8215. doi:`10.1021/acs.jpclett.0c02405` (2020).

54. Becke, A. D. Density-functional exchange-energy approximation with correct asymptotic behavior. *Physical Review A* **38,** 3098. doi:`10.1103/PhysRevA.38.3098` (1988).

55. Lee, C., Yang, W. & Parr, R. G. Development of the Colle-Salvetti correlation-energy formula into a functional of the electron density. *Physical Review B* **37,** 785. doi:`10.1103/PhysRevB.37.785` (1988).

56. Becke, A. D. A new mixing of Hartree–Fock and local density-functional theories. *The Journal of Chemical Physics* **98,** 1372–1377. doi:`10.1063/1.464304` (1993).

57. Perdew, J. P., Ernzerhof, M. & Burke, K. Rationale for mixing exact exchange with density functional approximations. *The Journal of Chemical Physics* **105,** 9982–9985. doi:`10.1063/1.472933` (1996).

58. Zhao, Y. & Truhlar, D. G. The M06 suite of density functionals for main group thermochemistry, thermochemical kinetics, noncovalent interactions, excited states, and transition elements: two new functionals and systematic testing of four M06-class functionals and 12 other functionals. *Theoretical Chemistry Accounts* **120,** 215–241. doi:`10.1007/s00214-007-0310-x` (2008).

59. Vuckovic, S., Song, S., Kozlowski, J., Sim, E. & Burke, K. Density functional analysis: The theory of density-corrected DFT. *Journal of Chemical Theory and Computation* **15,** 6636–6646. doi:`10.1021/acs.jctc.9b00826` (2019).

60. Neese, F. The ORCA program system. *Wiley Interdisciplinary Reviews: Computational Molecular Science* **2,** 73–78. doi:`10.1002/wcms.81` (2012).

61. Neese, F. Software update: The ORCA program system—Version 5.0. *Wiley Interdisciplinary Reviews: Computational Molecular Science* **12,** e1606. doi:`10.1002/wcms.1606` (2022).

62. Chibotaru, L. F. & Ungur, L. Ab initio calculation of anisotropic magnetic properties of complexes. I. Unique definition of pseudospin Hamiltonians and their derivation. *The Journal of Chemical Physics* **137.** doi:`10.1063/1.4739763` (2012).

63. Douglas, M. & Kroll, N. M. Quantum electrodynamical corrections to the fine structure of helium. *Annals of Physics* **82,** 89–155. ISSN: 00034916. doi:`10.1016/0003-4916(74)90333-9` (1974).

64. Hess, B. A. Applicability of the no-pair equation with free-particle projection operators to atomic and molecular structure calculations. *Physical Review A* **32,** 756–763. ISSN: 0556-2791. doi:`10.1103/PhysRevA.32.756` (1985).

65. Neese, F., Wolf, A., Fleig, T., Reiher, M. & Hess, B. A. Calculation of electric-field gradients based on higher-order generalized Douglas–Kroll transformations. *The Journal of Chemical Physics* **122.** doi:`10.1063/1.1904589` (2005).

66. Sandhoefer, B. & Neese, F. One-electron contributions to the g-tensor for second-order Douglas–Kroll–Hess theory. *The Journal of Chemical Physics* **137.** doi:`10.1063/1.4747454` (2012).

67. Heß, B. A., Marian, C. M., Wahlgren, U. & Gropen, O. A mean-field spin-orbit method applicable to correlated wavefunctions. *Chemical Physics Letters* **251,** 365–371. doi:`10.1016/0009-2614(96)00119-4` (1996).

68. Aravena, D., Neese, F. & Pantazis, D. A. Improved Segmented All-Electron Relativistically Contracted Basis Sets for the Lanthanides. *Journal of Chemical Theory and Computation* **12,** 1148–1156. doi:`10.1021/acs.jctc.5b01048` (2016).

69. Pantazis, D. A., Chen, X.-Y., Landis, C. R. & Neese, F. All-Electron Scalar Relativistic Basis Sets for Third-Row Transition Metal Atoms. *Journal of Chemical Theory and Computation* **4,** 908–919. doi:`10.1021/ct800047t` (2008).

70. Weigend, F. & Ahlrichs, R. Balanced basis sets of split valence, triple zeta valence and quadruple zeta valence quality for H to Rn: Design and assessment of accuracy. *Physical Chemistry Chemical Physics* **7,** 3297–3305. doi:`10.1039/b508541a` (2005).

71. Chilton, N. F., Anderson, R. P., Turner, L. D., Soncini, A. & Murray, K. S. PHI: A powerful new program for the analysis of anisotropic monomeric and exchange-coupled polynuclear d-and f-block complexes. *Journal of Computational Chemistry* **34,** 1164–1175. doi:`10.1002/jcc.23234` (2013).

72. Li, C. & Chan, G. K.-L. Accurate QM/MM molecular dynamics for periodic systems in GPU4PySCF with applications to enzyme catalysis. *Journal of Chemical Theory and Computation.* doi:`10.1021/acs.jctc.4c01698` (2025).

73. Kresse, G. & Hafner, J. Ab initio molecular dynamics for liquid metals. *Physical Review B* **47,** 558. doi:`10.1103/PhysRevB.47.558` (1993).

74. Kresse, G. & Hafner, J. Ab initio molecular-dynamics simulation of the liquid-metal–amorphous-semiconductor transition in germanium. *Physical Review B* **49,** 14251. doi:`10.1103/PhysRevB.49.14251` (1994).

75. Kresse, G. & Furthmüller, J. Efficiency of ab-initio total energy calculations for metals and semiconductors using a plane-wave basis set. *Computational Materials Science* **6,** 15–50. doi:`10.1016/0927-0256(96)00008-0` (1996).

76. Kresse, G. & Furthmüller, J. Efficient iterative schemes for ab initio total-energy calculations using a plane-wave basis set. *Physical Review B* **54,** 11169. doi:`10.1103/PhysRevB.54.11169` (1996).

77. Shannon, R. D. Revised effective ionic radii and systematic studies of interatomic distances in halides and chalcogenides. *Foundations of Crystallography* **32,** 751–767. doi:`10.1107/S0567739476001551` (1976).

78. Pyykkö, P. & Atsumi, M. Molecular single-bond covalent radii for elements 1–118. *Chemistry–A European Journal* **15,** 186–197. doi:`10.1002/chem.200800987` (2009).

79. Pedersen, K. S., Ungur, L., Sigrist, M., Sundt, A., Schau-Magnussen, M., Vieru, V., Mutka, H., Rols, S., Weihe, H., Waldmann, O., *et al.* Modifying the properties of 4f single-ion magnets by peripheral ligand functionalisation. *Chemical Science* **5,** 1650–1660. doi:`10.1039/C3SC53044B` (2014).

80. Flanagan, B. M., Bernhardt, P. V., Krausz, E. R., Lüthi, S. R. & Riley, M. J. Ligand-field analysis of an Er (III) complex with a heptadentate tripodal N4O3 ligand. *Inorganic Chemistry* **40,** 5401–5407. doi:`10.1021/ic0103244` (2001).

81. Richardson, F., Reid, M. F., Dallara, J. J. & Smith, R. D. Energy levels of lanthanide ions in the cubic Cs2NaLnCl6 and Cs2NaYCl6: Ln3+ (doped) systems. *The Journal of Chemical Physics* **83,** 3813–3830. doi:`10.1063/1.449092` (1985).

82. Hallmen, P. P., Rauhut, G., Stoll, H., Mitrushchenkov, A. & van Slageren, J. Crystal field splittings in lanthanide complexes: inclusion of correlation effects beyond second order perturbation theory. *Journal of Chemical Theory and Computation* **14,** 3998–4009. doi:`10.1021/acs.jctc.8b00184` (2018).

83. Rechkemmer, Y., Fischer, J. E., Marx, R., Dörfel, M., Neugebauer, P., Horvath, S., Gysler, M., Brock-Nannestad, T., Frey, W., Reid, M. F., *et al.* Comprehensive spectroscopic determination of the crystal field splitting in an erbium single-ion magnet. *Journal of the American Chemical Society* **137,** 13114–13120. doi:`10.1021/jacs.5b08344` (2015).

84. Kanesato, M. & Yokoyama, T. Synthesis and structural characterization of Ln (III) complexes (Ln= Eu, Gd, Tb, Er, Tm, Lu) of tripodal tris [2-(salicylideneamino) ethyl] amine. *Chemistry Letters* **28,** 137–138. doi:`10.1246/cl.1999.137` (1999).

85. Ishikawa, N., Sugita, M., Ishikawa, T., Koshihara, S.-y. & Kaizu, Y. Lanthanide double-decker complexes functioning as magnets at the single-molecular level. *Journal of the American Chemical Society* **125,** 8694–8695. doi:`10.1021/ja029629n` (2003).

86. Baldoví, J. J., Borrás-Almenar, J. J., Clemente-Juan, J. M., Coronado, E. & Gaita-Ariño, A. Modeling the properties of lanthanoid single-ion magnets using an effective point-charge approach. *Dalton Trans.* **41,** 13705–13710. doi:`10.1039/C2DT31411H` (44 2012).

Chapter 4

FERMIONIC REDUCED DENSITY LOW-RANK MATRIX COMPLETION, NOISE FILTERING, AND MEASUREMENT REDUCTION IN QUANTUM SIMULATIONS

This chapter is based on the published article reprinted with permission from:

1. **Peng, L**, Zhang, X. & Chan, G. K.-L. Fermionic reduced density low-rank matrix completion, noise filtering, and measurement reduction in quantum simulations. *Journal of Chemical Theory and Computation* **19,** 9151–9160. doi:`10.1021/acs.jctc.3c00851` (2023).

4.1 Abstract

Fermionic reduced density matrices summarize the key observables in fermionic systems. In electronic systems, the two-particle reduced density matrix (2-RDM) is sufficient to determine the energy and most physical observables of interest. Here, we consider the possibility of using matrix completion to reconstruct the two-particle reduced density matrix to chemical accuracy from partial information. We consider the case of noiseless matrix completion, where the partial information corresponds to a subset of the 2-RDM elements, as well as noisy completion, where the partial information corresponds to both a subset of elements, as well as statistical noise in their values. Through experiments on a set of 24 molecular systems, we find that the 2-RDM can be efficiently reconstructed from a reduced amount of information. In the case of noisy completion, this results in multiple orders of magnitude reduction in the number of measurements needed to determine the 2-RDM to chemical accuracy. These techniques can be readily applied to both classical and quantum algorithms for quantum simulations.

4.2 Introduction

Although quantum states live in a Hilbert space that is exponentially large in physical system size, most information of physical interest can be captured by quantities of much reduced dimension. For time-independent fermionic observables, the relevant quantities are the fermionic reduced density matrices (RDMs) [1, 2]. For example, the k-RDM, defined as

$$ {}^{k}P_{i_1 i_2 \dots i_k, i'_1 i'_2 i'_k} = \langle \Psi | a^{\dagger}_{i_1} a^{\dagger}_{i_2} \dots a^{\dagger}_{i_k} a_{i'_k} \dots a_{i'_2} a_{i'_1} | \Psi \rangle \tag{4.1} $$

where $a^{\dagger}_{i}, a_i$ denote fermionic creation and annihilation operators in an orbital basis, contains all information on k-fermion observables. We will be interested in electronic systems, where the interparticle interaction is Coulombic, and the Hamiltonian is thus of two-body form. In this case, the 2-RDM ${}^{2}P_{ik,jl} = \langle a^{\dagger}_{i} a^{\dagger}_{k} a_l a_j \rangle$ is of particular interest, as it determines the electronic energy [3, 4].

Because Ψ can be quite complicated in a correlated electronic state, obtaining an accurate k-RDM can be expensive. Here we discuss how to obtain improved approximations to the k-RDM (specifically, the 2-RDM ${}^{2}P$, although the procedures are general) from incomplete information on its elements. We consider two types of incomplete information. The first is a noiseless setting where we have only computed a subset of the RDM elements. This situation is relevant to deterministic algorithms (or stochastic algorithms in a setting where the statistical noise is very small) when obtaining the full k-RDM is expensive. The second is a noisy setting, where the goal is to reduce the total number of measurements. Such a noisy setting arises in both quantum Monte Carlo algorithms (as a statistical noise) [5–13] and in quantum simulations (as a measurement shot noise) [14–22]. In the latter case, measurement reduction [23–47] is especially relevant to hybrid quantum-classical algorithms [26, 43, 48–65] which rely on feedback from measured quantities. The quantum shot noise will be the specific noise setting considered in this work.

Various advanced estimators have been developed to reconstruct states and processes from tomographically incomplete measurements, including the maximum-likelihood estimator [66, 67], the maximum-entropy estimator [68, 69], N-representability-enforcing estimators [70, 71], basis adaptive measurements [72, 73], and symmetry projected measurements [74]. Here we will use the property that, in many applications, the RDMs are of low-rank [75–77]. Viewing the RDM as a matrix, we can then use its low-rank structure to both remove noise and/or fill in missing entries. This is a type of matrix completion or compressed sensing [78–87], and in the case where all elements are available with statistical errors, a version of low-rank noise filtering [88–94]. Similar matrix completion ideas have been used in quantum state tomography to treat n-qubit (reduced) density matrices [95–105]. Here we focus instead on the k-fermionic RDMs, and the specific matrix completion heuristics applicable to an electronic structure setting.

Low-rank matrix completion algorithms rely on a number of input parameters. We first define how such input parameters, such as the target rank, sampling method, incoherent basis, etc. can be determined in an electronic structure setting. We further introduce simple postprocessing (or error mitigation) techniques to improve the results of the completion. We then analyze noiseless and noisy matrix completion using a testbed of molecules from a subset of the G2 dataset [106]. In general, we find that with an optimized completion protocol, it is possible to reduce the measurement cost, either with respect to the number of elements or with respect to the number of shots, by 1-3 orders of magnitude across our dataset, while retaining a relevant accuracy to chemistry.

4.3 Theory

Recap of matrix completion and low-rank noise filtering

We briefly recall some relevant aspects of matrix completion. For a more detailed introduction, we refer to Refs. [79, 82, 107]. We restrict ourselves to square symmetric positive semi-definite matrices. The objective is to recover an approximation to a low-rank $d \times d$ matrix M from incomplete information about its elements. We first consider the case where we can measure the elements exactly (i.e. without noise) and the incompleteness is from measuring a subset of the elements Ω. Then, given $|\Omega| \equiv N_{\text{sample}}$ elements of matrix M, we can solve for a positive low-rank approximation M^r through the minimization:

$$\min_{\tilde{M}^r} \sum_{ij\in\Omega} (\tilde{M}^r_{ij} - M_{ij})^2, \text{ s.t. } \operatorname{rank}(\tilde{M}^r) = r, \tilde{M}^r \succcurlyeq 0, \tag{4.2}$$

where $\tilde{M}^r$ is the desired low-rank completion. Because we restrict to square symmetric positive definite M, we can use the parametrization $\tilde{M}^r = L^\dagger L$ where L is a real $r \times d$ matrix, and then perform minimization over L by gradient-based techniques.

The efficiency of the above matrix completion can be discussed in terms of the fraction of sampled elements $f_{\text{sample}} = N_{\text{sample}}/d^2$ required to obtain a given distance between $\tilde{M}^r$ and M, such as the relative error (in the Frobenius norm)

$$\epsilon(\tilde{M}^r, M) = \frac{||\tilde{M}^r - M||_F}{||M||}. \tag{4.3}$$

The efficiency clearly depends on the sampling scheme (i.e. the elements in Ω) and how information about the matrix is distributed in its entries (the matrix coherence). Assuming a random sampling scheme, successful matrix completion requires information to be spread over all matrix elements. For example, a matrix with only one nonzero element can only be completed correctly if the nonzero element is sampled. The distribution of such nonzero information can be quantified by the coherence in terms of the singular vectors of M [79, 107]: for $M = U\Lambda U^T$ with U a $d \times r$ matrix, we define the geometric coherence μ as

$$\mu = \frac{d}{r} \max_{1 \leq i \leq d} \|e_i^T U\|^2 \tag{4.4}$$

where $e_i \in \mathbb{R}^n$ is the standard basis. If all elements of U have magnitude $1/\sqrt{d}$, this yields the minimum coherence $\mu = 1$, while if the columns of U align with the standard basis, we obtain a maximum coherence $\mu = d/r$. The number of elements required to complete the matrix successfully can be shown to increase linearly with the coherence as $O(\mu r d \operatorname{poly}(\log d))$ [79, 107].

In our application, we require two generalizations of the above matrix completion. The first is that M is only approximately low rank, i.e. there are r singular values above some threshold, but also singular values below this threshold. Given some assumed rank r in the matrix completion, we can expect the best recoverable matrix to be $M^r = U\Lambda^r U^T$ (where Λ^r contains the r largest singular values) and there is a remaining rank truncation error $\sum_{i>r} \Lambda_i^2$ where Λ_i are the singular values in decreasing order. The best choice of rank r is not known ahead of time. We thus discuss how r can be estimated below using an independent approximate model of M.

The second generalization is that we consider matrix completion in the presence of noise. The statistical noise decreases as we increase the number of measurement shots m like $1/\sqrt{m}$. The efficiency of matrix completion can be assessed as $f_m = m/m_0$ where m_0 is the number of shots required in some standard measurement scheme to achieve a given error in M. Matrix completion is a useful technique in this context because statistical noise does not have a low-rank structure. Thus, if the noise is not too large, performing low-rank matrix completion filters out the noise. There are thus two potential gains in noisy matrix completion: one from measuring fewer distinct elements of the matrix, and one from requiring fewer shots to reduce the noise.

The fermionic 2-RDM

The fermionic 2-RDM, which we label P for simplicity, determines the electronic energy of the system. Given $P_{ik,jl}$, we obtain the 1-RDM

$$D_{ij} = \sum_{kl} P_{ik,jl}\delta_{kl}/(N_{\mathrm{el}} - 1) \tag{4.5}$$

where $N_{\mathrm{el}} = \mathrm{Tr}D$ is the number of electrons. The electronic energy is then

$$E[P] = \sum_{ij} t_{ij}D_{ij} + \frac{1}{2}\sum_{ijkl} V_{ikjl}P_{ik,jl} \tag{4.6}$$

where t_{ij} and V_{ikjl} are the one- and two-electron integrals, respectively. We denote the size of the orbital basis by n. We will refer to the two-electron part of the energy as $E_2[P]$.

The 2-RDM has a number of symmetries. In a real-orbital basis, the 2-RDM has an 8-fold symmetry

$$\begin{aligned} P_{ik,jl} &= P_{jl,ik} = -P_{ki,jl} = -P_{ik,lj} \\ &= -P_{lj,ik} = -P_{jl,ki} = P_{ki,lj} = P_{lj,ki} \end{aligned} \tag{4.7}$$

Further, if S_z is a good quantum number, and $i\sigma, j\sigma, k\sigma, l\sigma$ label α, β spin orbitals, P has only 3 unique non-zero spin sectors: $P^{\alpha\alpha\alpha\alpha}_{ik,jl}$, $P^{\beta\beta\beta\beta}_{ik,jl}$, and $P^{\alpha\beta\alpha\beta}_{ik,jl}$. If $S_z = 0$, then we further have $P^{\alpha\alpha\alpha\alpha}_{ik,jl} = P^{\beta\beta\beta\beta}_{ik,jl}$. $P^{\alpha\alpha\alpha\alpha}_{ik,jl}$, $P^{\beta\beta\beta\beta}_{ik,jl}$ have 8-fold symmetry, thus it is sufficient to consider symmetric matrices $P^{\sigma\sigma\sigma\sigma}_{i>k,j>l}$ of dimension $d \times d$ where $d = n(n+1)/2$ and n is the number of spatial orbitals. $P^{\alpha\beta\alpha\beta}_{ik,jl}$ has only 2-fold symmetry $P_{ik,jl} = P_{jl,ik}$ and is thus represented by a $d \times d$ symmetric matrix with $d = n^2$. We will only sample or measure unique elements (e.g. only the lower triangular part of P), and non-zero spin sectors, in our completion tests below, although for simplicity, we will refer to all spin sectors collectively as P.

The maximum rank r is d. For orientation, if one assumes the Hartree-Fock density matrix, where

$$P_{ik,jl} = D_{ij}D_{kl} - D_{il}D_{kj} \tag{4.8}$$

and D is idempotent, then $r(P^{\sigma\sigma\sigma\sigma}_{ik,jl}) = N_\sigma(N_\sigma - 1)/2$ and $r(P^{\alpha\beta\alpha\beta}_{ik,jl}) = N_\alpha N_\beta$ where N_α and N_β are the number of spin-up and spin-down electrons, respectively. These are the minimum ranks for an electronic system: if there are electron correlations, the rank of the 2-RDM increases. In Fig. 4.1, we show the singular values of the spin-components of P for two models of electron correlation: coupled cluster singles and doubles (CCSD) and second-order Møller Plesset perturbation theory (MP2) [108–110]. In both models, the singular value spectrum contains large singular values, corresponding to the Hartree-Fock piece of the 2-RDM. Beyond these, the singular values decay approximately exponentially [111].

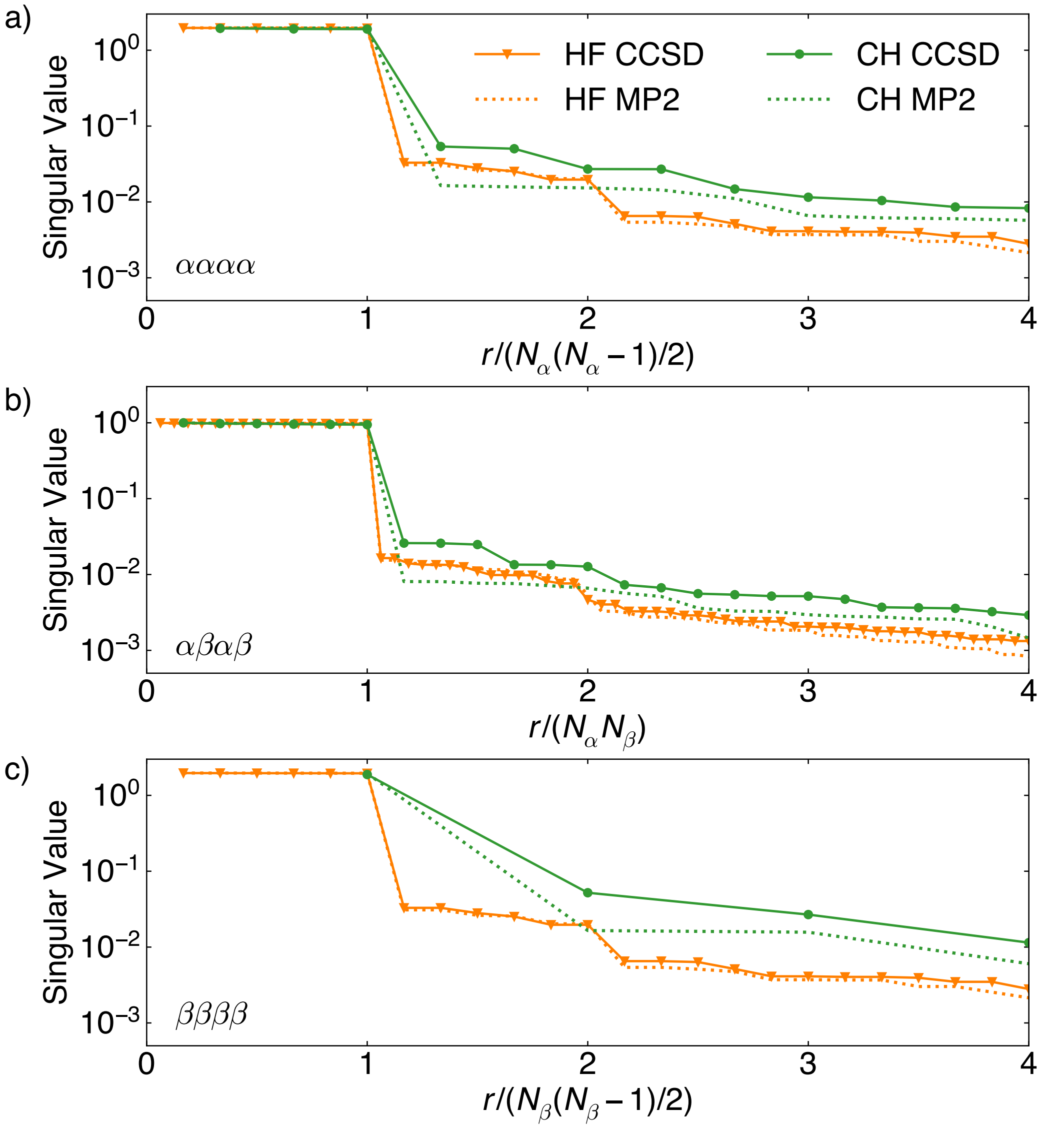

Figure 4.1: Singular values of the a) $P^{\alpha\alpha\alpha\alpha}$, b) $P^{\alpha\beta\alpha\beta}$, and c) $P^{\beta\beta\beta\beta}$ sectors of the (unrestricted) CCSD (solid) and MP2 (dash) 2-RDMs of the HF and CH molecules in the cc-pVDZ basis. The x-axis is the rank r divided by the rank of the corresponding Hartree-Fock 2-RDM.

Noiseless completion of the 2-RDM

We first consider the noiseless completion of the 2-RDM, where we have an incomplete sampling of the elements. To define the minimization problem in Eq. 4.2 concretely, as described in Sec. 4.3, we must specify (i) how to sample the elements,(ii) the estimated matrix rank r, and (iii) the number of elements to sample.

While there are procedures to estimate the approximation rank r on the fly [112, 113], here we use a simpler process that is likely available in many applications. Recall that we wish to use matrix completion in a setting where obtaining the elements of P is expensive. We can determine a less accurate model 2-RDM P_M via a cheaper procedure, and use the model to determine the optimal sampling, choice of rank r, and the number of elements to sample. We define the rank r model approximation $P_M^r = U\Lambda^r U^\dagger$ and choose r such that

$$\epsilon(P_M^r, P_M) < \kappa\epsilon_0 \tag{4.9}$$

where ϵ_0 is our target completion error, and κ is an empirical constant to account for the fact that our final error includes not only the rank truncation error arising from Eq. 4.9 but also a completion error from incomplete sampling. Here we use $\kappa = 1/2$.

Next, we consider the element sampling. Since we have a model available, one might consider sampling elements in the descending order of magnitude of elements of P_M in a basis such as the canonical molecular orbital (MO) basis. However, for the smaller elements necessary to complete P to chemical accuracy in energy, we observe a significant difference between our model P_M and P. Thus, sampling in this order does not give a favorable completion efficiency. As a result, we instead use uniform random sampling of the elements, which is efficient if the matrix is not very coherent. To minimize the coherence of the 2-RDM, we optimize orthogonal matrices C such that the coherence of $[P'_M]_{pqrs} = \sum_{ijkl} C_{pi}C_{qk}[P_M]_{ikjl}C_{jr}C_{ls}$ is minimized. See 4.4 for practical implementation. Fig. 4.2 shows the reduction in the coherence of a model MP2 P_M after such orbital rotations.

To estimate f_{sample} (the fraction of elements to sample), we perform matrix completion on the model P_M for the specified rank r, and coherence optimized orbitals, and choose N_{sample} so $\epsilon(\tilde{P}_M^r, P_M) < \epsilon_0$. An example of such a model matrix completion is shown in Fig. 4.3. As the fraction of sampled elements increases, the completion error saturates at the rank truncation error. However, there is an unusual feature where the completion error rises near the theoretical information bound (the number

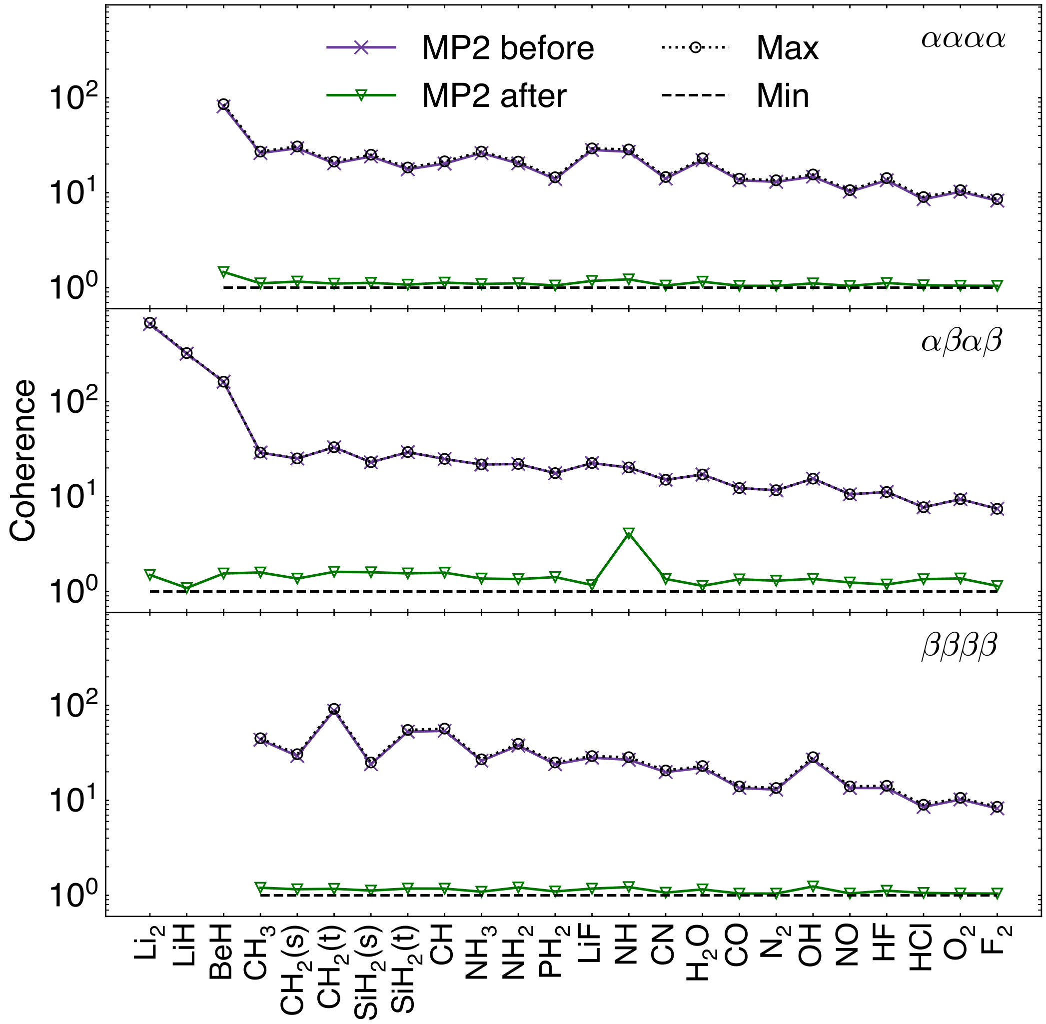

Figure 4.2: Coherence of the MP2 model 2-RDM in the cc-pVDZ basis. In the canonical MO basis, the coherence (purple) is close to the maximal coherence $\mu = d/r$ (black circle). After random orbital rotations, the coherence diminishes significantly, approaching the minimal coherence $\mu = 1$ (black dashed line). Note that after discarding the core orbitals (see main text) Li_2, LiH, and BeH only have a non-zero $P^{\alpha\beta\alpha\beta}$ sector.

of elements needed to exactly complete a symmetric matrix with the exact rank of r). This appears related to the approximate low-rank nature of P_M, and the non-trivial feature which is difficult to describe purely theoretically illustrates the value in having an explicit model P_M to determine the parameters of matrix completion.

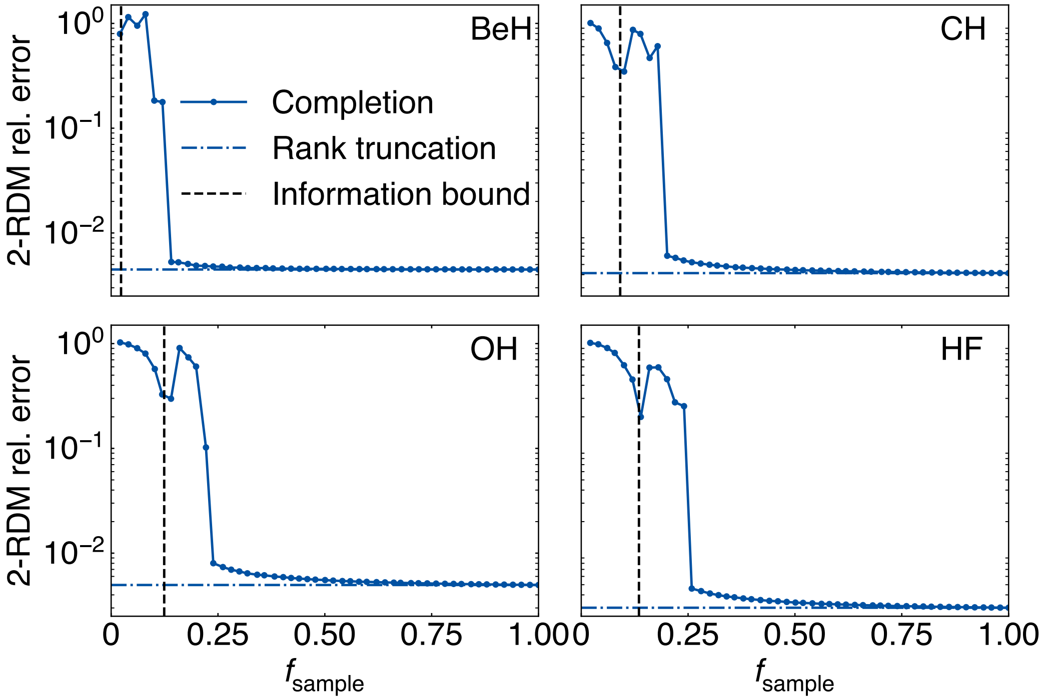

Figure 4.3: Completion errors of BeH, CH, OH and HF MP2 $P^{\alpha\alpha\alpha\alpha}$ RDMs in the cc-pVDZ basis as a function of the fraction of sampled elements f_{sample}. The completion rank is chosen according to Eq. 4.9. The theoretical information bound of $(2rd - r^2 + r)/(d(d+1))$ is the ratio of degrees of freedom in a rank-r symmetric $d \times d$ matrix to that of a rank-d symmetric matrix.

Measuring the 2-RDM in the quantum setting

We now consider the problem of measuring the 2-RDM with noise, which we will take to arise from quantum measurements. We choose a Jordan-Wigner encoding of fermions and assume we are measuring Pauli operators. The expectation value of strings of Pauli operators can then be converted to fermion expectation values. For a quartet of fermion labels i, j, k, l, the 3 fermion expectation values not related by permutational symmetry $\langle a_i^\dagger a_k^\dagger a_l a_j \rangle$, $\langle a_i^\dagger a_j^\dagger a_l a_k \rangle$, and $\langle a_i^\dagger a_l^\dagger a_j a_k \rangle$ are each determined from linear combinations of the expectation values of 8 Pauli strings

$$\begin{aligned}\langle a_i^\dagger a_k^\dagger a_l a_j\rangle, \langle a_i^\dagger a_j^\dagger a_l a_k\rangle, \langle a_i^\dagger a_l^\dagger a_j a_k\rangle \Leftrightarrow & \\ & \langle X_i \cdot X_k X_l \cdot X_j\rangle, \langle X_i \cdot X_k Y_l \cdot Y_j\rangle, \\ & \langle X_i \cdot Y_k X_l \cdot Y_j\rangle, \quad \langle X_i \cdot Y_k Y_l \cdot X_j\rangle, \\ & \langle Y_i \cdot X_k X_l \cdot Y_j\rangle, \quad \langle Y_i \cdot X_k Y_l \cdot X_j\rangle, \\ & \langle Y_i \cdot Y_k X_l \cdot X_j\rangle, \quad \langle Y_i \cdot Y_k Y_l \cdot Y_j\rangle,\end{aligned} \tag{4.10}$$

where $\cdot$ indicates additional possible Z operators in between the i, j, k, l indices. (Certain simplifications arise if any of the fermion indices i, j, k, l are the same; we can reconstruct such fermion expectation values using Pauli strings containing Z operators. We use such simplifications in our implementation and counting below.

Because the quantum state is not in a simultaneous eigenstate of all the measured operators, there will be statistical errors in (some of) the measurements. Although there exist a variety of techniques to minimize the number of measurement settings by grouping simultaneously measurable operators [27, 30, 32], we use the straightforward approach of independently measuring each Pauli string and leave potential improvement by grouping to future work. Thus we sample fermionic terms in sets of 3 in Eq. 4.10, each set associated with a i, j, k, l quartet and reconstructed from the same 8 Pauli strings. The measurement variance for the Pauli string Q is then obtained from the binomial distribution as $\sigma^2 = (1 + \langle Q\rangle)(1 - \langle Q\rangle)/m_{\mathrm{Q}}$ where m_{Q} is the number of measurements of the string.

To define the efficiency of matrix completion, we first need to define a "standard" measurement procedure, where no matrix completion is performed. In this scheme, all Pauli strings required for the fermionic 2-RDM are measured with the same number of shots yielding a noisy $\tilde{P}$. To estimate the total number of shots m required, we measure P in the coherence minimized orbital basis, and choose m such that $\epsilon(\tilde{P}, P) < \epsilon_0$. While in experiment more coherent basis might be used, in our tests, coherence minimization does not appreciably change the m required when no matrix completion is used, as illustrated on the model P_M in Fig. 4.4.

Noisy completion of the 2-RDM

We now discuss matrix completion when measurements include statistical errors. Given our model P_M, we use the same rank estimation procedure and coherence minimization procedure as in the noiseless setting. However, we need a differ-

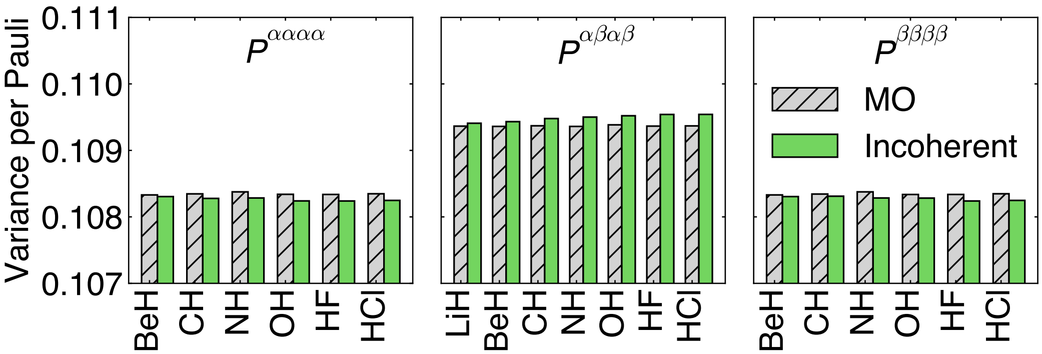

Figure 4.4: Average variance per Pauli string of MP2 2-RDMs in the aug-cc-pVDZ basis from a quantum measurement where each Pauli term is measured with 1 shot. The gray bars labeled "MO" denote measurements in the canonical MOs; the green bars labeled "incoherent" denote measurements in the coherence minimized orbital basis.

ent procedure to determine the number of (sets of) fermionic elements N_{sample} to measure, as the actual cost we wish to optimize is related to the total number of measurement shots m. For simplicity, we assume each Pauli string is being measured with the same number of shots. For a given m we should then search over N_{sample} to find the number of fermionic elements to measure that complete P_M with the lowest completion error; we then increase m until the completion error is below ϵ_0.

In Fig. 4.5 we illustrate a typical result from searching for the optimal N_{sample}. We see that in this problem, for a given m ($c = 0$ line) it is in fact optimal to sample close to 100% of the elements. This means matrix completion is performing almost entirely as a low-rank noise filter. In the other lines, we illustrate how the cost balance changes if we introduce a cost to switch the measurement setting when changing the Pauli strings (in multiples of the measurement cost, $c = 500, 10000$ data; $c = 500$ corresponds to the reported cost to switch measurements for the Sycamore quantum processor [114]). For a very high measurement setting cost, e.g. the case of $c = 10000$, there is a benefit to sample fewer elements. However, in the subsequent calculations, we will neglect the cost of measurement switching and determine the best m, f_{sample} pair assuming $c = 0$.

Post-processing the completed 2-RDM

We can improve the results of matrix completion and noise filtering through post-processing. In the noisy quantum setting, this can be viewed as a form of error mitigation. We perform the following steps:

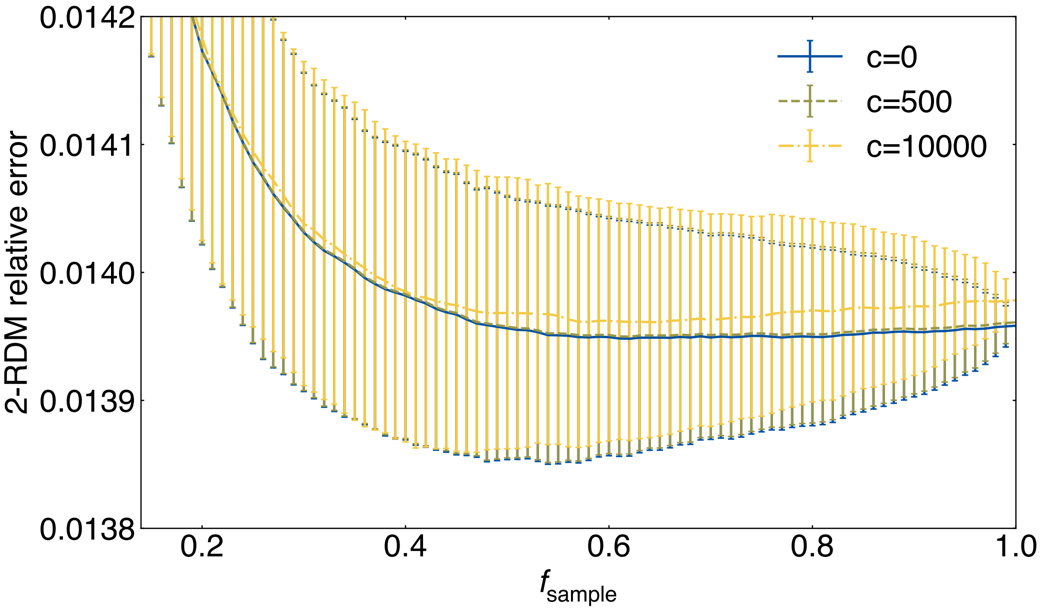

Figure 4.5: Completion errors of BeH CCSD $P^{\alpha\alpha\alpha\alpha}$ in the aug-cc-pVDZ basis in three settings, each with a different cost c to switch the measurement, for a fixed number of shots per element (1317636). The completion error at each f_{sample} is averaged over errors from 1000 different random samplings and the standard deviation is taken as the error bar.

1. For noiseless completion, we replace sampled terms in the completed 2-RDMs with their exact values (i.e. giving zero completion error on the sampled terms).
2. We normalize P (for the 3 spin components separately).
3. For noiseless completion, we apply matrix completion to obtain $\tilde{P}^r_M$, and the 2-RDM error of the model $P_M - \tilde{P}^r_M$ is added to our completed $\tilde{P}^r$.

Note this means that the *only* postprocessing done in the case of noisy completion is the normalization of the density matrix.

4.4 Computational details

We use 24 small molecular systems from the G2-1 test set [106], including both singlet (s) and triplet (t) states of CH_2 and SiH_2 and 20 other molecules (that include both open-shell radicals and closed-shell systems) in their lowest spin state for our noiseless completion studies, and a further subset of the 7 smallest ones to study the basis dependence of noiseless completion and for the noisy completion studies. (The 7 smallest molecules serve as representative examples for the larger set, encompassing both those with the smallest and largest cost reductions in the noiseless completion results). We used (aug-)cc-pVXZ bases [115–117] throughout and in CCSD and MP2 calculations froze the lowest energy orbitals ($1s$ for first row, $1s2s2p$ for second row). Completion is thus only performed for the non-core part of P. Molecular geometries at the B3LYP/6-31G($2df, p$) [118–120] level of theory were taken from Ref. [121, 122]. We computed unrestricted CCSD density matrices, as the reference "exact" density matrices. We computed unrelaxed unrestricted MP2 density matrices as the model density matrices. (We note that MP2 represents one of the simplest correlated density matrices for this purpose. For strongly multireference problems, other models may be preferable).

For our completion studies, we used a target completion error of $\epsilon_0 = 1\%$. Minimizing the geometric coherence corresponds to minimizing

$$\max_{p,q} \sum_s (C_{pi} C_{qk} U_{ik,s})^2 \tag{4.11}$$

where $U_{ik,s}$ are the singular vectors of $[P^r_M]_{ik,jl}$ and C is the basis rotation matrix to be optimized. However, this minimization is numerically inconvenient because the max function is not differentiable everywhere. Instead, we perform the minimization

$$\arg\min_{C} \sum_{p,q} \left(\sum_s (C_{pi} C_{qk} U_{ik,s})^2 \right)^4 \tag{4.12}$$

starting from 10 Haar random [123] initial guesses of orthogonal matrices C. In the noiseless matrix completion, for the MP2 P_M, we randomly generated 10 different element samplings for each f_{sample}, and for each sampling, used a maximum of 15000 iterations in the matrix completion optimization with the L-BFGS-B algorithm [124, 125]. f_{sample} was chosen so that $\epsilon \leq \epsilon_0$ in no less than 90% of the model completions. The CCSD 2-RDM completion was carried out using the same 10 element samplings as for MP2 2-RDMs. The CCSD completion errors were then averaged over all 10 trials except for cases where the optimization was not converged. In the noisy measurement setting, 10 random samplings were generated for each f_{sample} to estimate the best m, f_{sample} pair.

All quantum chemistry calculations were carried out with PySCF [126, 127], while the conversion of the fermionic operators to Jordan-Wigner form was carried out using the OpenFermion package and the OpenFermion-PySCF plugin [126, 128]. The Jordan-Wigner transformations were carried out on the 2-RDM in the coherence minimized basis.

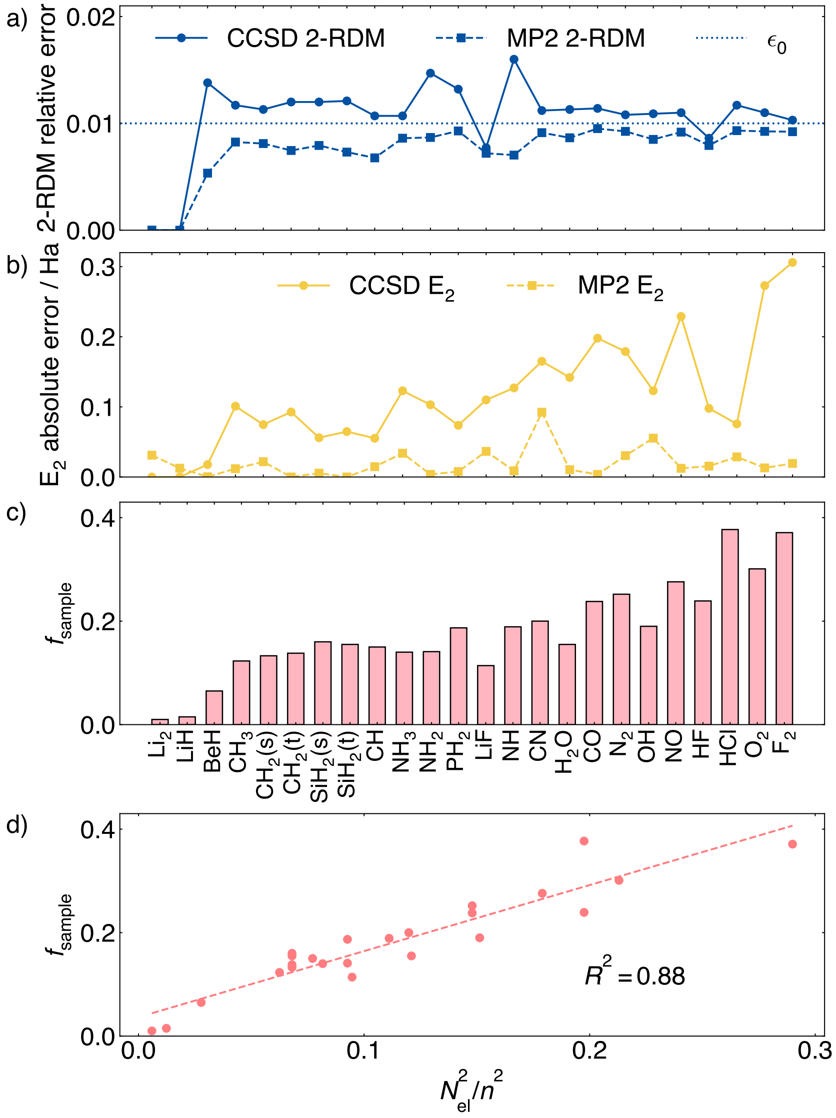

Figure 4.6: **a)** Using MP2 model P_M to complete the CCSD 2-RDM. A target completion error $\epsilon_0 = 1\%$ for P_M achieves $\epsilon \approx 1\%$ in the completed CCSD 2-RDM. **b)** The absolute error in the two-particle energy E_2 from completed 2-RDMs. **c)** Fraction of fermionic terms sampled f_{sample} used to complete 2-RDMs to the accuracy in **a**). **d)** f_{sample} is roughly proportional to $(N_{\text{el}}/n)^2$.

4.5 Results

Noiseless completion

Fig. 4.6a shows the completion results for $\epsilon_0 = 1\%$ for 2-RDMs in the cc-pVDZ basis for the 24 systems, showing both the 2-RDM error and two-particle energy (E_2, for the non-core part of P) error for the target 2-RDMs from CCSD, as well as the 2-RDM and two-particle energy error for the MP2 model 2-RDMs. For the MP2 model quantities, $\epsilon < 1\%$, by design. (We note that LiH and Li_2 have anomalously

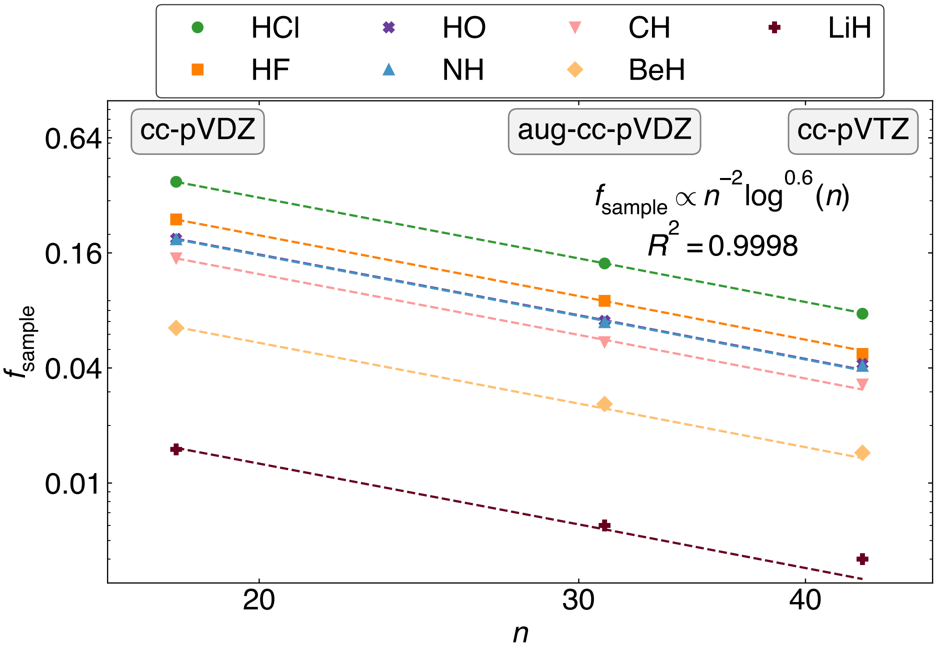

Figure 4.7: Fraction of elements sampled f_{sample} ($\epsilon_0 = 1\%$) as a function of basis size for a set of 7 molecules.

small errors because their RDMs are approximately rank-1). Across the series of molecules, this translates to approximately 0.02 Ha error in the MP2 two-particle energy.

The error of the MP2 model translates to the observed errors in the target CCSD 2-RDM matrix completion, with $\epsilon \leq 1.5\%$. The CCSD two-particle energy error is somewhat larger and grows from left to right in the plot. The molecules in the plot are ordered in terms of increasing N_{el}/n. For molecules such as BeH, where there is a significant difference between the singular value of the MP2 model and CCSD (reflecting the stronger correlation described by CCSD), the main reason for the increased CCSD completion error comes from the increased rank truncation error. For such systems where MP2 yields a relatively poor approximation, alternative models may be used. In Fig. 4.6c, we see that f_{sample} is roughly proportional to $(N_{\text{el}}/n)^2$. This comes from the rank of the Hartree-Fock 2-RDM as discussed in section 4.3.

The above suggests that matrix completion is more useful in larger basis sets. We test this in the subset of 7 molecules in Fig. 4.7. To achieve 1% completion error in the model MP2 2-RDM, we find that the fraction of samples needed decreases with basis size as $\sim 1/n^2 \log^{0.6}(n)$. To understand this trend, we note that the numerical rank for a fixed precision and system varies only slightly with basis, and thus the relative rank r/d decreases almost quadratically with the basis size. The smaller the relative rank, the larger the cost reduction from low-rank matrix completion. This trend falls between the fundamental information lower bound of $1/n^2$ [97, 129], below which P is underdetermined, and the best provable bound of $1/n^2 \log(n)$, which guarantees a high probability to complete P to a constant error [102].

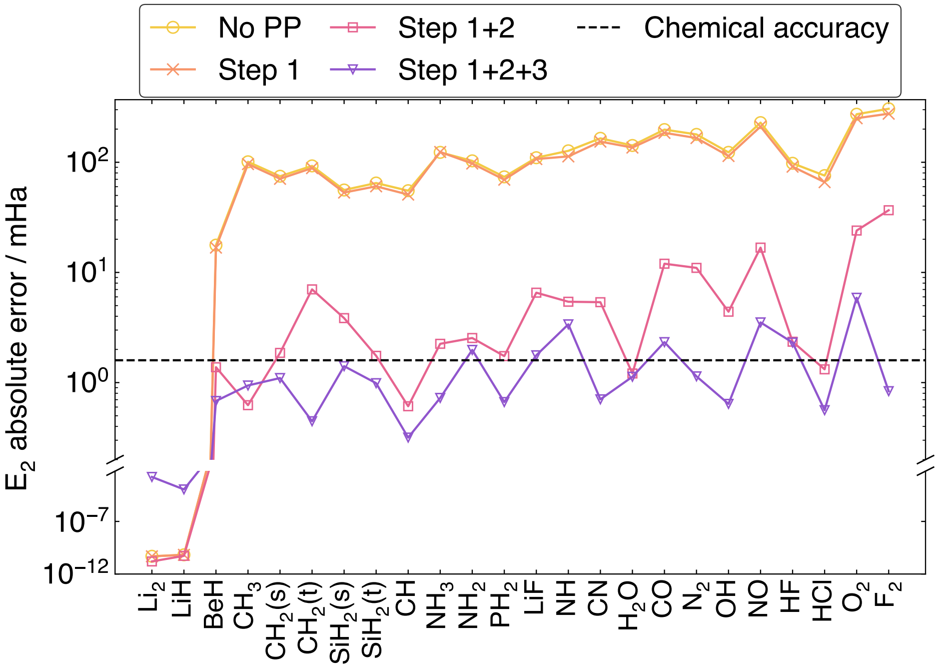

Figure 4.8: The effect on the two-particle energy E_2 of each post-processing option as defined in Sec. 4.3, for noiseless completion. Note that almost all the error reduction is achieved by normalization.

As expected, post-processing reduces the energy error of the completed target 2-RDMs. In Fig. 4.8 we show the effect of the different steps on the two-particle energy E_2. Out of the 3 post-processing steps, normalizing the trace of P reduces the error the most, by 1-2 orders of magnitude. This suggests that the majority of energy error comes from the low-rank approximation, i.e. from truncating small eigenvalues, which reduces the trace of P. After all post-processing steps, the two-particle energy errors are around chemical accuracy (1.6 mHa).

Noisy 2-RDM completion

We now carry out similar numerical experiments in the presence of measurement noise. In Fig. 4.9a, we report the average number of shots (i.e. number of shots divided by the number of unique elements of P, denoted $\bar{m}$) in the standard mea-

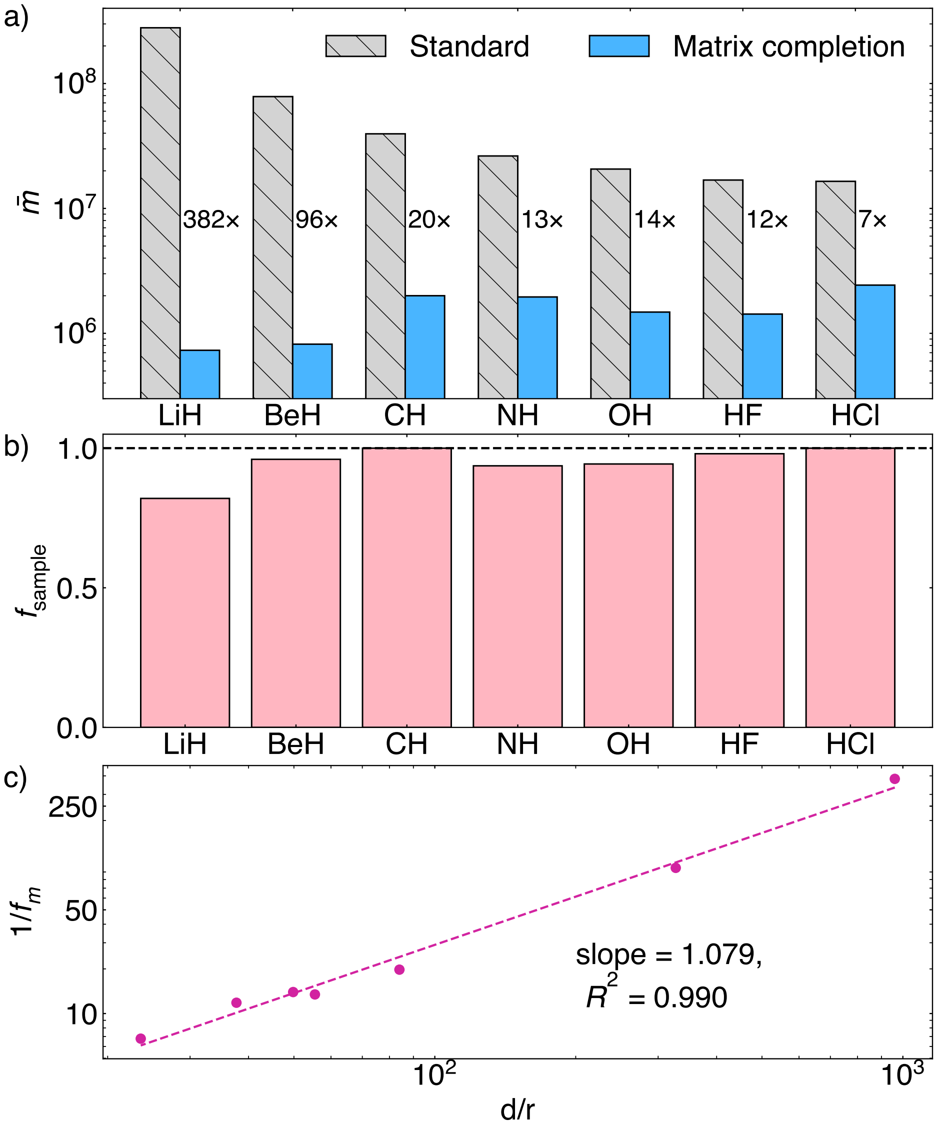

Figure 4.9: **a)** The average number of shots per unique Pauli term $\bar{m}$ for 7 molecules needed in the "standard" measurement scheme and when using "matrix completion." Their ratio $1/f_m$, i.e., the factor of measurement cost reduction, is reported next to the bars. **b)** Fraction of fermionic terms sampled f_{sample} used in **a)** "matrix completion." **c)** The measurement cost reduction, $1/f_m$, is proportional to d/r, where r is the MP2 rank estimate used in matrix completion. (d and r are averaged over the 3 spin sectors).

surement scheme and the average number of shots in the matrix completion scheme required to obtain $\epsilon_0 = 1\%$ for the subset of 7 molecules in the aug-cc-pVDZ basis. We see that across all molecules, there is a significant reduction $(1/f_m)$ in the average number of shots required compared to the standard measurement scheme; the total reduction is between 1 to 3 orders of magnitude in the aug-cc-pVDZ basis. For matrix completion, the associated f_{sample} used to generate the matrix completion data in Fig. 4.9a is reported in Fig. 4.9b. Almost all terms are measured for all the molecules, consistent with Fig. 4.5. Thus, resource reduction primarily comes from filtering the statistical noise in the measurements. In Fig. 4.9c we show the observed measurement cost reduction $1/f_m$ to complete to 1% accuracy as a function of the estimated rank of P_M. We find $f_m \sim r/d$ (the relative rank of the 2-RDM), which, when rescaled for $||P|| \sim r$, matches theoretical sample complexities of low-rank completions performed on normalized density matrices $||\bar{P}|| = 1$ [97, 102]. Therefore, resource reduction due to high-rank noise filtering is closely related to the low-rank property of the 2-RDM.

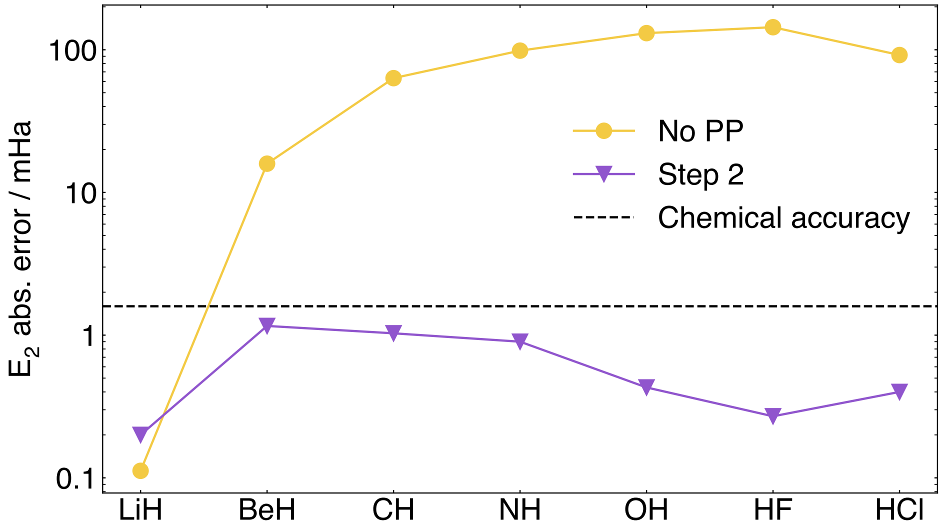

Figure 4.10: Absolute energy error from the completed 2-RDM before and after step 2 (trace normalization) of post-processing (PP). After post-processing, the two-particle energy error is within chemical accuracy (1.6 mHa).

In Fig. 4.10, we show the energy error and 2-RDM error before and after normalizing P to the correct number of electrons. After this post-processing, the energy errors are all within chemical accuracy.

4.6 Conclusions

We have demonstrated that matrix completions can effectively reduce the effort to obtain fermionic k-RDMs of interest in electronic structure, and in particular, the 2-RDM. This was achieved by exploiting the low-rank structure as well as information obtained from approximate models of the 2-RDM. After a simple postprocessing step (normalizing the density matrix) we can reach chemical accuracy, with multiple orders of magnitude reduction in measurement cost.

The current work has immediate applications in both classical and quantum algorithms to obtain 2-RDMs. In the classical setting, we envision that these techniques can easily be employed in quantum Monte Carlo simulations. In the hybrid quantum algorithm setting, there exist other techniques to reduce the measurement resources, such as optimizing the groups of qubit-wise commuting Pauli terms [30, 32], or employing classical shadows [27, 29]. It is likely these methods can be employed in conjunction with the matrix completion technique. In addition, it will be interesting to explore analogs of matrix completion that use the tensor structure of the 2-RDM [130] or to impose additional constraints, such as N-representability conditions [70, 131, 132].

References

1. Löwdin, P.-O. Quantum theory of many-particle systems. I. Physical interpretations by means of density matrices, natural spin-orbitals, and convergence problems in the method of configurational interaction. *Physical Review* **97,** 1474. doi:`10.1103/PhysRev.97.1474` (1955).

2. Davidson, E. *Reduced density matrices in quantum chemistry* (Elsevier, 2012).

3. Coulson, C. A. Present state of molecular structure calculations. *Reviews of Modern Physics* **32,** 170. doi:`10.1103/RevModPhys.32.170` (1960).

4. Mazziotti, D. A. *Reduced-density-matrix mechanics: with applications to many-electron atoms and molecules* doi:`10.1002/0470106603` (Wiley Online Library, 2007).

5. Hammond, B. L., Lester, W. A. & Reynolds, P. J. *Monte Carlo methods in ab initio quantum chemistry* doi:`10.1142/9789814317245_0001` (World Scientific, 1994).

6. Nightingale, M. P. & Umrigar, C. J. *Quantum Monte Carlo methods in physics and chemistry* **525** (Springer Science & Business Media, 1998).

7. Foulkes, W., Mitas, L., Needs, R. & Rajagopal, G. Quantum Monte Carlo simulations of solids. *Reviews of Modern Physics* **73,** 33. doi:`10.1103/RevModPhys.73.33` (2001).

8. Zhang, S. 15 Auxiliary-Field Quantum Monte Carlo for Correlated Electron Systems. *Emergent Phenomena in Correlated Matter* (2013).

9. Austin, B. M., Zubarev, D. Y. & Lester Jr, W. A. Quantum Monte Carlo and related approaches. *Chemical Reviews* **112,** 263–288. doi:`10.1021/cr2001564` (2012).

10. Kent, P., Hood, R. Q., Towler, M., Needs, R. & Rajagopal, G. Quantum Monte Carlo calculations of the one-body density matrix and excitation energies of silicon. *Physical Review B* **57,** 15293. doi:`10.1103/PhysRevB.57.15293` (1998).

11. Blunt, N. S., Booth, G. H. & Alavi, A. Density matrices in full configuration interaction quantum Monte Carlo: Excited states, transition dipole moments, and parallel distribution. *The Journal of Chemical Physics* **146,** 244105. doi:`10.1063/1.4986963` (2017).

12. Booth, G. H., Cleland, D., Alavi, A. & Tew, D. P. An explicitly correlated approach to basis set incompleteness in full configuration interaction quantum Monte Carlo. *The Journal of Chemical Physics* **137,** 164112. doi:`10.1063/1.4762445` (2012).

13. Liu, Y., Cho, M. & Rubenstein, B. Ab initio finite temperature auxiliary field quantum Monte Carlo. *Journal of Chemical Theory and Computation* **14,** 4722–4732. doi:`10.1021/acs.jctc.8b00569` (2018).

14. Nielsen, M. A. & Chuang, I. *Quantum computation and quantum information* doi:`10.1017/CBO9780511976667` (Cambridge University Press, 2000).

15. Kitaev, A. Y. Quantum measurements and the Abelian stabilizer problem. *arXiv preprint quant-ph/9511026.* doi:`10.48550/arXiv.quant-ph/9511026` (1995).

16. Aspuru-Guzik, A., Dutoi, A. D., Love, P. J. & Head-Gordon, M. Simulated quantum computation of molecular energies. *Science* **309,** 1704–1707. doi:`10.1126/science.1113479` (2005).

17. Cruz, P. M., Catarina, G., Gautier, R. & Fernández-Rossier, J. Optimizing quantum phase estimation for the simulation of Hamiltonian eigenstates. *Quantum Science and Technology* **5,** 044005. doi:`10.1088/2058-9565/abaa2c` (2020).

18. Motta, M., Sun, C., Tan, A. T., O'Rourke, M. J., Ye, E., Minnich, A. J., Brandão, F. G. & Chan, G. K.-L. Determining eigenstates and thermal states on a quantum computer using quantum imaginary time evolution. *Nature Physics* **16,** 205–210. doi:`10.1038/s41567-019-0704-4` (2020).

19. Veis, L. & Pittner, J. Adiabatic state preparation study of methylene. *The Journal of Chemical Physics* **140,** 214111. doi:`10.1063/1.4880755` (2014).

20. Tilly, J., Sriluckshmy, P., Patel, A., Fontana, E., Rungger, I., Grant, E., Anderson, R., Tennyson, J. & Booth, G. H. Reduced density matrix sampling: Self-consistent embedding and multiscale electronic structure on current generation quantum computers. *Physical Review Research* **3,** 033230. doi:`10.1103/PhysRevResearch.3.033230` (2021).

21. Braunstein, S. L. & Caves, C. M. Statistical distance and the geometry of quantum states. *Physical Review Letters* **72,** 3439. doi:`10.1103/PhysRevLett.72.3439` (1994).

22. Pezze, L. & Smerzi, A. Quantum theory of phase estimation. *arXiv preprint arXiv:1411.5164.* doi:`10.48550/arXiv.1411.5164` (2014).

23. Babbush, R., Wiebe, N., McClean, J., McClain, J., Neven, H. & Chan, G. K.-L. Low-depth quantum simulation of materials. *Physical Review X* **8,** 011044. doi:`10.1103/PhysRevX.8.011044` (2018).

24. Wang, D., Higgott, O. & Brierley, S. Accelerated variational quantum eigensolver. *Physical Review Letters* **122,** 140504. doi:`10.1103/PhysRevLett.122.140504` (2019).

25. Zhao, A., Tranter, A., Kirby, W. M., Ung, S. F., Miyake, A. & Love, P. J. Measurement reduction in variational quantum algorithms. *Physical Review A* **101,** 062322. doi:`10.1103/PhysRevA.101.062322` (2020).

26. Rubin, N. C. A hybrid classical/quantum approach for large-scale studies of quantum systems with density matrix embedding theory. *arXiv preprint arXiv:1610.06910.* doi:`10.48550/arXiv.1610.06910` (2016).

27. Huang, H.-Y., Kueng, R. & Preskill, J. Predicting many properties of a quantum system from very few measurements. *Nature Physics* **16,** 1050–1057. doi:`10.1038/s41567-020-0932-7` (2020).

28. Huang, H.-Y., Kueng, R. & Preskill, J. Efficient estimation of pauli observables by derandomization. *Physical Review Letters* **127,** 030503. doi:`10.1103/PhysRevLett.127.030503` (2021).

29. Zhao, A., Rubin, N. C. & Miyake, A. Fermionic partial tomography via classical shadows. *Physical Review Letters* **127,** 110504. doi:`10.1103/PhysRevLett.127.110504` (2021).

30. Verteletskyi, V., Yen, T.-C. & Izmaylov, A. F. Measurement optimization in the variational quantum eigensolver using a minimum clique cover. *The Journal of Chemical Physics* **152,** 124114. doi:`10.1063/1.5141458` (2020).

31. Jena, A., Genin, S. & Mosca, M. Pauli partitioning with respect to gate sets. *arXiv preprint arXiv:1907.07859.* doi:`10.48550/arXiv.1907.07859` (2019).

32. Bonet-Monroig, X., Babbush, R. & O'Brien, T. E. Nearly optimal measurement scheduling for partial tomography of quantum states. *Physical Review X* **10,** 031064. doi:`10.1103/PhysRevX.10.031064` (2020).

33. Yen, T.-C., Verteletskyi, V. & Izmaylov, A. F. Measuring all compatible operators in one series of single-qubit measurements using unitary transformations. *Journal of Chemical Theory and Computation* **16,** 2400–2409. doi:`10.1021/acs.jctc.0c00008` (2020).

34. Hadfield, C., Bravyi, S., Raymond, R. & Mezzacapo, A. Measurements of quantum Hamiltonians with locally-biased classical shadows. *Communications in Mathematical Physics* **391,** 951–967. doi:`10.1007/s00220-022-04343-8` (2022).

35. Yen, T.-C., Ganeshram, A. & Izmaylov, A. F. Deterministic improvements of quantum measurements with grouping of compatible operators, non-local transformations, and covariance estimates. *npj Quantum Information* **9,** 14. doi:`10.1038/s41534-023-00683-y` (2023).

36. Wu, B., Sun, J., Huang, Q. & Yuan, X. Overlapped grouping measurement: A unified framework for measuring quantum states. *Quantum* **7,** 896. doi:`10.22331/q-2023-01-13-896` (2023).

37. Gokhale, P., Angiuli, O., Ding, Y., Gui, K., Tomesh, T., Suchara, M., Martonosi, M. & Chong, F. T. Minimizing state preparations in variational quantum eigensolver by partitioning into commuting families. *arXiv preprint arXiv:1907.13623.* doi:`10.48550/arXiv.1907.13623` (2019).

38. Izmaylov, A. F., Yen, T.-C., Lang, R. A. & Verteletskyi, V. Unitary partitioning approach to the measurement problem in the variational quantum eigensolver method. *Journal of Chemical Theory and Computation* **16,** 190–195. doi:`10.1021/acs.jctc.9b00791` (2019).

39. Gokhale, P., Angiuli, O., Ding, Y., Gui, K., Tomesh, T., Suchara, M., Martonosi, M. & Chong, F. T. $O(N^3)$ Measurement Cost for Variational Quantum Eigensolver on Molecular Hamiltonians. *IEEE Transactions on Quantum Engineering* **1,** 1–24. doi:`10.1109/TQE.2020.3035814` (2020).

40. Torlai, G., Mazzola, G., Carleo, G. & Mezzacapo, A. Precise measurement of quantum observables with neural-network estimators. *Physical Review Research* **2,** 022060. doi:`10.1103/PhysRevResearch.2.022060` (2020).

41. Crawford, O., van Straaten, B., Wang, D., Parks, T., Campbell, E. & Brierley, S. Efficient quantum measurement of Pauli operators in the presence of finite sampling error. *Quantum* **5,** 385. doi:`10.22331/q-2021-01-20-385` (2021).

42. Cotler, J. & Wilczek, F. Quantum overlapping tomography. *Physical Review Letters* **124,** 100401. doi:`10.1103/PhysRevLett.124.100401` (2020).

43. Quantum, G. A., Collaborators*†, Arute, F., Arya, K., Babbush, R., Bacon, D., Bardin, J. C., Barends, R., Boixo, S., Broughton, M., Buckley, B. B., *et al.* Hartree-Fock on a superconducting qubit quantum computer. *Science* **369,** 1084–1089. doi:`10.1126/science.abb9811` (2020).

44. Huggins, W. J., McClean, J. R., Rubin, N. C., Jiang, Z., Wiebe, N., Whaley, K. B. & Babbush, R. Efficient and noise resilient measurements for quantum chemistry on near-term quantum computers. *npj Quantum Information* **7,** 1–9. doi:`10.1038/s41534-020-00341-7` (2021).

45. Shlosberg, A., Jena, A. J., Mukhopadhyay, P., Haase, J. F., Leditzky, F. & Dellantonio, L. Adaptive estimation of quantum observables. *Quantum* **7,** 906. doi:`10.22331/q-2023-01-26-906` (2023).

46. Torlai, G., Mazzola, G., Carrasquilla, J., Troyer, M., Melko, R. & Carleo, G. Neural-network quantum state tomography. *Nature Physics* **14,** 447–450. doi:`10.1038/s41567-018-0048-5` (2018).

47. Lanyon, B., Maier, C., Holzäpfel, M., Baumgratz, T., Hempel, C., Jurcevic, P., Dhand, I., Buyskikh, A., Daley, A., Cramer, M., *et al.* Efficient tomography of a quantum many-body system. *Nature Physics* **13,** 1158–1162. doi:`10.1038/nphys4244` (2017).

48. Peruzzo, A., McClean, J., Shadbolt, P., Yung, M.-H., Zhou, X.-Q., Love, P. J., Aspuru-Guzik, A. & O'brien, J. L. A variational eigenvalue solver on a photonic quantum processor. *Nature Communications* **5,** 1–7. doi:`10.1038/ncomms5213` (2014).

49. Yung, M.-H., Casanova, J., Mezzacapo, A., Mcclean, J., Lamata, L., Aspuru-Guzik, A. & Solano, E. From transistor to trapped-ion computers for quantum chemistry. *Scientific Reports* **4,** 1–7. doi:`10.1038/srep03589` (2014).

50. Shen, Y., Zhang, X., Zhang, S., Zhang, J.-N., Yung, M.-H. & Kim, K. Quantum implementation of the unitary coupled cluster for simulating molecular electronic structure. *Physical Review A* **95,** 020501. doi:`10.1103/PhysRevA.95.020501` (2017).

51. McClean, J. R., Romero, J., Babbush, R. & Aspuru-Guzik, A. The theory of variational hybrid quantum-classical algorithms. *New Journal of Physics* **18,** 023023. doi:`10.1088/1367-2630/18/2/023023` (2016).

52. Romero, J., Babbush, R., McClean, J. R., Hempel, C., Love, P. J. & Aspuru-Guzik, A. Strategies for quantum computing molecular energies using the unitary coupled cluster ansatz. *Quantum Science and Technology* **4,** 014008. doi:`10.1088/2058-9565/aad3e4` (2018).

53. O'Malley, P. J., Babbush, R., Kivlichan, I. D., Romero, J., McClean, J. R., Barends, R., Kelly, J., Roushan, P., Tranter, A., Ding, N., *et al.* Scalable quantum simulation of molecular energies. *Physical Review X* **6,** 031007. doi:`10.1103/PhysRevX.6.031007` (2016).

54. Nam, Y., Chen, J.-S., Pisenti, N. C., Wright, K., Delaney, C., Maslov, D., Brown, K. R., Allen, S., Amini, J. M., Apisdorf, J., *et al.* Ground-state energy estimation of the water molecule on a trapped-ion quantum computer. *npj Quantum Information* **6,** 1–6. doi:`10.1038/s41534-020-0259-3` (2020).

55. McCaskey, A. J., Parks, Z. P., Jakowski, J., Moore, S. V., Morris, T. D., Humble, T. S. & Pooser, R. C. Quantum chemistry as a benchmark for near-term quantum computers. *npj Quantum Information* **5,** 1–8. doi:`10.1038/s41534-019-0209-0` (2019).

56. Motta, M., Gujarati, T. P., Rice, J. E., Kumar, A., Masteran, C., Latone, J. A., Lee, E., Valeev, E. F. & Takeshita, T. Y. Quantum simulation of electronic structure with a transcorrelated Hamiltonian: improved accuracy with a smaller footprint on the quantum computer. *Physical Chemistry Chemical Physics* **22,** 24270–24281. doi:`10.1039/D0CP04106H` (2020).

57. Takeshita, T., Rubin, N. C., Jiang, Z., Lee, E., Babbush, R. & McClean, J. R. Increasing the representation accuracy of quantum simulations of chemistry without extra quantum resources. *Physical Review X* **10,** 011004. doi:`10.1103/PhysRevX.10.011004` (2020).

58. Hempel, C., Maier, C., Romero, J., McClean, J., Monz, T., Shen, H., Jurcevic, P., Lanyon, B. P., Love, P., Babbush, R., *et al.* Quantum chemistry calculations on a trapped-ion quantum simulator. *Physical Review X* **8,** 031022. doi:`10.1103/PhysRevX.8.031022` (2018).

59. Gao, Q., Jones, G. O., Motta, M., Sugawara, M., Watanabe, H. C., Kobayashi, T., Watanabe, E., Ohnishi, Y.-y., Nakamura, H. & Yamamoto, N. Applications of quantum computing for investigations of electronic transitions in phenylsulfonyl-carbazole TADF emitters. *npj Computational Materials* **7,** 1–9. doi:`10.1038/s41524-021-00540-6` (2021).

60. Parrish, R. M., Hohenstein, E. G., McMahon, P. L. & Martínez, T. J. Quantum computation of electronic transitions using a variational quantum eigensolver. *Physical Review Letters* **122,** 230401. doi:`10.1103/PhysRevLett.122.230401` (2019).

61. Kandala, A., Mezzacapo, A., Temme, K., Takita, M., Brink, M., Chow, J. M. & Gambetta, J. M. Hardware-efficient variational quantum eigensolver for small molecules and quantum magnets. *Nature* **549,** 242–246. doi:`10.1038/nature23879` (2017).

62. Smart, S. E. & Mazziotti, D. A. Quantum solver of contracted eigenvalue equations for scalable molecular simulations on quantum computing devices. *Physical Review Letters* **126,** 070504. doi:`10.1103/PhysRevLett.126.070504` (2021).

63. Bauer, B., Wecker, D., Millis, A. J., Hastings, M. B. & Troyer, M. Hybrid quantum-classical approach to correlated materials. *Physical Review X* **6,** 031045. doi:`10.1103/PhysRevX.6.031045` (2016).

64. Kreula, J. M., García-Álvarez, L., Lamata, L., Clark, S. R., Solano, E. & Jaksch, D. Few-qubit quantum-classical simulation of strongly correlated lattice fermions. *EPJ Quantum Technology* **3,** 1–19. doi:`10.1140/epjqt/s40507-016-0049-1` (2016).

65. Yamazaki, T., Matsuura, S., Narimani, A., Saidmuradov, A. & Zaribafiyan, A. Towards the practical application of near-term quantum computers in quantum chemistry simulations: A problem decomposition approach. *arXiv preprint arXiv:1806.01305.* doi:`10.48550/arXiv.1806.01305` (2018).

66. Hradil, Z. Quantum-state estimation. *Physical Review A* **55,** R1561. doi:`10.1088/2058-9565/abaa2c` (1997).

67. Banaszek, K., D'ariano, G., Paris, M. & Sacchi, M. Maximum-likelihood estimation of the density matrix. *Physical Review A* **61,** 010304. doi:`10.1103/PhysRevA.61.010304` (1999).

68. Gupta, R., Xia, R., Levine, R. D. & Kais, S. Maximal entropy approach for quantum state tomography. *PRX Quantum* **2,** 010318. doi:`10.1103/PRXQuantum.2.010318` (2021).

69. Teo, Y. S., Zhu, H., Englert, B.-G., Řeháček, J. & Hradil, Z. Quantum-state reconstruction by maximizing likelihood and entropy. *Physical Review Letters* **107,** 020404. doi:`10.1103/PhysRevLett.107.020404` (2011).

70. Rubin, N. C., Babbush, R. & McClean, J. Application of fermionic marginal constraints to hybrid quantum algorithms. *New Journal of Physics* **20,** 053020. doi:`10.1088/1367-2630/aab919` (2018).

71. Foley IV, J. J. & Mazziotti, D. A. Measurement-driven reconstruction of many-particle quantum processes by semidefinite programming with application to photosynthetic light harvesting. *Physical Review A* **86,** 012512. doi:`10.1103/physreva.86.012512` (2012).

72. Teo, Y. S., Struchalin, G., Kovlakov, E., Ahn, D., Jeong, H., Straupe, S., Kulik, S., Leuchs, G. & Sánchez-Soto, L. L. Objective compressive quantum process tomography. *Physical Review A* **101,** 022334. doi:`10.1103/PhysRevA.101.022334` (2020).

73. Kim, Y., Teo, Y. S., Ahn, D., Im, D.-G., Cho, Y.-W., Leuchs, G., Sánchez-Soto, L. L., Jeong, H. & Kim, Y.-H. Universal compressive characterization of quantum dynamics. *Physical Review Letters* **124,** 210401. doi:`10.1103/PhysRevLett.124.210401` (2020).

74. Smart, S. E. & Mazziotti, D. A. Lowering tomography costs in quantum simulation with a symmetry projected operator basis. *Physical Review A* **103,** 012420. doi:`10.1103/PhysRevA.103.012420` (2021).

75. Schwerdtfeger, C. A. & Mazziotti, D. A. Low-rank spectral expansions of two electron excitations for the acceleration of quantum chemistry calculations. *The Journal of Chemical Physics* **137,** 244103. doi:`10.1063/1.4770278` (2012).

76. Gidofalvi, G. & Mazziotti, D. A. Multireference self-consistent-field energies without the many-electron wave function through a variational low-rank two-electron reduced-density-matrix method. *The Journal of Chemical Physics* **127,** 244105. doi:`10.1063/1.2817602` (2007).

77. Mazziotti, D. A. Enhanced constraints for accurate lower bounds on many-electron quantum energies from variational two-electron reduced density matrix theory. *Physical Review Letters* **117,** 153001. doi:`10.1103/PhysRevLett.117.153001` (2016).

78. Cai, J.-F., Candès, E. J. & Shen, Z. A singular value thresholding algorithm for matrix completion. *SIAM Journal on Optimization* **20,** 1956–1982. doi:`10.1137/080738970` (2010).

79. Candès, E. J. & Recht, B. Exact matrix completion via convex optimization. *Foundations of Computational Mathematics* **9,** 717–772. doi:`10.1007/s10208-009-9045-5` (2009).

80. Keshavan, R., Montanari, A. & Oh, S. Matrix completion from noisy entries. *Advances in Neural Information Processing Systems* **22** (2009).

81. Keshavan, R. H., Montanari, A. & Oh, S. Matrix completion from a few entries. *IEEE Transactions on Information Theory* **56,** 2980–2998. doi:`10.1109/TIT.2010.2046205` (2010).

82. Candes, E. J. & Plan, Y. Matrix completion with noise. *Proceedings of the IEEE* **98,** 925–936. doi:`10.1109/JPROC.2009.2035722` (2010).

83. Candes, E. J. & Plan, Y. Tight oracle inequalities for low-rank matrix recovery from a minimal number of noisy random measurements. *IEEE Transactions on Information Theory* **57,** 2342–2359. doi:`10.1109/TIT.2011.2111771` (2011).

84. Koltchinskii, V., Lounici, K. & Tsybakov, A. B. Nuclear-norm penalization and optimal rates for noisy low-rank matrix completion. *The Annals of Statistics* **39,** 2302–2329. doi:`10.1214/11-AOS894` (2011).

85. Negahban, S. & Wainwright, M. J. Restricted strong convexity and weighted matrix completion: Optimal bounds with noise. *The Journal of Machine Learning Research* **13,** 1665–1697 (2012).

86. Ge, R., Lee, J. D. & Ma, T. Matrix completion has no spurious local minimum. *Advances in Neural Information Processing Systems* **29.** doi:`10.48550/arXiv.1605.07272` (2016).

87. Ji, H., Liu, C., Shen, Z. & Xu, Y. *Robust video denoising using low rank matrix completion* in *2010 IEEE Computer Society Conference on Computer Vision and Pattern Recognition* (2010), 1791–1798. doi:`10.1109/CVPR.2010.5539849`.

88. Richards, J. A. & Richards, J. A. *Remote sensing digital image analysis* doi:`10.1007/978-3-030-82327-6` (Springer, 2022).

89. Wall, M. E., Rechtsteiner, A. & Rocha, L. M. Singular value decomposition and principal component analysis. *A Practical Approach to Microarray Data Analysis,* 91–109. doi:`10.1007/0-306-47815-3_5` (2003).

90. Gan, S., Chen, Y., Zu, S., Qu, S. & Zhong, W. Structure-oriented singular value decomposition for random noise attenuation of seismic data. *Journal of Geophysics and Engineering* **12,** 262–272. doi:`10.1088/1742-2132/12/2/262` (2015).

91. Paul, J. S., Reddy, M. R. & Kumar, V. J. A transform domain SVD filter for suppression of muscle noise artefacts in exercise ECG's. *IEEE Transactions on Biomedical Engineering* **47,** 654–663. doi:`10.1109/10.841337` (2000).

92. Kazama, M. & Tohyama, M. Estimation of speech components by ACF analysis in a noisy environment. *Journal of Sound and Vibration* **241,** 41–52. doi:`10.1006/jsvi.2000.3275` (2001).

93. Schanze, T. Compression and noise reduction of biomedical signals by singular value decomposition. *IFAC-PapersOnLine* **51,** 361–366. doi:`10.1016/j.ifacol.2018.03.062` (2018).

94. Konstantinides, K., Natarajan, B. & Yovanof, G. S. Noise estimation and filtering using block-based singular value decomposition. *IEEE Transactions on Image Processing* **6,** 479–483. doi:`10.1109/83.557359` (1997).

95. Gross, D., Liu, Y.-K., Flammia, S. T., Becker, S. & Eisert, J. Quantum state tomography via compressed sensing. *Physical Review Letters* **105,** 150401. doi:`10.1103/PhysRevLett.105.150401` (2010).

96. Gross, D. Recovering low-rank matrices from few coefficients in any basis. *IEEE Transactions on Information Theory* **57,** 1548–1566. doi:`10.1109/TIT.2011.2104999` (2011).

97. Flammia, S. T., Gross, D., Liu, Y.-K. & Eisert, J. Quantum tomography via compressed sensing: error bounds, sample complexity and efficient estimators. *New Journal of Physics* **14,** 095022. doi:`10.1088/1367-2630/14/9/095022` (2012).

98. Kalev, A., Kosut, R. L. & Deutsch, I. H. Quantum tomography protocols with positivity are compressed sensing protocols. *npj Quantum Information* **1,** 1–6. doi:`10.1038/npjqi.2015.18` (2015).

99. Riofrio, C. A., Gross, D., Flammia, S. T., Monz, T., Nigg, D., Blatt, R. & Eisert, J. Experimental quantum compressed sensing for a seven-qubit system. *Nature Communications* **8,** 1–8. doi:`10.1038/ncomms15305` (2017).

100. Cramer, M., Plenio, M. B., Flammia, S. T., Somma, R., Gross, D., Bartlett, S. D., Landon-Cardinal, O., Poulin, D. & Liu, Y.-K. Efficient quantum state tomography. *Nature Communications* **1,** 1–7. doi:`10.1038/ncomms1147` (2010).

101. Steffens, A., Riofrío, C., McCutcheon, W., Roth, I., Bell, B. A., McMillan, A., Tame, M., Rarity, J. & Eisert, J. Experimentally exploring compressed sensing quantum tomography. *Quantum Science and Technology* **2,** 025005. doi:`10.1088/2058-9565/aa6ae2` (2017).

102. Guţă, M., Kahn, J., Kueng, R. & Tropp, J. A. Fast state tomography with optimal error bounds. *Journal of Physics A: Mathematical and Theoretical* **53,** 204001. doi:`10.1088/1751-8121/ab8111` (2020).

103. Schwemmer, C., Tóth, G., Niggebaum, A., Moroder, T., Gross, D., Gühne, O. & Weinfurter, H. Experimental comparison of efficient tomography schemes for a six-qubit state. *Physical Review Letters* **113,** 040503. doi:`10.1103/PhysRevLett.113.040503` (2014).

104. Roth, I., Kueng, R., Kimmel, S., Liu, Y.-K., Gross, D., Eisert, J. & Kliesch, M. Recovering quantum gates from few average gate fidelities. *Physical Review Letters* **121,** 170502. doi:`10.1103/PhysRevLett.121.170502` (2018).

105. Brieger, R., Roth, I. & Kliesch, M. Compressive gate set tomography. *PRX Quantum* **4,** 010325. doi:`10.1103/PRXQuantum.4.010325` (2023).

106. Curtiss, L. A., Raghavachari, K., Trucks, G. W. & Pople, J. A. Gaussian-2 theory for molecular energies of first-and second-row compounds. *The Journal of Chemical Physics* **94,** 7221–7230. doi:`10.1063/1.460205` (1991).

107. Candès, E. J. & Tao, T. The power of convex relaxation: Near-optimal matrix completion. *IEEE Transactions on Information Theory* **56,** 2053–2080. doi:`10.1109/TIT.2010.2044061` (2010).

108. Purvis, G. D. & Bartlett, R. J. A full coupled-cluster singles and doubles model: The inclusion of disconnected triples. *The Journal of Chemical Physics* **76,** 1910–1918. doi:`10.1063/1.443164` (1982).

109. Møller, C. & Plesset, M. S. Note on an approximation treatment for many-electron systems. *Physical Review* **46,** 618. doi:`10.1103/PhysRev.46.618` (1934).

110. Helgaker, T., Jorgensen, P. & Olsen, J. *Molecular electronic-structure theory* (John Wiley & Sons, 2013).

111. Giesbertz, K. & van Leeuwen, R. Natural occupation numbers: When do they vanish? *The Journal of Chemical Physics* **139,** 104109. doi:`10.1063/1.4820419` (2013).

112. Keshavan, R. H. & Oh, S. A gradient descent algorithm on the grassman manifold for matrix completion. *arXiv preprint arXiv:0910.5260.* doi:`10.48550/arXiv.0910.5260` (2009).

113. Wen, Z., Yin, W. & Zhang, Y. Solving a low-rank factorization model for matrix completion by a nonlinear successive over-relaxation algorithm. *Mathematical Programming Computation* **4,** 333–361. doi:`10.1007/s12532-012-0044-1` (2012).

114. Sung, K. J., Yao, J., Harrigan, M. P., Rubin, N. C., Jiang, Z., Lin, L., Babbush, R. & McClean, J. R. Using models to improve optimizers for variational quantum algorithms. *Quantum Science and Technology* **5,** 044008. doi:`10.1088/2058-9565/abb6d9` (2020).

115. Dunning Jr, T. H. Gaussian basis sets for use in correlated molecular calculations. I. The atoms boron through neon and hydrogen. *The Journal of Chemical Physics* **90,** 1007–1023. doi:`10.1063/1.456153` (1989).

116. Woon, D. E. & Dunning Jr, T. H. Gaussian basis sets for use in correlated molecular calculations. III. The atoms aluminum through argon. *The Journal of Chemical Physics* **98,** 1358–1371. doi:`10.1063/1.464303` (1993).

117. Kendall, R. A., Dunning Jr, T. H. & Harrison, R. J. Electron affinities of the first-row atoms revisited. Systematic basis sets and wave functions. *The Journal of Chemical Physics* **96,** 6796–6806. doi:`10.1063/1.462569` (1992).

118. Becke, A. D. Density-functional exchange-energy approximation with correct asymptotic behavior. *Physical Review A* **38,** 3098. doi:`10.1103/PhysRevA.38.3098` (1988).

119. Lee, C., Yang, W. & Parr, R. G. Development of the Colle-Salvetti correlation-energy formula into a functional of the electron density. *Physical Review B* **37,** 785. doi:`10.1103/PhysRevB.37.785` (1988).

120. Becke, A. D. Density-functional thermochemistry. III. The role of exact exchange. *The Journal of Chemical Physics* **98,** 5648. doi:`10.1063/1.464913` (1993).

121. Haunschild, R. & Klopper, W. New accurate reference energies for the G2/97 test set. *The Journal of Chemical Physics* **136,** 164102. doi:`10.1063/1.4704796` (2012).

122. Haunschild, R., Janesko, B. G. & Scuseria, G. E. Local hybrids as a perturbation to global hybrid functionals. *The Journal of Chemical Physics* **131,** 154112. doi:`10.1063/1.3247288` (2009).

123. Haar, A. Der Massbegriff in der Theorie der kontinuierlichen Gruppen. *Annals of Mathematics,* 147–169. doi:`10.2307/1968346` (1933).

124. Liu, D. C. & Nocedal, J. On the limited memory BFGS method for large scale optimization. *Mathematical programming* **45,** 503–528. doi:`10.1007/BF01589116` (1989).

125. Zhu, C., Byrd, R. H., Lu, P. & Nocedal, J. Algorithm 778: L-BFGS-B: Fortran subroutines for large-scale bound-constrained optimization. *ACM Transactions on mathematical software (TOMS)* **23,** 550–560. doi:`10.1145/279232.279236` (1997).

126. Sun, Q., Berkelbach, T. C., Blunt, N. S., Booth, G. H., Guo, S., Li, Z., Liu, J., McClain, J. D., Sayfutyarova, E. R., Sharma, S., *et al.* PySCF: the Python-based simulations of chemistry framework. *Wiley Interdisciplinary Reviews: Computational Molecular Science* **8,** e1340. doi:`10.1002/wcms.1340` (2018).

127. Sun, Q., Zhang, X., Banerjee, S., Bao, P., Barbry, M., Blunt, N. S., Bogdanov, N. A., Booth, G. H., Chen, J., Cui, Z.-H., *et al.* Recent developments in the PySCF program package. *The Journal of Chemical Physics* **153,** 024109. doi:`10.1063/5.0006074` (2020).

128. McClean, J. R., Rubin, N. C., Sung, K. J., Kivlichan, I. D., Bonet-Monroig, X., Cao, Y., Dai, C., Fried, E. S., Gidney, C., Gimby, B., *et al.* OpenFermion: the electronic structure package for quantum computers. *Quantum Science and Technology* **5,** 034014. doi:`10.1088/2058-9565/ab8ebc` (2020).

129. Haah, J., Harrow, A. W., Ji, Z., Wu, X. & Yu, N. *Sample-optimal tomography of quantum states* in *Proceedings of the forty-eighth annual ACM symposium on Theory of Computing* (2016), 913–925.

130. Liu, J., Musialski, P., Wonka, P. & Ye, J. Tensor completion for estimating missing values in visual data. *IEEE Transactions on Pattern Analysis and Machine Intelligence* **35,** 208–220. doi:`10.1109/TPAMI.2012.39` (2012).

131. Coleman, A. J. & Yukalov, V. I. *Reduced density matrices: Coulson's challenge* (Springer Science & Business Media, 2000).

132. Mazziotti, D. A. Structure of fermionic density matrices: Complete N-representability conditions. *Physical Review Letters* **108,** 263002. doi:`10.1103/PhysRevLett.108.263002` (2012).